"Con fundamento en los artículos 21 y 27 de la Ley Federal del Derecho de Autor y como titular de los derechos moral y patrimonial de la obra titulada ***"Adsorption in slit-like decorated pores via Markov chain Monte Carlo simulations"***, Tesis para obtener el grado de **Maestro en Ciencias (Física)**, otorgo de manera gratuita y permanente a la Facultad de Ciencias de la Universidad Autónoma de San Luis Potosí, la autorización para que difunda la obra en cualquier medio, incluido el electrónico, y la divulgue entre sus usuarios, profesores, estudiantes o terceras personas, sin que pueda percibir por tal divulgación una contraprestación"

Fecha presentación: 19 de Junio del 2020

Fecha autorización: 12 de Junio del 2020

Nombre y Firma de AUTORES

Omar Alejandro Palacios Álvarez
Estudiante

Dr. Martín Chávez Páez
Asesor

Co-asesor (si aplica)

Universidad Autónoma de San Luis Potosí

Instituto de Física

Adsorption in Slit-Like Decorated Pores Via Markov Chain Monte Carlo Simulations in the Grand Canonical Ensemble

submitted in fulfillment as
a requirement for the degree of
Master of Science (Physics)

Author:
L. F. Omar Alejandro Palacios Álvarez

Dissertation Director:
Dr. Martín Chávez Páez

Advisory Committee
Dr. Juan Faustino Aguilera Granja
Dr. Yuri Nahmad Molinari
Dr. Enrique González Tovar

San Luis Potosí, S.L.P., June 19, 2020

Abstract

Adsorption applicability of both simple and complex porous materials is very-far reaching, extending to areas of scientific and industrial importance, with a large interest in selective components devised by lithographic pattern techniques. To this end, a set of Markov Chain Monte Carlo simulations coded in the modern Julia language provided relevant insight related to the mechanism of preferential adsorption sites with the introduction of confining molecular interfaces with imposed periodic boundary conditions and constituted of an arrangement of hexagonal close packing molecules with square-well and hard-sphere interacting molecules, emulating attractive and neutral sites.

The present dissertation branches out into four main sections, commencing with the experimental fieldwork and importance of pattern-designed porous systems and their applicability. This is followed by the implemented Monte Carlo simulation technique with the underlying mathematical foundation of effective statistic sampling by introducing Markov chain generated states; as well as the technical aspects of both statistical ensembles implemented to bulk systems.

A straightforward implementation to porous systems is provided as an introduction for the discussion of the designed decorated-systems' trends and behavior as compared to it's bulk analogue.

Finally, a narrow analysis regarding pseudo-random numbers and reduced unit systems are located in the first two appendices as a complementation of the study, followed by the pseudo-interactive codes designed for first-time Julia programmers with no previous background required.

Acknowledgments

First of all, to the thesis advisor not only for properly guiding me in this scientific path but also for sharing his considerable wisdom and experience in my multiple visits to his office.

To the advisory committee, for taking the time to read the present work and provide valuable feedback.

To my family, for the long-term support and continuous encouragement in this new experience.

To my friends, for making my stay more tolerable, albeit the unceasing problematic situations arising indoors.

Finally, thankfully acknowledge the *Consejo Nacional de Ciencia y Tecnología* for the financial support (N. CVU 886355) along the whole time of development of this project.

Contents

Chapter 1

Introduction

The field of physisorption [1] in porous materials (both solid-state and soft-matter) has received great renown with the plentiful amount of recent scientific investigation that introduces newer experimental techniques, along with theoretical approaches, leading to understanding the behavior of adsorbed polymers in different environments and surface conditions, potentially prompting the development of improved materials and novel technologies.

Physical properties of fluids dramatically change as the degree of confinement approaches molecular dimensions, with many aspects of these changes remaining poorly characterized and understood. For example, a liquid's viscosity may increase by several orders of magnitude in films with molecular or nanoscale dimensions [1], but also, its structure may become completely different than the bulk fluid, depending on how the microscopic shape and atomic arrangement of the confining walls match that of the fluid's molecules.

Although experimental techniques such as surface forces apparatus (SFA), differential scanning calorimetry (DSC), neutron diffraction and/or nuclear magnetic resonance (NMR) deliver imperative information related to the properties of fluids under molecular confinement, direct experimental investigations are remarkably complicated due to frequently poorly characterized materials. Nevertheless, molecular simulations and mathematical models provide valuable data of model systems with precise pore size and shape, nature of the surface, density, temperature and type of active sites; while minimizing the experimentation effort. To this end, molecular-based methods such as Density Functional Theory (DFT) and Grand Canonical Monte Carlo (GCMC) are now well established as powerful tools in the study of numerous adsorption problems, with refined methods based on classical approaches being simultaneously implemented [2].

[1] Process in which the electronic structure of the atom or molecule is barely perturbed upon adsorption. The energy of interaction is largely due to van der Waals forces, arising from fluctuating dipole moments between the interacting fluid and substrate.

The importance of adsorption in porous materials resides in the fact that virtually all solid and semisolid materials (with the exception of metals, some dense rocks, and plastics) are porous to varying degrees , prompting very far-reaching adsorption applicability that extend to areas of scientific and industrial importance, such as adhesives, catalysts, colloids, surface coatings, thin films, wetting phenomena, lubrication, chromatography, biomedical implant modification, fracture propagation, pressure solvation, geophysical processes, and various aspects of electrochemistry through to biochemistry, where interfaces play a crucial role like in membranes and enzyme binding [1, 3]. These disciplines deal with increasingly complex, multi-component systems that are often structured at the microscopic and nanoscopic scales, with a network of internal surfaces, interfaces, and "interphases" (thin films trapped between two surfaces) that ultimately determine the overall properties of the whole system.

A common example for multi-component systems are shale rocks, which has become an increasingly important source of natural gas since the start of the century, with many developed countries spending millions of dollars worth of research destined to the challenge of understanding the geological and geochemical nature of organic shale formations to improve their gas producibility. Much of the recent attention obtained is thanks to the lower amounts of carbon dioxide emissions subsequent to methane combustion, as compared with oil burning, making it an attractive environmental-friendlier substitutional source of energy as the global oil reserves swiftly deplete and the startling concerns over the increasing amounts of carbon dioxide in the atmosphere [4]. Shale rocks not only store large amounts of methane, but also heavier hydrocarbons in lower amounts but with higher market values than methane, given their applicability as valuable feedstock of a variety of chemical products.

These systems represent an abundant and highly efficient energy source consisting of gas accumulations characterized by widespread gas saturation, subtle trapping mechanisms, seals of variable lithography, and relatively short hydrocarbon migration distances that are mainly composed of methane with a small fraction of ethane, propane and butane with varying compositions in various shale formations with natural fractures and intergranular porosity, mainly at nanoscale, storing gas adsorbed onto kerogen and clay-particle surfaces, or as gas dissolved in kerogen and bitumen [5]. Although, these rocks are composed of both organic and inorganic matters, the first one is a key factor that controls the adsorption uptakes in shales, with kerogen being the major organic constituent in most shale formations.

Kerogen pore surface roughness may play an important role in hydrocarbon adsorption and recovery mechanism, but, its complicated structure makes it difficult to model and having to appeal instead with graphite slit pore confinements. Recently, J. Zhou *et. al.* [6] implemented instead slit-shaped kerogen $C_{242}H_{219}O_{13}N_5S_2$ subject to molecular dynamics simulations in the canonical ensemble (NVT) and isobaric-isothermal ensemble NPT with a Dreiding force field

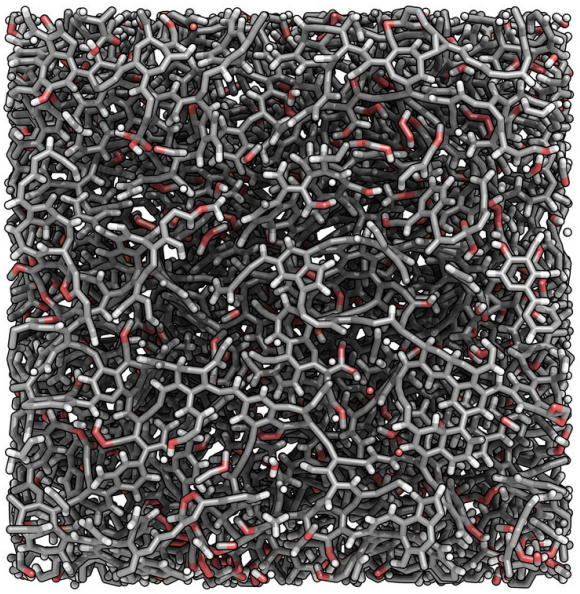

Figure 1.1: Molecular model of a sample of kerogen. Carbon, hydrogen and oxygen atoms are shown in grey, white and red respectively. Image from *Realistic molecular model of kerogen's nanostructure* by C. Bousige [7].

for molecule relaxation. The final kerogen matrixes are collected for further creation of kerogen slit pores by extending the simulation box in the Z-direction.

Despite current techniques such as pressure drawdown and horizontal drilling technology, there still remain daunting challenges for the efficient recovery of these complex hydrocarbons with only a small fraction of the total resource being found in high enough concentrations to be feasibly captured. Once fully developed, the extent of commercially viable reserves could radically alter the dynamics of supply for the world's biggest energy consumers, allowing a drastic reduction in carbon emissions as shale gas replaces coal.

Natural gas' obtention isn't the only imperative challenge, as its suitability for a particular application greatly depends on adequate ways of storing large amounts of it; this is a particular acute problem in the design of gas driven vehicles where compressed natural gas fuel tanks must be three times larger than a gasoline tank to allow a vehicle the same driving range. Because natural gas is supercritical and cannot be liquefied at ambient temperature, high-surface area adsorbents have been proposed as alternative storing methods, with the possibility of mantaining moderate physical conditions for the bulk phase [10]. M. Beckner *et. al.* [11] benchmarked adsorbed natural gas (ANG) which definitely stores more than the conventional compressed natural gas (CNG) at low pressure and can deliver more fuel, depending on the depletion pressure of the system. Not only its storage is more efficient, but ANG allows for an adequate driving range to cover the daily commute while operating at a low pressure [12].

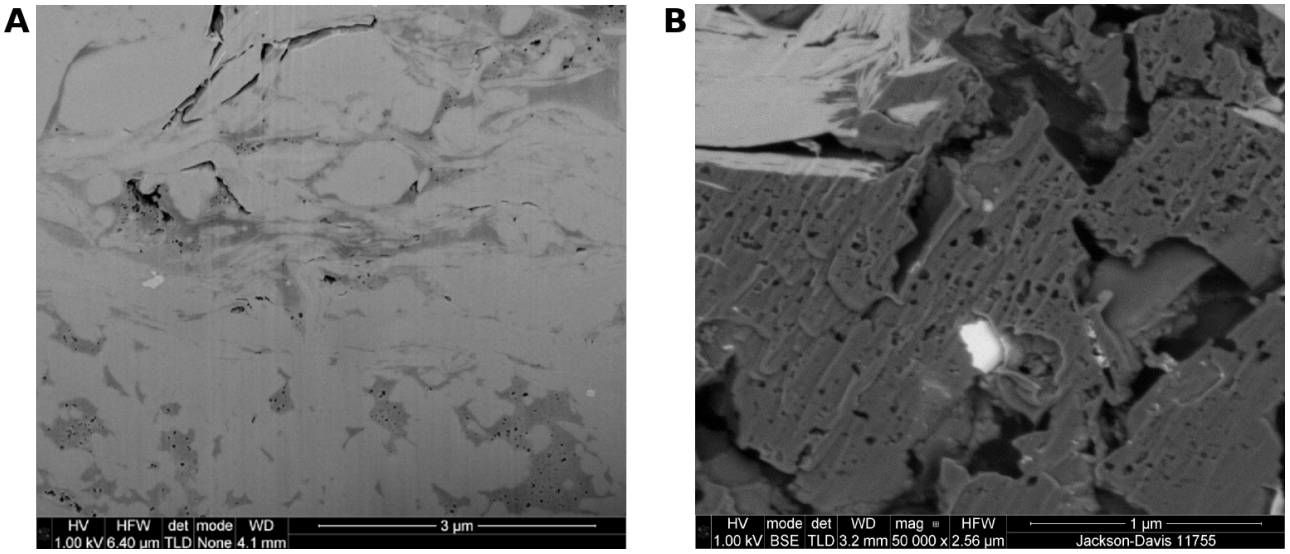

Figure 1.2: **(A)** SEM image showing porosity and kerogen within a shale. Pores are found in black, kerogen in dark gray and clay and silica in light gray. Image taken from *Shale gas-in-place calculations part I: new pore-scale considerations* by R. J. Ambrose *et. al.* [8]
(B) SEM image of a Haynesville's organic bitumen shale sample with the intrinsic structure fractured, indicating disturbance after formation and maturation. The bright object is pyrite and the light grey particles engulfed in the upper-left are clays. Image taken from *Application of FIB/SEM and Argon Ion Milling to the Study of Foliated Fine Grained Organic Rich Rocks* by C. H. Sondergeld *et. al.* [9]

Another type of interesting porous systems are zeolites, porous solids with TO_4 (T-atoms usually refer to Si, Al, or in some cases also P) basic building blocks found at the corners, forming regular pore networks. This mineral has gained a significant interest mainly due to their valuable properties such as ion-exchange capability, sided with their low cost and local availability.

They are used in many technological applications as molecular sieves, catalysts and adsorbents in the pretroleum and chemical industries, environment protection, phosphate-free washing agents and as catalysts in gasoline production. Most of these rely on the fact that the pores have dimensions comparable with the size of the molecules that can be adsorbed.

The group of R. I. Yousef [13] studied aquatic environments polluted of phenol coming from wastewaters of paint, pesticide, coal conversion, polymeric resin and petrochemical industries in the Jordanian region. In order to diminish the pollution, zeolitic tuff proved to be a low cost adsorbent for the removal of phenol from water, being this adsorbed onto zeolites spontaneously.

A similar investigation regarding acid mine drainage, the outflow of acidic water from metal or coal mines into water streams, was investigated by T. Motsi *et. al.* [14] where they showed that natural zeolites can effectively remove heavy metals from relatively dilute acid mine drainage, making it an eligible substitute for the more expensive adsorbents due to its

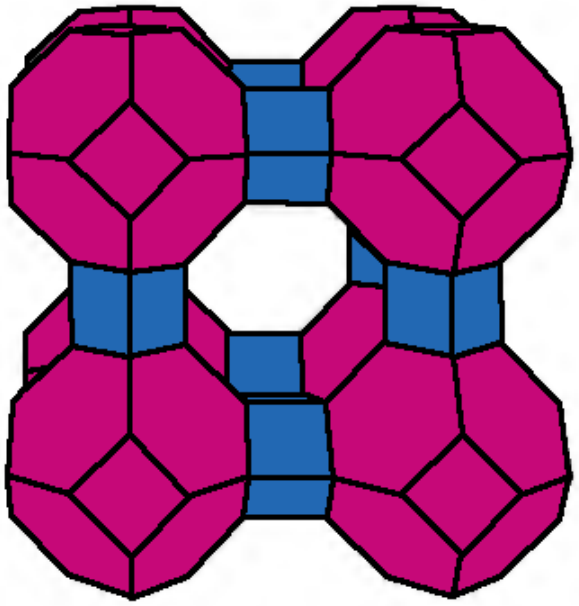

Figure 1.3: Structure scheme of zeolites, with the vertices marking the positions of the T-atoms (found in magenta) and the lines (found in blue) symbolize the oxygen bridges between them.

large availability and low cost.

In many of these applications, it is desirable to have surfaces that "recognize" and selectively adsorb specific monomeric sequences with practical implications in designing smart sensors that are capable of discriminating between different analytes or toxins, in the discovery of new drugs that bind to specific receptors, and in the development of chromatographic materials for target separation [3]. Progress in micro and nanotechnology applicability depends upon the capability to fabricate structures in a variety of materials with great accuracy, with the ability of patterning different scale structures.

To fully benefit, low-cost and high-throughput manufacture is essential, with lithographic patterning being one of the most promising development technologies in the recent years. This process consists of two steps; the first one is the imprintment, where a mold with a nanoscale design on its surface is employed to deform a thin resist film (or an active material) deposited on a substrate, followed by a pattern-transfer (an anisotropic etching process, such as reactive ion etching), used to remove the residual resist in the compressed area, transferring the thickness contrast pattern created by the imprint into the entire resist.

The resist can be either a thermal plastic, UV/thermal curable polymers or other deformable materials. For a thermal plastic resist, this is heated above its glass transition temperature during imprint, where the resist becomes viscous liquid and the mold is pressed into

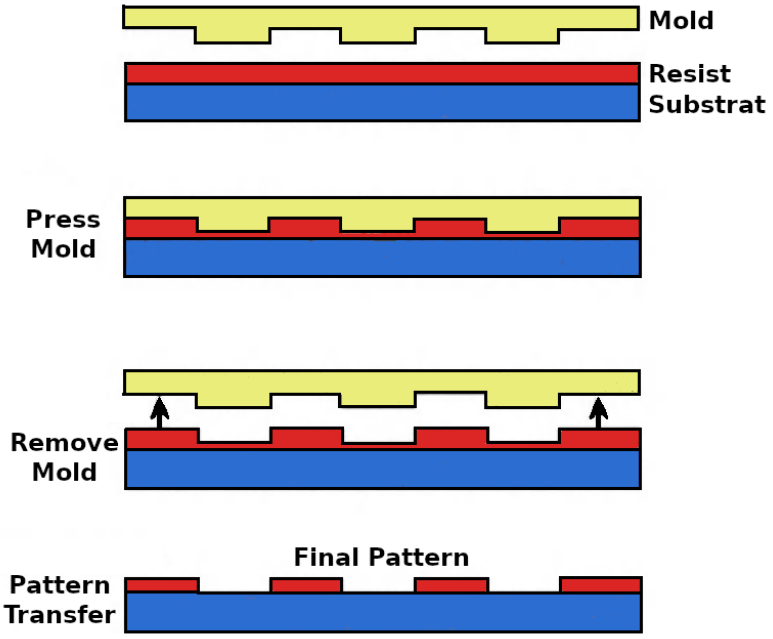

Figure 1.4: Schematic nanoimprint lithography process using a moldcreate pressed against a resist.

the resist. After that, it is cooled below its glass transition temperature before being separated from the mold.

In case it's a thermal or UV curable polymer (often in a liquid thin film form on a substrate), it's imprinted by the mold and then cured by UV light radiation or thermal heating, depending of the material [15].

Adsorption in patterned porous surfaces has multiple fields of applicability, such as magnetic structures representing an important development area of new information technology

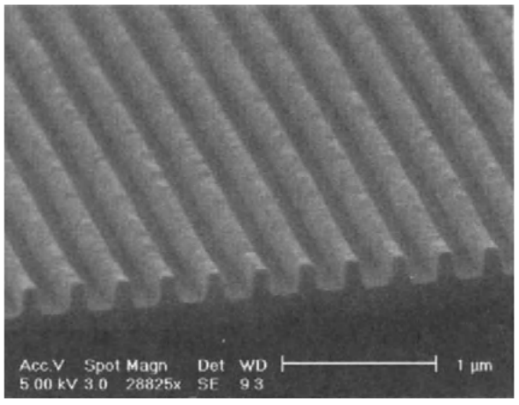

Figure 1.5: SEM micrograph of 120 nm wide structure fabricated by nanoimprint lithography. Image taken from *Alternative Lithography* by C. M. S. Torres [15]

mainly towards ultra high-density recording, magnetic randomly accessible memories, spin transistors, resonant tunnel devices and non-volatile programmable logic. In the optical industry, a great demand of patterned devices to be used in cameras, eyeglasses and optical fibre, but also in modern measurement and control systems is greatly under demand. Moreover, photolithography is the standard method of printed circuit boards and microprocessor fabrication.

In the field of biotechnology, organic molecules are particularly appealing building blocks for lithographic processes due to the inherent precision in their size, shape, chemical functionality and relatively low production costs, with these properties being translated directly to biomedical applications for the use of selective patterning of proteins, synthetic biomaterials, and cell-seeded biomaterials.

The chemical functionality of an organic molecule can be used to couple patterned organic molecular assemblies with inorganic thin-film growth methods such as physical vapor deposition (PVD), chemical vapor deposition (CVD) or atomic layer deposition (ALD) to direct spatially constrained metal or semiconductor thin films, granting the ability to design devices through self-assembly techniques with great molecular precision, being one of the benchmarks of lithographic patterning. Organic molecular assembly includes methods of patterning self-assembled organic monolayer films through soft-lithographic methods such as microcontact printing (μCP) and nanoimprint lithography (NIL), through direct processes with a nanometer-sized tip and through exposure to electron or photon beams.

Chapter 2

Monte Carlo

Computational simulation methods spawn data allowing a correlation to approximate theoretical solutions, where no perfect physical realization of a system may be obtained. This allows an, as complete as possible, understanding of the physical properties of elected systems while making use of the entire control of "experimental" variables in a computer analysis, reviewing every aspect of the system's configuration in detail.

An essential simulation scheme is the Monte Carlo method, which dates back to 1945 with the building of the first electronic computers. This technique revolves around the idea that a determinate mathematical problem may be taken over by a probabilistic analog, which is then solved by stochastic sampling experiments that employ a source of uniformly distributed pseudo-random numbers during the process to make decisions [16]. Although employing two different sequences of pseudo-random numbers won't arise identical results, an agreement within some statistical error must be met.

Equilibrium statistical mechanics takes interest in thermal averages of interacting many-particle systems, an achievable task for the Monte Carlo method by taking proper account of statistical fluctuations of the system from state to state throughout the simulation and their effects in such configurations. The transition from one state to another simulates the dynamics of the system, resulting in each state appearing with the probability appropriate to the state itself.

In the context of a liquid, determining the configuration energy by solving the coupled equations of motion of the atoms and averaging over time might sound like the way to go, but, setting up an ensemble of states of the liquid by choosing individual states with the appropriate probability and calculating the configuration energy by averaging uniformly over the ensembles,

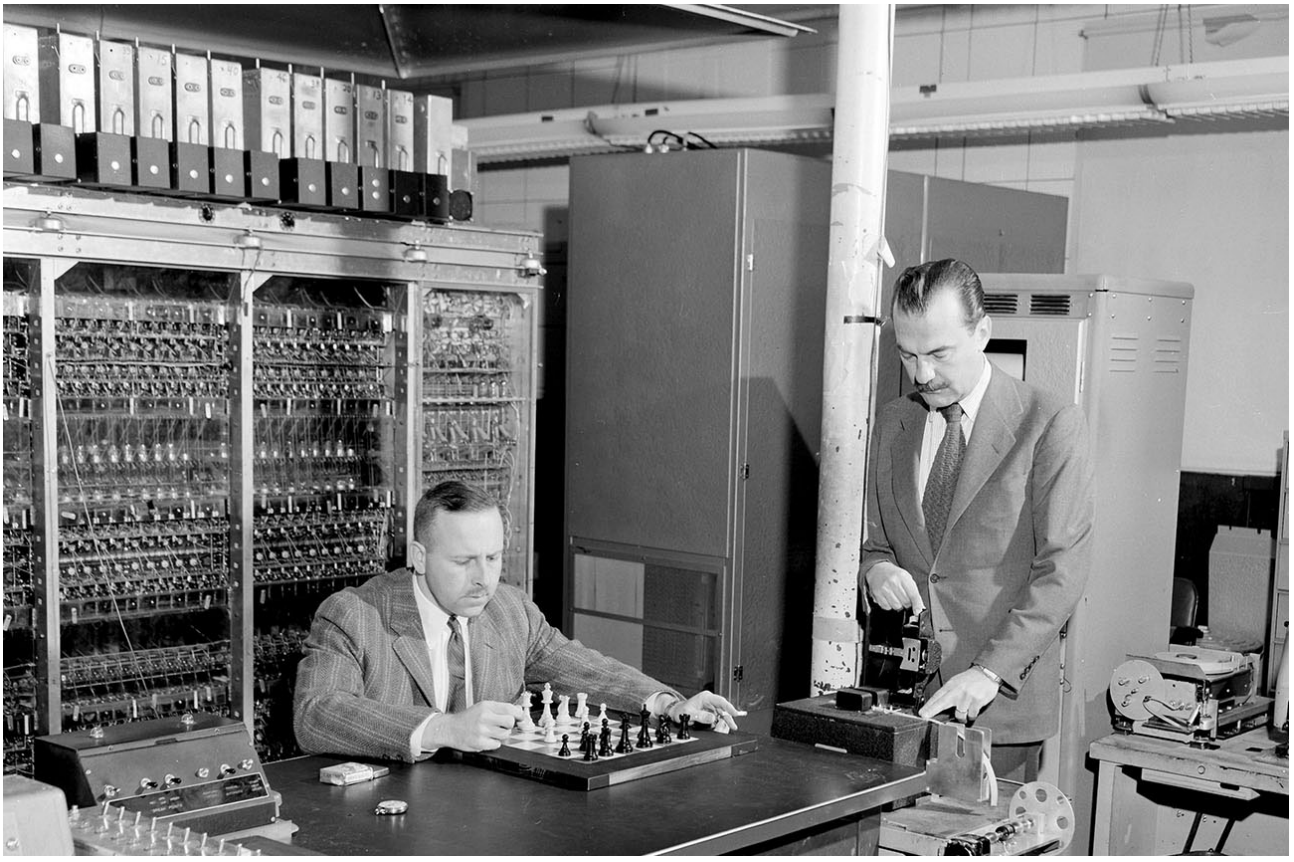

Figure 2.1: P. Stein (left) and N. Metropolis (right) playing modified chess with the MANIAC I. Image courtesy of *Herbert L. Anderson* in the article *Metropolis, Motne Carlo, and the MANIAC* [19].

tends to be a more profitable task due to the technique relying on only requiring a small fraction of states of the system to be sampled to get accurate estimates of physical quantities and the randomness of the method boosting the probing of phase space. An increment in the number of samples improves the estimations while remaining an inherent arise of statistical error due to finite statistical sampling.

This methodology implemented in the supercomputer MANIAC represented a milestone as being the first study characterizing the equations of state for the two-dimensional motion of hard spheres, where the strategy implemented led to an improvement in computer efficiency for equilibrium systems ruled by a Boltzmann distribution function [17]. If a statistical "displacement" of a particle in the system decreased the total energy, the new configuration was accepted. Otherwise, if the same "displacement" increased the total energy with the new configuration, it was accepted only if it survived a game of chance biased by a Boltzmann factor.

For the complete anecdote and context around the Monte Carlo method, N. Metropolis wrote a short article telling the detailed story of the algorithm, which includes the reason behind the coinage of this famous method's name. [18]

2.1 Estimator and General Principle

The usual goal in a Monte Carlo simulation of a thermal system is the calculation of an expectation value $\langle \xi \rangle$ of a certain physical observable quantity ξ. Ideally speaking, such calculation derives from averaging the quantity of interest over all existing states μ of the system, weighting each with its Boltzmann probability:

$$\langle \xi \rangle = \frac{\sum_\mu \xi_\mu e^{-\beta E_\mu}}{\sum_\mu e^{-\beta E_\mu}}. \tag{2.1}$$

This is only feasible in a minuscule amount of small-scale systems; in practice, this rarely happens. Given the time constraint for the computational calculation, one must limit to average over some subset of states at random from a probability distribution p_μ. By picking M states $\{\mu_1, \mu_2, ..., \mu_M\}$, ξ may be estimated as:

$$\xi_M = \frac{\sum_{i=1}^{M} \xi_{\mu_i} p_{\mu_i}^{-1} e^{-\beta E_{\mu_i}}}{\sum_{i=1}^{M} p_{\mu_i}^{-1} e^{-\beta E_{\mu_i}}}, \tag{2.2}$$

where ξ_M is called the *estimator* of ξ; in the limit $M \to \infty$, then $\xi_M = \langle \xi \rangle$. The trivial decision is to pick all states with an equal probability, reducing equation (2.2) into:

$$\xi_M = \frac{\sum_{i=1}^{M} \xi_{\mu_i} e^{-\beta E_{\mu_i}}}{\sum_{i=1}^{M} e^{-\beta E_{\mu_i}}}. \tag{2.3}$$

The estimator above tends to be a poor guide to the value of $\langle \xi \rangle$, given that one or both of the sums may be dominated by a small number of states. This effect is commonly witnessed at low temperatures, where the thermal energy is not enough to lift the system into the higher excited states, spending most of the time in the low-energy states.

2.2 Importance Sampling

Instead of randomly selecting from a total of μ available states, picking the M samples from states that make an important contribution to the sum in equation (2.1) would increase the estimation of $\langle \xi \rangle$ with the same sample size. In other words, rather than having all the states popping up with equal probability p_μ, let them be proportional to their Boltzmann weight to narrow the ranges of energy popping up in the simulation. This is the most common form of *importance sampling*.

For a particular state μ, its probability of being chosen is $p_\mu = Z^{-1}e^{-\beta E_\mu}$ which reduces the estimator from equation (2.2) into:

$$\xi_M = \frac{\sum_{i=1}^{M} \xi_{\mu_i}}{\sum_{i=1}^{M} 1} = \frac{1}{M}\sum_{i=1}^{M} \xi_{\mu_i}. \tag{2.4}$$

This new estimation is the arithmetic mean of the samplings, which gets closer to the expected value of ξ for M large enough. This is visualized by assuming that the sampled values of ξ_μ are such that the event x_1 occurs κ_1 times, event x_2 occurs κ_2 times, ..., and x_M occurs κ_M times. Then,

$$\sum_{i=1}^{M} \xi_{\mu_i} = x_1\kappa_1 + x_2\kappa_2 + ... + x_M\kappa_M \tag{2.5}$$

Hence,

$$\frac{1}{M}\sum_{i=1}^{M} \xi_{\mu_i} = x_1\frac{\kappa_1}{M} + x_2\frac{\kappa_2}{M} + ... + x_M\frac{\kappa_M}{M} \tag{2.6}$$

For a large amount of samplings, the frequencies κ_i/M for each x_i tend to their probabilities p_i, therefore, $\kappa_i/M \approx p_i$. In consequence,

$$\frac{1}{M}\sum_{i=1}^{M} \xi_{\mu_i} = \sum_{i=1}^{M} x_i\frac{\kappa_i}{M} \approx \sum_{i=1}^{M} x_i p_i = \langle\xi\rangle \tag{2.7}$$

Equation (2.7) establishes the *Weak Law of Large Numbers* (also known as Bernouilli's theorem) stating that as the sample of independent and identically distributed random variables grows larger, the sample mean will tend towards the population mean.

Theorem 2.2.1 Law Of Large Numbers

$$\lim_{n\to\infty} P(|\langle x\rangle - \mu| \geq \epsilon) = 0 \tag{2.8}$$

As the sample size N grows to infinity, the probability that the sample mean $\langle x\rangle$ differs from the population mean μ by some small amount ϵ is equal to 0.

Calculation of the second moment of a probability distribution is of great quintessence. It's better known as the *variance*, which characterizes the spread of values around the mean,

and is determined as the average squared distance from the mean value:

$$Var(\xi) = \sigma_\xi^2 = \langle(\xi - \langle\xi\rangle)^2\rangle = \langle\xi^2\rangle - \langle\xi\rangle^2. \tag{2.9}$$

As the arithmetic mean converges in probability to $\langle\xi\rangle$, the size and distributional form of the stochastic fluctuations during its convergence are ruled by the central limit theorem. For a large enough amount of samples M, the distribution of ξ_M is close to the normal distribution with mean $\langle\xi\rangle$ and variance σ^2/M. The usefulness of the theorem is that taking the mean value of variables ξ_μ with *any* well-behaved probability distribution function, the sampling distribution of the mean value approaches a normal distribution. A consistent and clear proof is presented by V. Apaja, where an example using a Cauchy distribution shows that the central limit theorem is not valid for all distribution functions [20].

Theorem 2.2.2 Central Limit

Given a distribution with mean μ and variance σ^2, the sampling distribution of the mean approaches a normal distribution with a mean μ and a variance σ^2/N as the sample size N increases.

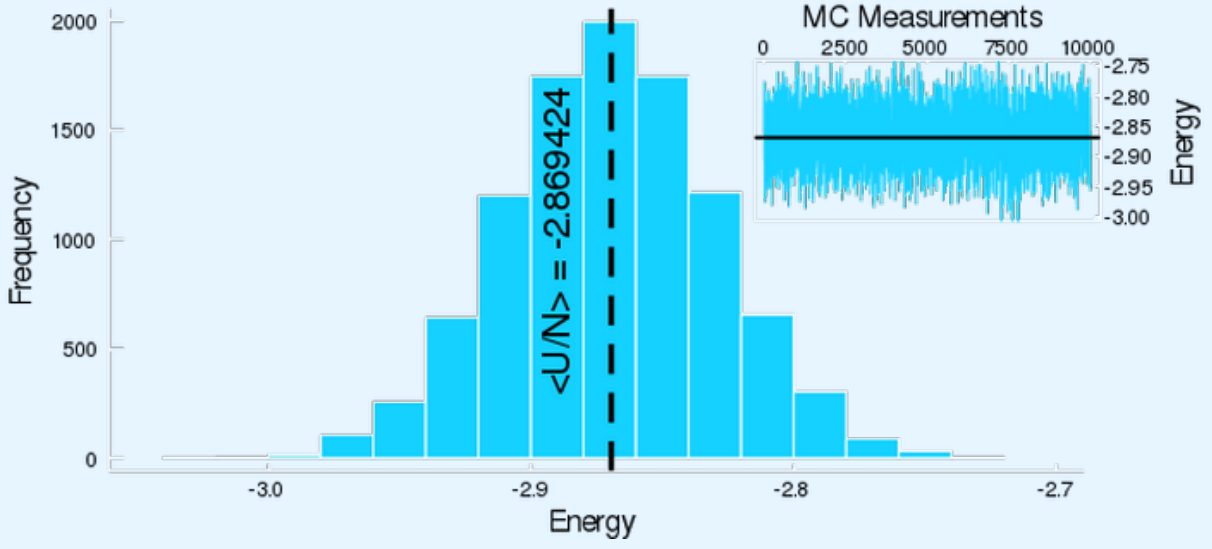

Figure 2.2: Energies histogram displaying a normal behavior for an arbitrary Monte Carlo simulation.

2.3 Metropolis Method

Statistical mechanics analytically deals with very dilute fluids (ideal gases) and crystalline solids, but the treatment of strongly correlated dense fluids (and their solid counterparts, amorphous glasses) represents a much more difficult task. Even the description of short-range order in fluids in a thermodynamic state far away from any phase transition is a non-trivial matter. This complication regards fluid dynamics as a *stochastic process*, defined as the mathematical abstraction, model or representation of its empirical analog whose development is governed by probabilistic laws; making it an ideal and very active area for Monte Carlo techniques in fluid analysis.

The generation of a random set of states according to a Boltzmann distribution with statistical weight proportional to $e^{-\beta E}$ would be no better than sampling states at random, since the probabilities for their acceptance would be exponentially small, virtually rejecting most of the states. This is where markovian processes shine as the most optimal engine for state generation.

2.3.1 Markov Process

In classical probability theory, a sequence of independent random variables $X_1, X_2, ..., X_N$ representing the outcome for N independent trials, with $S_1, S_2, ..., S_N$ being the states of the system at each trial. Since the trials are independent, the probability of observing the sequence of outcomes $S_{j,1}, S_{j,2}, ..., S_{j,N}$ simplifies to the product of the probabilities associated with the outcomes

$$P\{S_{j,1}, S_{j,2}, ..., S_{j,N}\} = P\{X_1 = S_{j,1}\}P\{X_2 = S_{j,2}\}...P\{X_N = S_{j,N}\} = p_{j,1}p_{j,2}...p_{j,N}. \quad (2.10)$$

Assuming that the outcome of any trial depends only on the directly precedent event, a conditional probability $p_{j,i}$ must be associated with every pair of states:

$$p_{j,i} = P\{S_j \to S_i\} = P\{X_N = S_j | X_{N-1} = S_i\}. \quad (2.11)$$

This kind of process are named Markovian and the sequence of states $\{X_t\}$ for a discrete set of times $t_1, t_2, ..., t_N$ is called a *Markov chain*, where the conditional probability from equation (2.11) is interpreted as the transition probability to move from state j to state i.

Theorem 2.3.1 Markov Chain

Abstraction from an empirical process associated with systems whose state change with time (according to some probability law) in such a manner that the probability of the system going from a given state S_i at a time t_λ to a state S_j at a time $t_{\lambda+1}$ depends only on the state S_i at time t_λ and is independent of the states of the system at times before t_λ. [21]

The set of all conditional probabilities $p_{j,i}$ forms the transition matrix $P = \{p_{j,i}\}$ which completely determines the properties of the (irreducible) Markov chain.

$$P = \begin{bmatrix} p_{1,1} & p_{1,2} & p_{1,3} & \cdots \\ p_{2,1} & p_{2,2} & p_{2,3} & \cdots \\ p_{3,1} & p_{3,2} & p_{3,3} & \cdots \\ \vdots & \vdots & \vdots & \ddots \end{bmatrix} \tag{2.12}$$

Clearly, P must be a square matrix with non-negative elements ($p_{j,i} \geq 0$) and unit row sums ($\sum_j p_{j,i} = 1$). If the transition probabilities are independent of time, establishing its initial condition at $t = 0$ uniquely defines the Markov process [22]. Consequently, knowledge of the state at time t entirely determines the future time evolution, making the random variables in the Markov chain not independent, but dependent over the extension of one unit time; therefore, its sequence of samples are now correlated.

Hastings in 1970 generalized the algorithm to account for nonsymmetric transfer matrices, showing that the asymmetry is compensated in the acceptance probabilities [23].

2.3.2 Ergodicity

The main limitation of the Monte Carlo method is the slow convergence of Markov chains. Regularly, chain's links correspond to only a handful of independent configurations, thus, decorrelation becomes troublesome to the point that independent samples may not be created in a finite computational time.

Ideally speaking, one expects the chain to be able to attain any state of the system from any other previous state. Although some transition probabilities of the process are zero, there must be at least one path of non zero transition probabilities; but this doesn't always happen

and the chain might be stuck in an *absorbing* state, denying the transition to any other state. If each of its states is linked with some absorbing state, the chain becomes an *absorbing Markov chain*.

Theorem 2.3.2 Absorbing Markov Chain

A *Markov chain* is an *absorbing* chain if:

- There is at least one reachable absorbing state that, once entered, cannot be left.
- It is possible to go from any state to at least one absorbing state in a finite number of states.

States of the chain that aren't absorbing are called *transient*.

If the *Markov chain* is constituted by only *transient* states, then all possible configuration states of the system must be attainable in a finite number of steps, since the transition probabilities for any pair of states S_i and S_j is non zero. This is known as the *ergodicity principle*.

Theorem 2.3.3 Ergodic Markov Chain

An irreducible Markov chain has a stationary distribution if and only if the Markov chain is ergodic. If the Markov chain is ergodic, the stationary distribution is unique.

Proving that the method of choosing new configurations is ergodic may represent a problematic task since states can get trapped in subsets of the configuration space in a periodic loop. A *quasi-ergodic* definition is coined for instances where high energy barriers may be found between subspaces, so, theoretically speaking, all states are reachable but highly improbable in a finite simulation.

Below a phase transition, multiple different ordered states may appear, well separated in phase space. If the phase transition from the disordered phase to the ordered phase is associated with ergodicity breaking, therefore the system stays in one separate region in phase space [24].

2.3.3 Detailed Balance

As equilibrium is achieved, the Markov chain expects upcoming states S_j to pop up with non-zero probability $\pi(S_j) > 0$, where π is the probability distribution function to be associated with the chain. The crucial defining condition for equilibrium is that the rate of change of the probability of being in a given state is equal to the probability of transitioning into that state at the given time minus the probability of transitioning out of that state. This is mathematically expressed as

$$\frac{dP\{S_j(t)\}}{dt} = \sum_j P\{S_i \to S_j\}\pi(S_i) - \sum_j P\{S_j \to S_i\}\pi(S_j) \tag{2.13}$$

and is the so-called master equation, which states how the probability of a state varies as a function of the simulation time and expresses the fact that the total probability is conserved at all times ($\sum_j P\{S_j(t)\} = 1$). For stationary transition probabilities, the left-hand of equation (2.13) vanishes into

$$\sum_j P\{S_i \to S_j\}\pi(S_i) = \sum_j P\{S_j \to S_i\}\pi(S_j). \tag{2.14}$$

Previous equality states that the rate at which the system makes transitions into and out of any state must be equal. This is known as the weaker *balance condition*, but it might not always guarantee that the actual states will have anything like the desired probability distribution since it might get stuck to a set of a few different values, called a limit cycle [25]. This problem can be evaded by applying a more meticulous condition to the transition probabilities, where

$$\pi(S_j)P\{S_j \to S_i\} = \pi(S_i)P\{S_i \to S_j\}, \quad \forall\, i, j \in S. \tag{2.15}$$

This is the *detailed balance* condition, also acknowledged as microscopic reversibility, and guarantees that any set of transition probabilities fulfilling this condition also satisfy the weaker *balance condition*. It also states that on average, the system should go from S_i to S_j just as often as it goes from S_j to S_i. In a limit cycle, the probability of occupation of some or all of the states changes in a cyclic fashion, for instance, there must be more transitions into certain states than out of them, on average. The condition of detailed balance forbids dynamics of this kind and hence forbids limit cycles.

Theorem 2.3.4 Reversible Markov Chain

A stationary Markov chain is reversible if, and only if, there exists a collection of non-negative numbers $\pi(S_j), j \in S$, summing to unity which solves the detailed balance equations:

The detailed balance condition is sufficient, but not necessary. It has been proved via the Perron-Frobenius theorem that the substantially weaker balance condition is necessary and sufficient requirement for the eigenvector of the irreducible stochastic matrix to be the limiting distribution of the chain, bringing more flexibility in developing Monte Carlo methods.[26]

Equation (2.13) and the unitary row summation from the transition matrix can be used to prove that:

$$\sum_j P\{S_j \to S_i\}\pi(S_j) = \pi(S_i)\sum_j P\{S_i \to S_j\} = \pi(S_i). \tag{2.16}$$

For any set of transition probabilities satisfying this equation, the asymptotical probability distribution $\pi(S_i)$ will be an equilibrium of the dynamics of the Markov process.

Computers modeling real physical systems tend to obey the detailed balance condition, given the reasoning of time-reversal symmetry. When shifting the flow of time, the dynamics around a limit cycle are also reversed, becoming clear that the motion of the system in equilibrium is not the same forward as it is backward. Such a violation of time-reversal symmetry is forbidden for most systems and, although detailed balance shouldn't be imposed in a simulation, it's helpful to more accurately mimic the dynamics of the real system.

In essence, the probability distribution of states generated by a Markov process tend to any distribution π_i (a contraction of $\pi(S_i)$) given a set of transition probabilities satisfying the detailed balance condition (2.15). By selecting the equilibrium distribution to be the Boltzmann distribution, the detailed balance equation specifies the transition probabilities as

$$\frac{P(S_j \to S_i)}{P(S_i \to S_j)} = \frac{\pi_i}{\pi_j} = e^{-\beta(E_i - E_j)}. \tag{2.17}$$

As long as the transition probabilities satisfy the normalization constraint, the ergodicity principle, and the detailed balance condition, then the equilibrium distribution of states in the Markov chain process will converge to the Boltzmann distribution [16, 27]. Having the

freedom of making the transition probabilities take any arbitrary set of values, allows any state generation algorithm to be valid by introducing the new concept of *acceptance probability* and a transition probability decomposition as follows:

$$P(S_j \to S_i) = g(S_j \to S_i)A(S_j \to S_i), \tag{2.18}$$

where $g(S_j \to S_i)$ is the *selection probability* (probability of proposing a state S_i given S_j) and $A(S_j \to S_i)$ the *acceptance ratio* (probability to accept the transition); the last one being able to take any value between zero and one, with the lower bound making the system never leave state S_j.

Redefinition of the transition probabilities along with the detailed balance condition fixes the ratio (2.17) into

$$\frac{P(S_j \to S_i)}{P(S_i \to S_j)} = \frac{g(S_j \to S_i)A(S_j \to S_i)}{g(S_i \to S_j)A(S_i \to S_j)}, \tag{2.19}$$

where the ratio $A(S_j \to S_i)/A(S_i \to S_j)$ is able to take any value between zero and infinity, meaning both $g(S_j \to S_i)$ and $g(S_i \to S_j)$ are now unrestricted.

The selection probabilities $g(S_j \to S_i)$ are chosen so that the condition of ergodicity (every state is accessible from every other state in a finite number of steps) is fulfilled. However, the energies of systems in thermal equilibrium stay within a very narrow range of values, with the energy fluctuations being small compared to the energy of the entire system. In other words, the real system spends most of its time in a subset of states with a narrow range of energies and rarely makes transitions that change the energy of the system dramatically. Therefore, it's not desired to spend much time considering transitions to states whose energy is very different from the energy of the present state. The simplest way of achieving this is to consider only those states which differ from the present one by the displacement of a single molecule, thus having N non-zero selection probabilities $g(S_j \to S_i)$, for simplicity each one taking the value:

$$g(S_j \to S_i) = g(S_i \to S_j) = \frac{1}{N}. \tag{2.20}$$

Combining (2.19) with (2.17), takes the form:

$$\frac{P(S_j \to S_i)}{P(S_i \to S_j)} = \frac{g(S_j \to S_i)A(S_j \to S_i)}{g(S_i \to S_j)A(S_i \to S_j)} = \frac{A(S_j \to S_i)}{A(S_i \to S_j)} = e^{-\beta(E(S_i)-E(S_j))}. \tag{2.21}$$

To maximize the acceptance ratios from the previous constraint, it's optimal to provide the larger of the two ratios the probability of one and then adjust the other to satisfy the constraint. For example, suppose two states S_i and S_j with $E_i < E_j$ (a contraction of $E(S_i)$ and $E(S_j)$). Then the larger of the two acceptance ratios is $A(S_j \to S_i)$, which is set equal to one. In order to satisfy equation (2.21), $A(S_i \to S_j)$ must then take the value $e^{-\beta(E_j - E_i)}$. Thus, the optimal algorithm is reduced to:

$$A(S_j \to S_i) = \begin{cases} e^{-\beta(E_i - E_j)} & \text{if } E_i - E_j > 0 \\ 1 & \text{otherwise} \end{cases} = min\{1, e^{-\beta(E_i - E_j)}\} \tag{2.22}$$

In other words, if the new state has energy lower or equal than the present one, the transition to that state should always be accepted. On the other hand, if it has higher energy it might be accepted with a probability as given above. The procedure just described constitutes the *Metropolis Algorithm*, pioneered by Metropolis and co-workers in their paper on hard-sphere gases [17].

Rehashing, a Monte Carlo algorithm that generates random new states S_i given old ones S_j, with some set of probabilities $g(S_j \to S_i)$ that may be accepted or rejected according to an acceptance probability $A(S_j \to S_i)$ that satisfies equation (2.18) will meet all the requirements for the transition probabilities, therefore, producing a string of states which, when equilibrium is reached, will each appear with their correct Boltzmann probability. It's important to keep in mind that if the acceptance probabilities for the moves are small, then the algorithm will spend most of the time staying in the same state it is in, instead of nimbly sampling a wide selection of different states. An ideal algorithm selects new states with exactly the correct transition probabilities all the time, and the acceptance probability is always one [25].

2.4 Canonical Ensemble

For a system of N molecules confined in a box of volume V in thermal equilibrium at a given temperature T, a Markov chain with constant transition probabilities is established to model the NVT ensemble. Each state of the chain represents a point in the 3N-dimensional phase space spanned by all $\vec{r}_i$ coordinates. Due to computational arguments, phase space must be subdivided into a sufficiently large number of cells; this simplification enables the theory of discrete chains. An adequately fine subdivision, revolved around the number of binary bits used to represent the position coordinates of the molecules, could approach the results for a continuum set of states [27]. Implementation of the algorithm assumes that an atomic or

molecular model in a suitable starting configuration specifies all intermolecular interactions to generate the trial moves.

Translational motion is normally carried out in cartesian coordinates with a limit set to the maximum change in each of the x-, y- and z-directions often represented by a vector of *maximum step-length* $\vec{\delta}$ which, for anisotropic systems, may be advantageous to take different values $\delta_x, \delta_y, \delta_z$ for each direction. In the present work, the arbitrary initial values were defined as proportional to the length of the simulation box as $\delta_i = L_i/8$ in each coordinate.

For a very small maximum step-length, most displacements are accepted due to smaller changes to the potential energy between states. Otherwise, for large enough values, the gap of energy between the new and old state becomes too large, culminating in the presumable rejection of the trial move. A self-adapting $\vec{\delta}$ is employed to adjust that approximately half the trial moves are accepted; this is done by implementing a simple *if* conditional that updates the value after a predefined interval of steps:

```
if Accepted_Moves / Total_Moves > 0.55
  δ_i = 1.05 * δ_i
else if Accepted_Moves / Total_Moves > 0.45
  δ_i = 0.95 * δ_i
end if

if δ_i > L / 4
  δ_i = L / 4
else if δ_i < 0.05
  δ_i = 0.05
end if
```

Code 2.1: Conditional to update maximum step-length along the simulation.

This maximum step-length is constrained to the domain $\delta_i \in [0.05, L_i/4]$ to prevent unmanageable scaling of the displacements.

Selection of a random particle i with a random displacement from old configuration μ to the new one ν is given by:

$$\begin{aligned} x_i^\nu &= x_i^\mu + \delta_x(\eta_x - \tfrac{1}{2}) \\ y_i^\nu &= y_i^\mu + \delta_y(\eta_y - \tfrac{1}{2}) \\ z_i^\nu &= z_i^\mu + \delta_z(\eta_z - \tfrac{1}{2}) \end{aligned} \tag{2.23}$$

where η_x, η_y, η_z are random numbers uniformly distributed between 0 and 1.

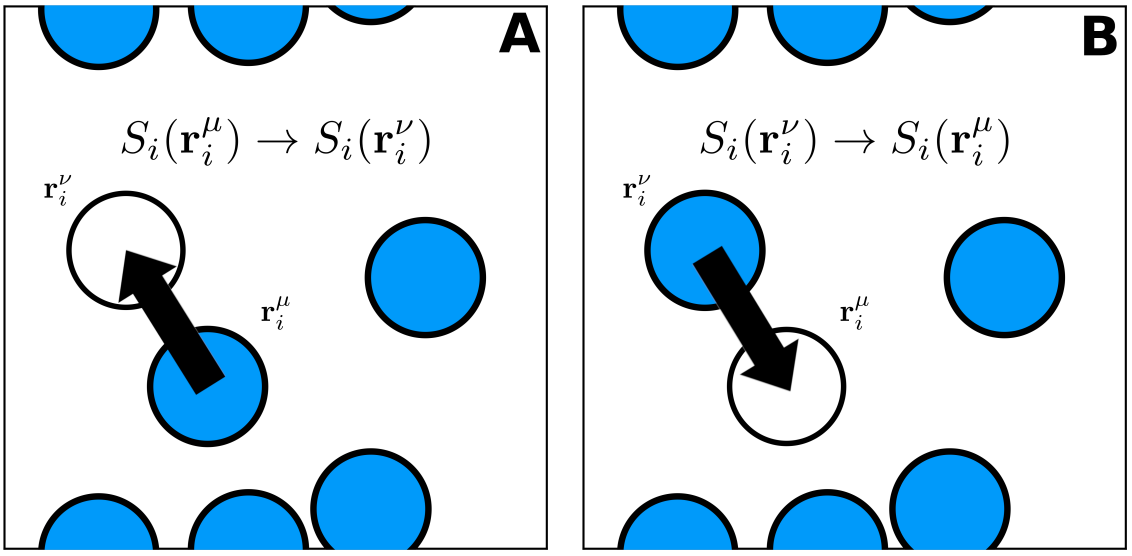

Figure 2.3: **(A)** State ν is generated from state μ by displacing a molecule i from $\vec{r}_i^{\,\mu}$ to $\vec{r}_i^{\,\nu}$. **(B)** The reverse move. To ensure microscopic reversibility, the probabilities of attempting the forward and reverse moves should be equal.

The resulting change in energy of the system ΔU caused by the move may have two outcomes according to the optimal acceptance criteria (2.22):

- $\Delta U \leq 0$: The move brings the system to a state of lower energy, therefore, the movement to its new position must always be allowed.
- $\Delta U > 0$: The move brings the system to a state of higher energy, which is allowed with probability $e^{-\beta \Delta U}$. This means comparing such probability with a random uniform number $\eta \in [0, 1]$. If $\eta < e^{-\beta \Delta U}$ the move is accepted; else, it's rejected.

therefore, the criteria is divided into three different categories: Always accepted, accepted and rejected.

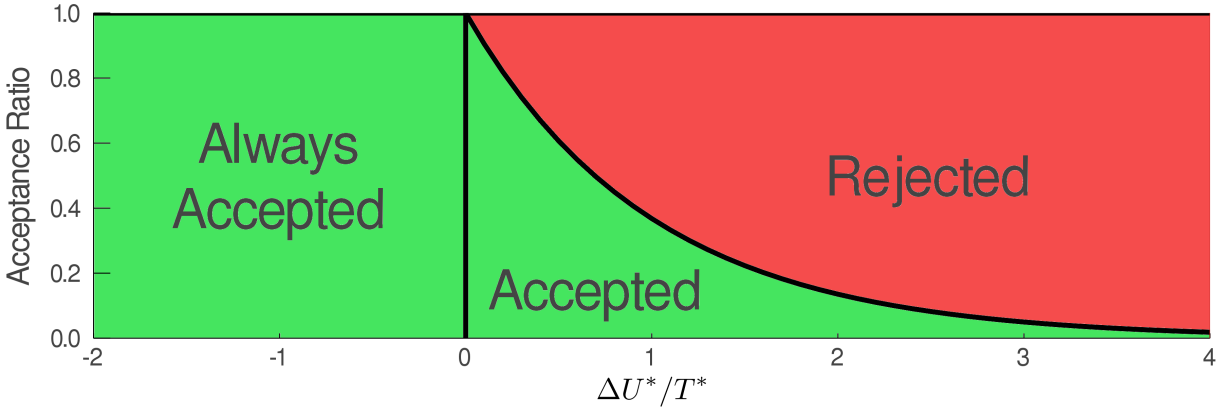

Figure 2.4: Acceptance/Rejection diagram for the NVT Monte Carlo simulation.

The implementation of the algorithm can be summarized by the following steps:

Algorithm 1 *NVT* Metropolis Monte Carlo

1. Generation of an initial state. Molecules should be distributed in non-overlapping configurations to avoid discontinuities in the potential energy.
2. Random selection of molecule i with a given displacement $\vec{r}_i^{New} = \vec{r}_i^{Old} + \vec{\delta}_i(\vec{\eta} - \frac{1}{2})$.
3. Calculate energy change $\Delta U = U(\vec{r}_N^{New}) - U(\vec{r}_N^{Old})$.
   - If $\Delta U < 0$, the move is accepted.
   - If $\Delta U > 0$, a random number η is chosen such that $0 \leq \eta \leq 1$.

     If $\eta \leq e^{-\Delta U/k_B T}$ accept the move; else, reject it.
4. Sample thermal and/or structural properties of interest.
5. Repeat from step **2.** until acceptable convergence criteria has been achieved.

Quantities such as the average potential energy $\langle U \rangle$, or structural information like the radial pair distribution function g(r) are straightforward to calculate by sampling. However, the pressure is required to obtain the equation of state, which is not directly calculated by sampling as it would be for other properties. The classical virial expansion from statistical mechanics appropriately expresses the pressure of a many-particle system in equilibrium with the expansion

$$P = \rho k_B T - \frac{1}{3V} \langle \sum_{i<j} \vec{r_{ij}} \cdot \vec{\nabla} U(\vec{r_{ij}}) \rangle, \tag{2.24}$$

which is valid for continuous, pair-wise potential interactions.

2.4.1 Periodic Boundary Conditions

Simulations of atomic or molecular systems aim to provide information about the properties of a macroscopic sample. Yet, most modern computers probe structural and thermodynamical properties of a system ranging from a few hundred to thousand molecules, where clearly, this number is still far from the thermodynamic limit.

To simulate bulk phases it's essential to choose boundary conditions that mimic the presence of an infinite bulk surrounding the N-particle model system, accomplished by treating the

volume V containing the N molecules as the primitive cell of an infinite periodic lattice of identical cells (see Figure 2.5). This device overcomes the problem of having molecules bordering the edge of the simulation box. Additionally, molecules in the main simulation cell are allowed to interact only with those residing within a distance of $L/2$ in every direction, both *real* (those found in the main simulation box) or *image* (those found in the copies of the simulation box) molecules. This approach is termed *minimum image convention* and applies to systems with short-range particle-particle interactions.

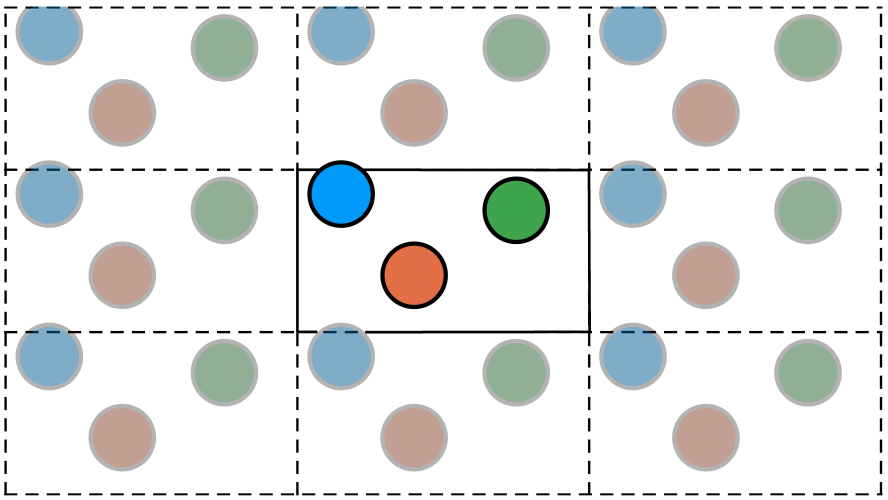

Figure 2.5: Schematic representation of periodic boundary conditions, with the cell in the center being the main simulation box. Molecules inside this box are called *real* while the blurry ones found in the rest of the cells are called *images*.

Although implementing periodic boundary conditions introduces a spurious periodicity, it usually does not represent a serious problem, especially for short-ranged interaction potentials. To reduce any potential issue, each particle in the simulation box can only interact with one of the infinite number of images of any other particle, that image being the one closest to the original particle. Furthermore, it vastly reduces the computational time needed to evaluate the energy of each configuration. An alternative method is to only take into account interactions between molecules inside a cut-off sphere around each molecule of radius r_c. This cut-off radius is often chosen to be much less than $L_i/2$ to prevent interactions with more than one image.

In practice, implementation of periodic boundary conditions is exceedingly simple and a function as follows is enough to mimic the periodicity effect:

```
1  function PeriodicBoundaryConditions!(x, L)
2    return x - L * round(x / L)
3  end
```

Code 2.2: Periodic boundary condition function for an orthorhombic system. The *round()* function rounds the quotient to the nearest integer.

2.4.2 Chemical Potential

The chemical potential is important for simulating chemical equilibria and systems where molecules can be exchanged with either an external reservoir (which is too large to be simulated explicitly) or between two subsystems. Just like the pressure p, the chemical potential μ is an intensive variable that requires a refined approach to be calculated during a simulation (or after, if desired). An effective and practical approach is the computational implementation of the *test-particle insertion method* or *Widom Sampling* acknowledged to B. Widom [28]. It allows for an estimation of the excess chemical potential for an individual thermodynamic state of the system.

Starting from the Helmholtz free energy $A_N(V,T)$ of an N-particle system in a volume V at a temperature T, the chemical potential μ per particle can be written as

$$\mu(\rho,T) \equiv \left(\frac{\partial A}{\partial N}\right)_{V,T} \approx \frac{\Delta A}{\Delta N} =\approx A_{N+1}(V,T) - A_N(V,T) = -k_B T \ln\left(\frac{Q_{N+1}}{Q_N}\right), \tag{2.25}$$

where $\rho \equiv N/V$ is the density and $Q_N(V,T)$ the canonical partition function; this relation is exact in the thermodynamic limit of large N at fixed density. The partition functions Q_N consists of the corresponding configuration integrals

$$Q_N(V,T) = \frac{1}{N!\Lambda^{3N}} \int_V d\vec{r}^N e^{-\beta U_N(\vec{r}^N)}, \tag{2.26}$$

where $k_B T(=\beta^{-1})$ and $\Lambda = h/(2\pi/mk_BT)^{1/2}$ are the so-called *thermal energy* and *thermal wavelength*, respectively. Inserting the expression for $Q_N(V,T)$ from (2.26) into the chemical potential approximation found in equation (2.25) becomes

$$\beta\mu = \ln\left[\frac{(N+1)\Lambda^3}{V}\right] - \ln\left(\frac{\int_V d\vec{r}^{N+1} e^{-\beta U_{N+1}}}{\int_V d\vec{r}^{N+1} \int_V d\vec{r}^N e^{-\beta U_N}}\right). \tag{2.27}$$

$\beta\mu$ may be rewritten as the sum of an ideal gas component $\beta\mu_{id}$ and an excess contribution $\beta\mu_{ex}$

$$\beta\mu_{Id} = \ln\left[\frac{(N+1)\Lambda^3}{V}\right], \tag{2.28a}$$

$$\beta\mu_{ex} = -\ln\left(\frac{\int_V d\vec{r}^{N+1} e^{-\beta U_{N+1}}}{\int_V d\vec{r}^{N+1} \int_V d\vec{r}^{N} e^{-\beta U_N}}\right). \tag{2.28b}$$

By having the $(N+1)-th$ particle singled out, the two-body interatomic potential function may be rewritten as

$$U_{N+1}(\vec{r}^{N+1}) \equiv U_N(\vec{r}^{N}) + \phi(\vec{r}^{N}, \vec{r}^{N+1}), \tag{2.29}$$

where ϕ is the potential energy of the $(N+1)-th$ particle at $\vec{r}^{N+1}$, embedded in the system formed by the remaining N molecules. From this, the excess chemical potential (2.28b) takes the form

$$\beta\mu_{ex} = -\ln\left(\frac{\int_V d\vec{r}^{N+1} \int_V d\vec{r}^{N} e^{-\beta U_N(\vec{r}^{N})} e^{-\beta\phi(\vec{r}^{N},\vec{r}^{N+1})}}{\int_V d\vec{r}^{N+1} \int_V d\vec{r}^{N} e^{-\beta U_N \vec{r}^{N}}}\right) \tag{2.30}$$

$$= -\ln\left(\frac{\int_V d\vec{r}^{N+1} \langle e^{-\beta\phi}\rangle}{\int_V d\vec{r}^{N+1}}\right) = -\ln\left(\langle\langle e^{-\beta\phi}\rangle_N\rangle_{\vec{r}^{N+1}}\right), \tag{2.31}$$

where the first average $\langle\cdots\rangle_N$ is over the configurations $\vec{r}^{N}$ of the N-particle system, and the subsequent average $\langle\cdots\rangle_{\vec{r}_{N+1}}$ over randomly chosen propositions of the $(N+1)-th$ particle during the canonical distribution. The algorithm can be described as follows:

Algorithm 2 *Test-particle insertion* method

1. Perform a regular NVT Monte Carlo simulation
   (a) Fix the current positions and calculate the potential energy of the system.
   (b) Generate a total of n random positions within the simulation box.
   (c) Calculate the potential energy of a probe particle in each of the n positions.
   (d) Average the Boltzmann factor over the insertions and keep track of the output.
   (e) Resume the simulation.
2. Repeat (a - e) until convergence for a large enough amount of iterations.
3. Average the output by the number of iterations.

4. The negative natural logarithm of the averages results in the excess chemical potential of the system.

Note: The number of random positions n may depend on the system as well as the iterations.

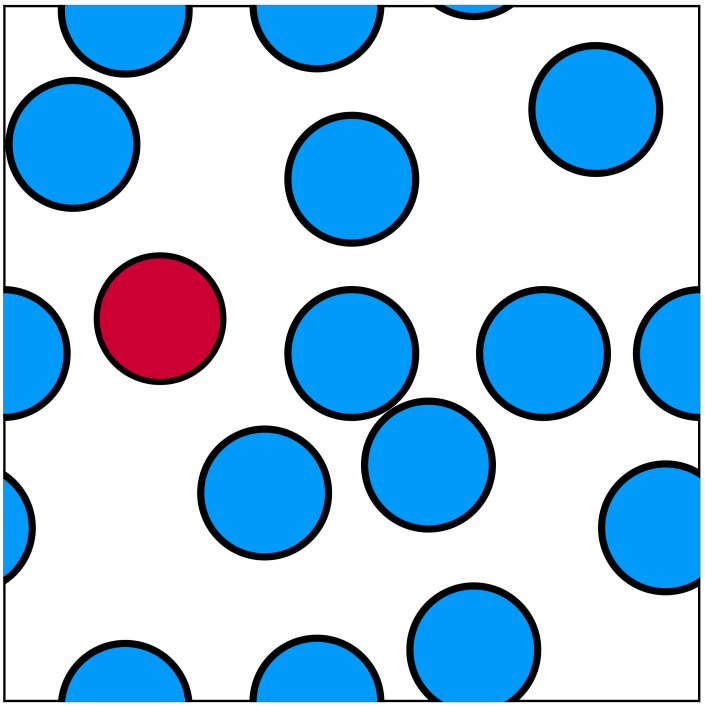

Figure 2.6: Probe particle (found in red) inserted in a random position of a bidimensional system. Once it's energy is calculated, it proceeds to be relocated in a new random position.

This method has convergence issues for high-density systems given the saturation of molecules. In the next chapter 2.5.1, a revamp for this kind of tricky situation will be introduced.

2.5 Grand Canonical Ensemble

The *Grand canonical* ensemble has flexibility concerning N (thus the density of the system is allowed to fluctuate by creating and/or destroying molecules), while fixing the temperature T, volume V and chemical potential μ. This makes it an ideal ensemble for adsorption studies, where it's possible to calculate the average number of adsorbed molecules as a function of pressure and temperature of the reservoir with which the material is in contact.

It's also suitable for the investigation of phase equilibria and proves a useful tool in the study of liquid mixtures, especially when chemically reacting species are present [29]. In the experimental setup, the adsorbed gas is in equilibrium with the gas in the reservoir, provided that the temperature and chemical potential of the gas inside and outside the adsorbent are equal.

As previously inspected, the Metropolis scheme could not be used to determine the thermodynamic properties of a system that depend explicitly on the configurational integral. However, although it cannot be used to measure free energies directly, it can be used to calculate the difference in free energies between two possible states of an N-body system. This fact was exploited by Norman and Filinov in a 1969 work [30], and later extended and improved independently by Adams [29, 31] and Rowley *et. al.* [32]. Initiating from the *grand canonical* partition function

$$\Xi(\mu, V, T) = \frac{1}{N!}(V/\Lambda^3)^N e^{\beta\mu N} \int_V d\vec{r}^N e^{-\beta U(\vec{r}^N)}, \tag{2.32}$$

the probability density derived from the previous partition function can be sampled by a Metropolis Monte Carlo method.

In addition to trial moves for particle displacement (acceptance probability for such moves remains the same as in equation (2.22)), attempts for insertion and removal of molecules from the reservoir are also introduced. The insertion of a particle at a randomly selected position $\vec{r}^{N+1}$ is accepted with probability

$$A(N \to N+1) = \min\left\{1, \frac{V}{\Lambda^3(N+1)} e^{-\beta\left[U(\vec{r}^{N+1}) - U(\vec{r}^N) - \mu\right]}\right\}, \tag{2.33}$$

while the acceptance criteria for the removal of a randomly chosen particle is

$$A(N \to N-1) = \min\left\{1, \frac{\Lambda^3 N}{V} e^{-\beta\left[U(\vec{r}^{N-1}) - U(\vec{r}^N) + \mu\right]}\right\}. \tag{2.34}$$

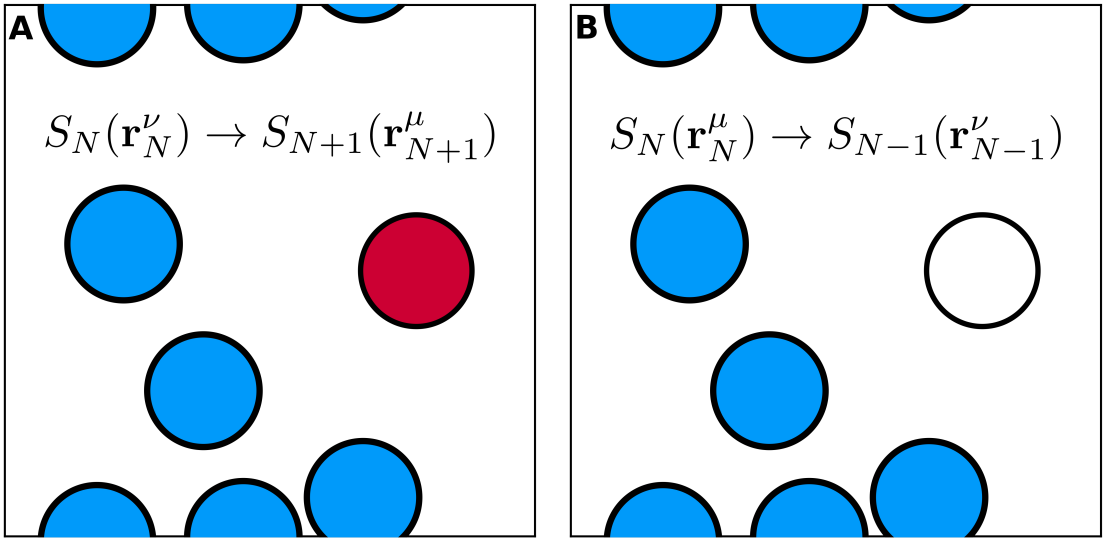

Figure 2.7: **(A)** Insertion attempt of a new particle (found in red) in a bidimensional system. **(B)** Removal attempt of an already existing particle (found in white) in a bidimensional system.

Algorithm 3 μVT Metropolis Monte Carlo

1. Generate a uniform random number $\lambda \in [1, 2, 3]$
2. If $\lambda = 1$ and $N > 1$
   - Perform a particle displacement according to the canonical ensemble Metropolis method, like in Algorithm 1.
3. If $\lambda = 2$
   (a) Insert a particle at a randomly selected location within the simulation box.
   (b) Calculate energy change $\Delta U = U(\vec{r}^{N+1}) - U(\vec{r}^{N})$
   (c) Generate a uniform random number $0 \leq \eta \leq 1$
   - If $\eta \leq \frac{V}{N+1} e^{-\beta[\Delta U - \mu]}$, accept the insertion.
   - Else, reject the insertion.
4. If $\lambda = 3$ and $N \geq 1$
   (a) Select a random particle to be removed.
   (b) Calculate energy change $\Delta U = U(\vec{r}^{N-1}) - U(\vec{r}^{N})$
   (c) Generate a uniform random number $0 \leq \eta \leq 1$
   - If $\eta \leq \frac{N}{V} e^{-\beta[\Delta U + \mu]}$, accept the removal.
   - Else, reject the removal.
5. Sample thermal and/or structural properties of interest.
6. Repeat from step **1.** until acceptable convergence criteria has been achieved.

Canonical and Grand Canonical Monte Carlo are complementary in some way: the first one is more suitable for the study of solids and dense liquids, while the second one is better for low-density liquids and the vapor phase. When the compressibility of the fluid is large, the tendency for Canonical Monte Carlo to suppress density fluctuations is an awkward source of error and the μVT ensemble is then clearly superior [29].

2.5.1 Cavity Biased

The efficiency of the *grand canonical* Monte Carlo algorithm rapidly deteriorates as the density increases (for dense fluids near their fluid-solid transition), becoming an impractical method due to successful attempts of a particle insertion being extremely rare. In this section, a simple biasing technique that significantly increases the efficiency of the insertions is presented, further yielding a significant increase in the density limit of the method.

The *Cavity-biased Grand Canonical Monte Carlo* procedure attempts insertions of new molecules only at points where a cavity of suitable radius R_c exists (such radius depends on the potential function employed and its allowance for molecules to overlap), instead of randomly selected points. These cavities can be identified, for instance, via the *Excluded Volume Map Sampling (EVMS)* technique [33] which comprehends the region in which the insertion of a molecule yields a plausible change in the potential energy of interaction.

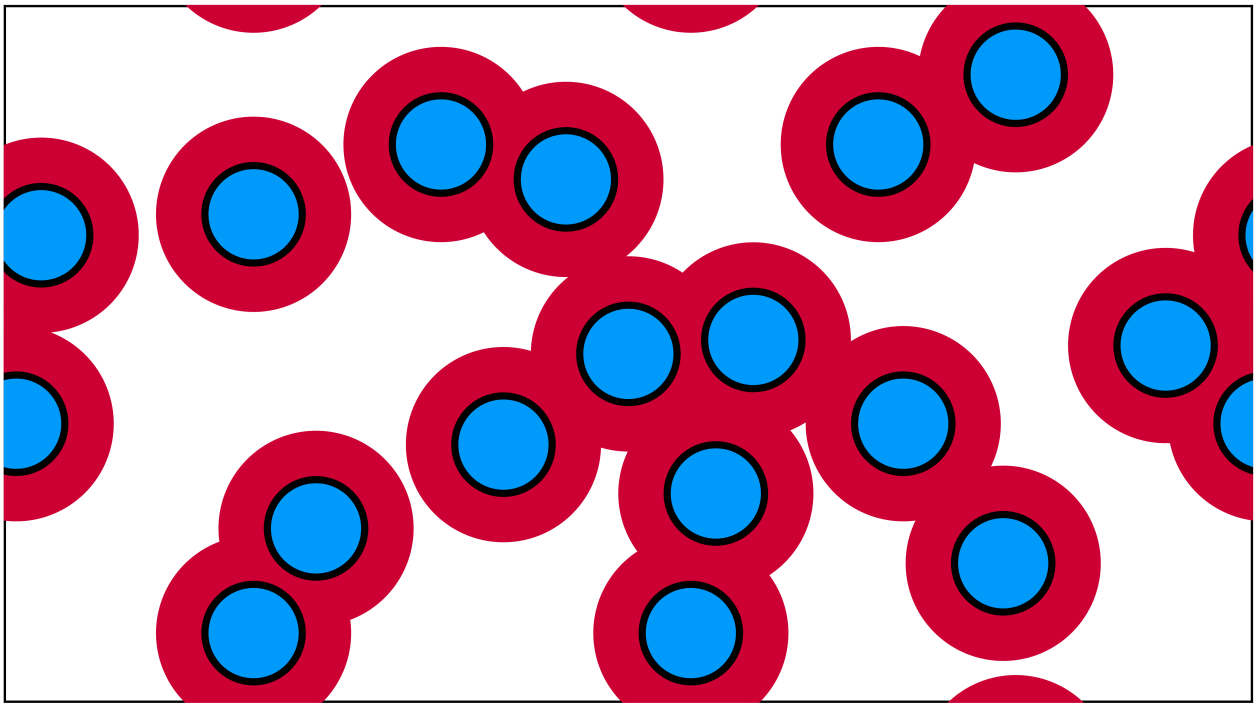

Figure 2.8: Schematic diagram of the excluded volume of a configuration of a bidimensional system. The blue shading indicates the effective hard core and the red shading illustrates the excluded volume of the molecules. EVMS selects probe particle positions uniformly from the uncolored region.

A cavity probability Γ_N given as the ratio of non-excluded volume and total volume is defined for each value of N in the simulation. An analytical approach may represent a difficult and laborious task to execute, but an estimation may be carried out by generating N_t uniformly distributed test points and finding the fraction of them that are in a suitable cavity, as well as a possible location where a new particle can be inserted. To improve estimation, Γ_N is updated

along with the simulation via

$$\Gamma_N = \frac{\text{nonexcluded volume}}{\text{total simulation volume}} \approx \left\langle \frac{N_i}{N_t} \right\rangle \tag{2.35}$$

where N_i is the number of points inside a cavity (points residing in the uncolored region of figure 2.8) out of N_t attempts. It's important to keep track of test points in the nonexcluded volume, since this are the favorable positions for the new insertions.
Conventionally, the creation of the test points for each configuration is achieved either by random generation [34] or by implementing a uniform grid [35]. Figure 2.9 shows a comparison between these two approaches for a generic high-density system, where the random one displays significant fluctuations compared to the ordered-one since the simulation spends little time in low-density states and the randomness diminishes convergence of Γ_N. In the high-density limit, both curves are similar since more data is obtained for a narrower window of sampled densities.

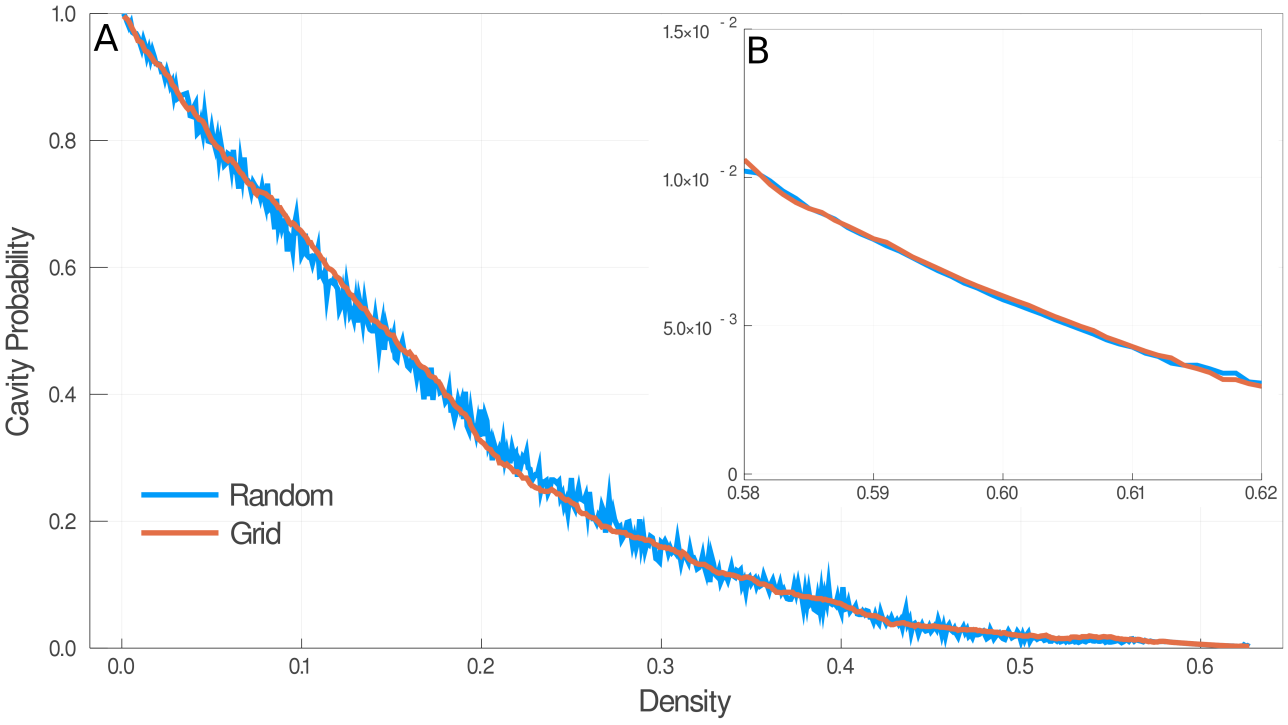

Figure 2.9: **(A)** Cavity probability comparison for a random and systematic grid methodology evolution along with the simulation. **(B)** Zoom in to the high-density domain, where most of the simulation takes place.

Implementation of the cavity probability induces a slight modification to the acceptance probability for the insertion and removal of molecules. Based on all of the above considerations, the algorithm consists of the following steps described in the original work of Mezei:

Algorithm 4 *Cavity-Biased μVT Monte Carlo*

1. Generate a uniform random number $\lambda \in [1, 2, 3]$
2. If $\lambda = 1$ and $N > 1$
   - Perform a particle displacement according to the canonical ensemble Metropolis method, like in Algorithm 1.
3. If $\lambda = 2$
   (a) Generate N_t points and find the amount that reside inside a cavity.
   (b) Update the estimation of Γ_N.
   (c) If at least one point was found to be in a cavity:
      i. Insert one particle at one of the points which was found to be in a cavity.
      ii. Calculate energy change $\Delta U = U(\vec{r}^{N+1}) - U(\vec{r}^{N})$
      iii. Generate a uniform random number $0 \leq \eta \leq 1$
      iv. If $\eta \leq \frac{\Gamma_N V}{N+1} e^{-\beta[\Delta U - \mu]}$, accept the insertion.
      v. Else, reject the insertion.
   (d) If no point was found to be in a cavity, proceed to a regular Grand Canonical Monte Carlo insertion like in Algorithm 3, step 3.
4. If $\lambda = 3$ and $N \geq 1$
   (a) Select a random particle to be removed.
   (b) Calculate energy change $\Delta U = U(\vec{r}^{N-1}) - U(\vec{r}^{N})$
   (c) Generate a uniform random number $0 \leq \eta \leq 1$
   (d) If $\eta > (1 - \Gamma_{N-1})^{N_t}$
      i. Generate a uniform random number $0 \leq \eta \leq 1$
      ii. If $\eta \leq \frac{N}{\Gamma_{N-1} V} e^{-\beta[\Delta U + \mu]}$, accept the removal.
      Note: In case $N - 1$ has not been sampled yet, Γ_{N-1} is extrapolated from the nearest values.
   (e) If $\eta \leq (1 - \Gamma_{N-1})^{N_t}$
      - Proceed to a regular Grand Canonical Monte Carlo deletion like in Algorithm 3, step 4.
5. Sample thermal and/or structural properties of interest.
6. Repeat from step **1.** until acceptable convergence criteria has been achieved.

2.6 Structural and Thermophysical Quantities

Fluid's structure is characterized by a set of distribution functions, the simplest of which is the pair distribution function $g(r)$ (commonly known as radial distribution function), which calculates the number of pair-molecules separated by a distance r.
For a three-dimensional system, the site-site distribution function is directly calculated from the simulation by collecting histograms of the number of all pairs of respective sites, having bin i store the number of pairs which lie in a distance range between r_i and $r_i + \Delta r$. From this pair number, the density of the sites in spherical shells of radius r_i and thickness Δr is estimated and normalized by the mean number density in each shell.

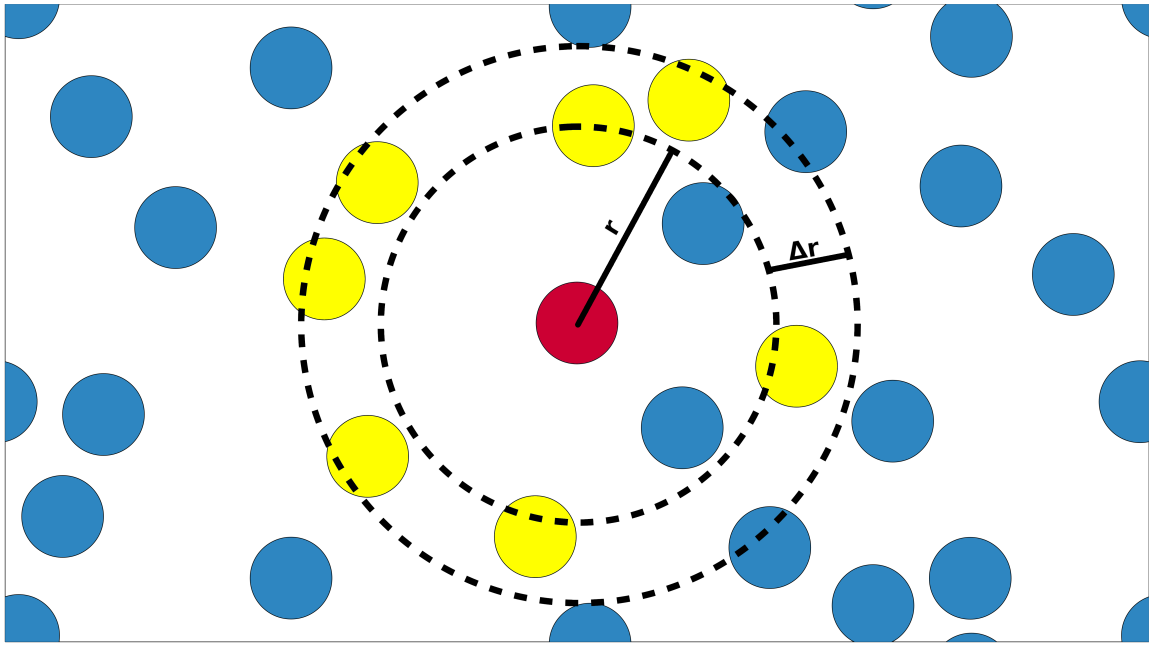

Figure 2.10: Radial distribution function $g(r)$ calculation, where the dashed black lines concentric to the red particle delimit the radial bins. Molecules inside this bin are identified in yellow.

The number of molecules between r and $r + \Delta r$ about a central molecule is given by $4\pi r^2 \rho g(r)$, thus

$$\int_0^\infty dr\ \rho g(r) 4\pi r^2 = N - 1 \approx N. \tag{2.36}$$

Clearly, the limit behavior of the radial distribution function goes as $g(r \to 0) = 0$ since molecules become effectively "hard" for small distances, and $g(r \to \infty) = 1$ since the influence of the molecule at the origin diminishes as r becomes large.

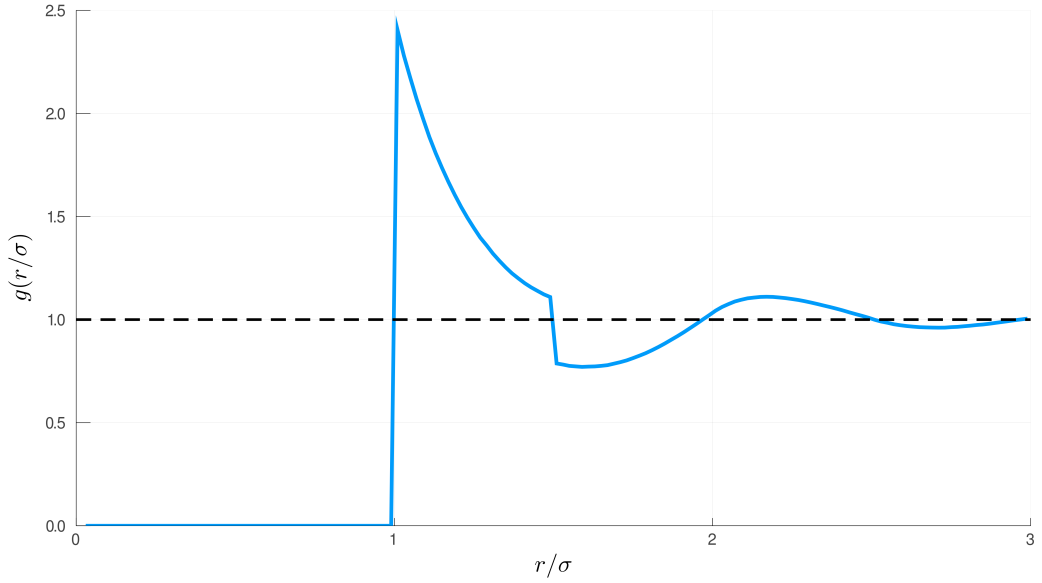

Figure 2.11: Radial distribution function for the square well model fluid at $T^* = 3.0$, $\rho^* = 0.6$, where the limiting behaviors $g(r \to 0) = 0$ and $g(r \to \infty) = 1$ are appreciated.

This pair distribution function offers a description of the density variation as a function of the site to site separation, giving a hint on the type of matter with substantial differences between solids, liquids and gases:

- **Solids**: Periodic structures with molecules fluctuating near their lattice positions. The structure is very specific over a long range, with discrete peaks at values of $\sigma, \sqrt{2}\sigma, \sqrt{3}\sigma$. Each peak has a broadened shape which is caused by molecules vibrating around their lattice sites.

- **Liquids**: Due to their ability to move dynamically liquids do not mantain a constant structure and lose all of their long range structure. For long distances, the molecules become independent of each other and the distribution returns to the bulk density.

- **Gases**: No regular structure with only a single molecule neighboring the tagged one, rapidly decaying to the bulk density of a gas. The behavior of the function is fairly simple:

$$g(r) \begin{cases} = 0 & r < \sigma \\ > 1 & \sigma < r < 2\sigma \\ \approx 1 & r > 2\sigma \end{cases} \tag{2.37}$$

Code 2.3 calculates radial distribution function by first measuring distances between sites $\vec{r_i}$ and $\vec{r_j}$ subjected to Periodic Boundary Conditions 2.2 and to a cutoff distance r_{Cut} typically of the order of 3σ. The corresponding bins are normalized by the density of the system multiplied by the volume of the spherical shell, symbolically expressed as $\rho 4\pi r^2 dr$.

```
function Distribution(N_Bins, L, Density, x, y, z, R_Cut = 3.)
  Δr = R_Cut / N_Bins;
  N = length(x);
  g_r = zeros(Float64, N_Bins);
  for i = 1:length(x) - 1
    for j = i + 1:length(x)
      Δx, Δy, Δz = x[i] - x[j], y[i] - y[j], z[i] - z[j];
      Δx = PeriodicBoundaryConditions!(L, Δx);
      Δy = PeriodicBoundaryConditions!(L, Δy);
      Δz = PeriodicBoundaryConditions!(L, Δz);
      r2 = Δx^2 + Δy^2 + Δz^2;
      if r2 < R_Cut^2
          Bin_Index = convert(Int64, floor(√r2 / Δr));
          g_r[Bin_Index] += 2;
      end
    end
  end
  g_r ./= (4π × N × (Bin_Index * Δr)^2 × Δr × Density)
  return g_r
end
```

Code 2.3: Algorithm for the calculation of the radial distribution function *g(r)*. Pseudo-code based in the Julia language 1.3.1.

If the potential energy of the N-body system is pair-wise additive, then

$$U_N(\vec{r_1}, \cdots, \vec{r_N}) = \sum_{i=1}^{N-1} \sum_{j=i+1}^{N} U(|\vec{r_i} - \vec{r_j}|), \tag{2.38}$$

and all the thermodynamic functions of the system can be written in terms of $g(r)$. D. A McQuarrie [36] expresses the total energy E as

$$\frac{E}{Nk_BT} = \frac{3}{2} + \frac{\rho}{2k_BT} \int_0^\infty dr\, U(r) g(r) 4\pi r^2, \tag{2.39}$$

whereas the pressure equation takes the form

$$\frac{P}{k_BT} = \rho - \frac{\rho^2}{6k_BT} \int_0^\infty dr\, \frac{dU}{dr} g(r) 4\pi r^3. \tag{2.40}$$

Furthermore, it is possible to link the thermodynamic properties of the fluid to X-ray or light scattering studies through the *structure factor* function $S(k)$, where k is the wave vector associated with the scattered waves. Such association is achieved from the Fourier transform of

$g(r)-1$ (see reference [36] for the complete outline of the relation between the radial distribution function and the scattering of electromagnetic radiation):

$$S(k) = 1 + \rho \int dr\ (4\pi r^2)[g(r) - 1]\frac{sin(kr)}{kr}. \tag{2.41}$$

Chapter 3

From Bulk to a Confined Fluid

Transition from bulk fluids into a confined one is straightforward with the implementation of a molecular interface structure that enables the study of equilibrium properties (like density distribution, the order of the molecules, the pressure at the wall, etc.) of fluids in terms of the interface structural roughness, including feed-back effects from the fluid properties to the interface structure.

For this study, the so mentioned molecular interface structure consists of a planar interface layer (simulating a slit-like pore) of dimensions $L_x \times L_y \times L_z$ located at $\pm z = L_z/2$ with imposed

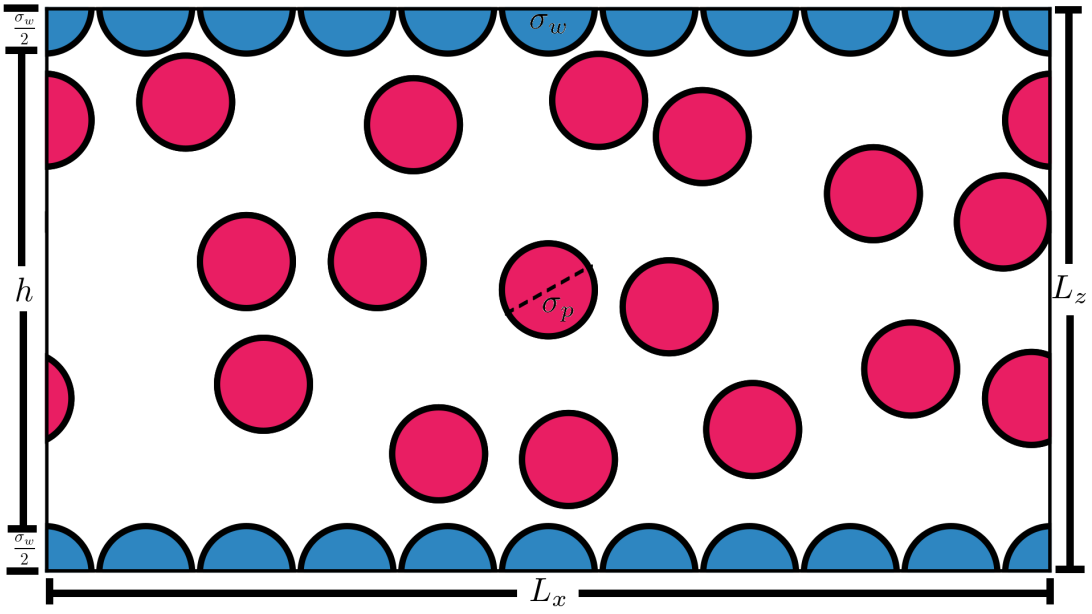

Figure 3.1: Bidimensional representation for the slit-like pore model with periodic continuation along the x- and y-directions. σ_p and σ_w represent the fluid and wall particles diameter, respectively. This project implements $\sigma_p = \sigma_w = \sigma$.

periodic boundary conditions along the x- and y-axis, as shown in figure 3.1. The design of the planar layers could be conceived as structureless or smooth walls, but instead, an arrangement of particles in an hexagonal closed packing is implemented and displayed in figure 3.2.

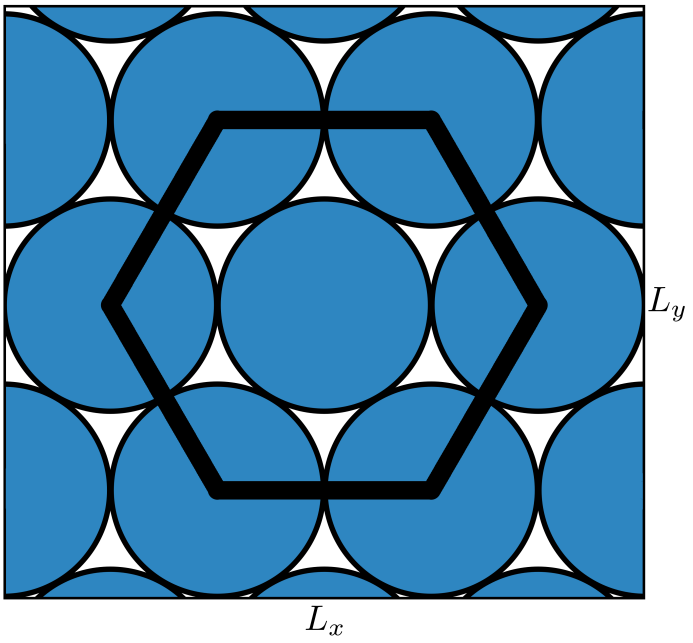

Figure 3.2: Hexagonal arrangement of molecules generate the confining interface that is located at $z = \pm L_z/2$.

The confinement of the fluid requires to take new things into consideration and redefine some previous concepts for bulk fluids, with the main changes focusing on the molecular interactions, pressure and distribution profiles.

3.1 Molecular Interactions

The combination of the infinitely extended slits enclosing the fluid form a system with three individual energetic contributions:

- **Particle - Particle interaction (P-P)**: If the intermolecular forces are restricted to site-site models with N interaction sites (simulating atoms or model particles) per fluid molecule, as is done in most simulations of confined fluids, the potential energy U_{P-P} is generally written as

$$U_{P-P} = \frac{1}{2} \sum_{i=1}^{N} \sum_{j>i} \sum_{\alpha} \sum_{\beta} U_{i\alpha j\beta}(\mid \vec{r}_{i\alpha} - \vec{r}_{j\beta} \mid), \tag{3.1}$$

where $U_{i\alpha j\beta}(\mid \vec{r}_{i\alpha} - \vec{r}_{j\beta} \mid)$ is the site-site potential between site α of particle i and site β of particle j, which depends on the scalar distance between the sites.

- **Wall - Particle interaction (W-P)**: Due to the atomistic nature of the walls, the interaction depends only between the fluid particles inside the pore and the center of the wall particles. This is represented as

$$U_{W-P} = \frac{1}{2} \sum_{w} \sum_{i=1}^{N} \sum_{\alpha} U_{w,i\alpha}(\mid \vec{r}_{i\alpha} - \vec{r}_{w} \mid) \tag{3.2}$$

where $U_{w,i\alpha}$ is the energy between a wall-particle w and a site α of the $i-th$ particle.

- **Wall - Wall interaction (W-W)**: In general it is assumed that the sites in the different walls may have interactions between them. As such, a particular form of such interaction must be defined, as well as its contribution to the total energy:

$$U_{W-W} = \frac{1}{2} \sum_{w} \sum_{v} U_{wv}(\mid \vec{r}_{w} - \vec{r}_{v} \mid), \tag{3.3}$$

Therefore, the total potential energy of the pore-fluid system is:

$$U_{Total} = U_{P-P} + U_{W-P} + U_{W-W}. \tag{3.4}$$

3.2 Pressure

Uniform mechanical pressure in confined fluids does not exist in general, instead a position and direction space-dependent tensor must be implemented for the calculation. Specifically for slit-like pores, pressure splits into two contributing pressures:

- Tangential Pressure P_T: Consists of the average mechanical pressure parallel to the walls and has the meaning of a thermodynamic pressure in phase equilibria comprising bulk and confined fluids [37]. Implementation of the Irving-Kirkwood prescription for the tangential pressure [38] leads to

$$P_T(z) = \rho(z) k_B T - \frac{\bar{A}_T(z)}{S_{xy}}, \tag{3.5}$$

where

$$A_T(z) = \sum_{i=1}^{N-1} \sum_{j=i+1}^{N} \frac{x_{ij}^2 + y_{ij}^2}{2r_{ij}} \left[\frac{dU(\vec{r}_{ij})}{dr_{ij}} \right] \xi_T(z, z_i, z_j), \tag{3.6}$$

and

$$\xi_T(z, z_i, z_j) = \frac{1}{|z_{ij}|} \left[H(z - z_i) - H(z - z_j) \right]. \tag{3.7}$$

Here, $\rho(z)$ is the density of the adsorbed phase at a distance z from the surface; S_{xy} is the area of the simulation cell in the x-y plane parallel to the surface; x_{ij}, y_{ij} are projections of the separation distance r_{ij} between molecules i and j onto the corresponding axes and H(x) is the Heaviside function. The line above A_T denotes time average.

- Normal Pressure P_N: It's the average mechanical pressure parallel to the walls. The Irving-Kirkwood prescription for the normal pressure results in

$$P_N(z) = \rho(z) k_B T - \frac{\bar{A}_N(z)}{S_{xy}}, \tag{3.8}$$

where

$$\bar{A}_N(z) = \sum_{i=1}^{N-1} \sum_{j=i+1}^{N} \frac{z_{ij}}{r_{ij}} \frac{dU(r_{ij})}{dr_{ij}}. \tag{3.9}$$

Contributions to the normal pressure at a distance z_0 are only feasible if the pair of molecules i and j form a vector that crosses in some fashion the plane found in $z = z_0$ [38]. In simpler terms, if both molecules aren't found between the plane at the height of the measurement, these do not contribute to the normal pressure.

The problem of the behavior of the pressure as a function of the distance from the walls is an actual problem in experimental studies of planar interface structures, like biologically active phospholipid bilayers [37].

3.3 Distribution Profile

The definition of a radial distribution function as implemented in chapter 2.6 is no longer valid in confined systems, given the periodicity violation along the z-direction.

Instead, density profiles $\rho(z)$ across the walls are mapped by measuring and averaging the local density along the z-coordinate; and once it's properly normalized with the density of the

corresponding ideal gas, the wall-particle or wall-fluid "pair" correlation function is obtained. The basic step for such calculations is now the construction of rectangular bins parallel to the walls of the slit, like in figure 3.3, where particles inside the bin are purposely highlighted in yellow.

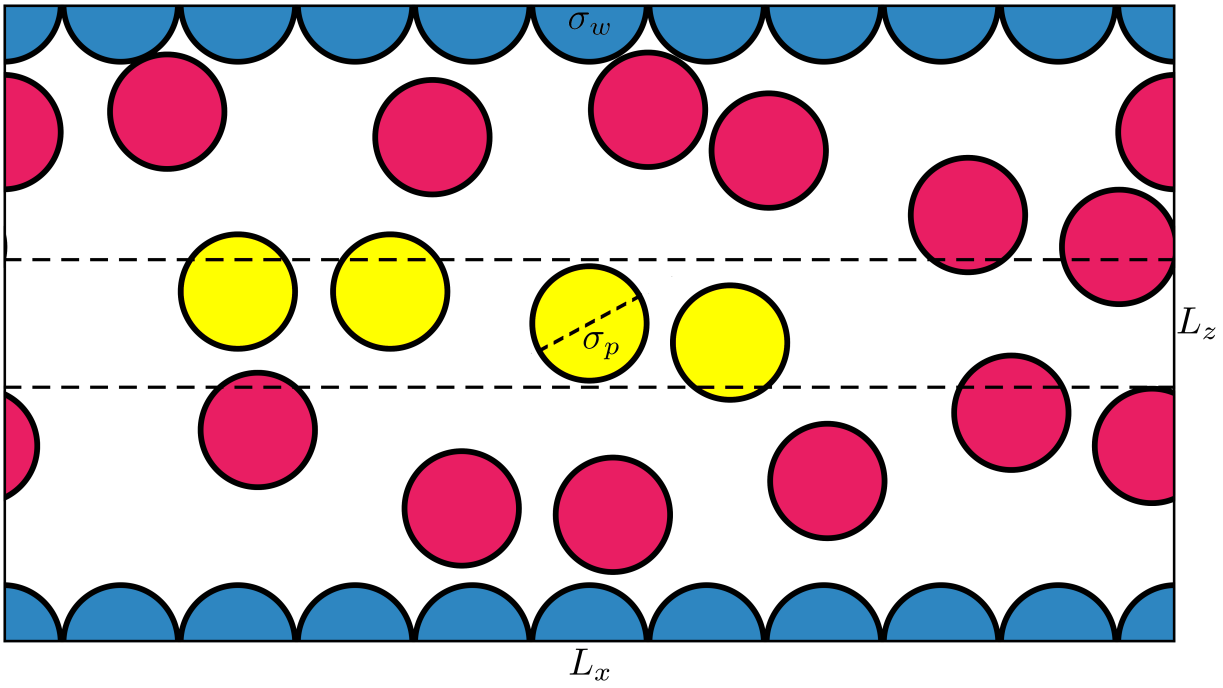

Figure 3.3: Bidimensional representation of the rectangular bins parallel to the slit-like walls, where yellow particles are found inside the corresponding bin.

The algorithm is much simpler than it's bulk analog, given the constant volume between bins. A normalization with ρ_{Bulk} is implemented as an aid for comparisons.

```
function Density_Profile(N_Bins, Lz, z, V, ρBulk)
  Δz = Lz / N_Bins;
  g_z = zeros(Float64, N_Bins);
  for i = 1:length(z)
      Bin_Index = convert(Int64, ceil( (Lz / 2. - z[i]) / Δz) );
      g_z[Bin_Index] += 1;
  end
  g_z .*= N_Bins / ( V * ρBulk);
  return g_z
end
```

Code 3.1: Pseudo-code for the calculation of distribution profiles by creating rectangular prisms enclosing a certain number of molecules.

Implementation of the previous code displays an example of a distribution profile for a confined system in the figure 3.4. It's easily perceived that the main conglomeration of particles is close to the walls in the proximities of $\pm 4.5\sigma$, with this behavior slowly fading as the walls have no real contribution in the midst of the pore.

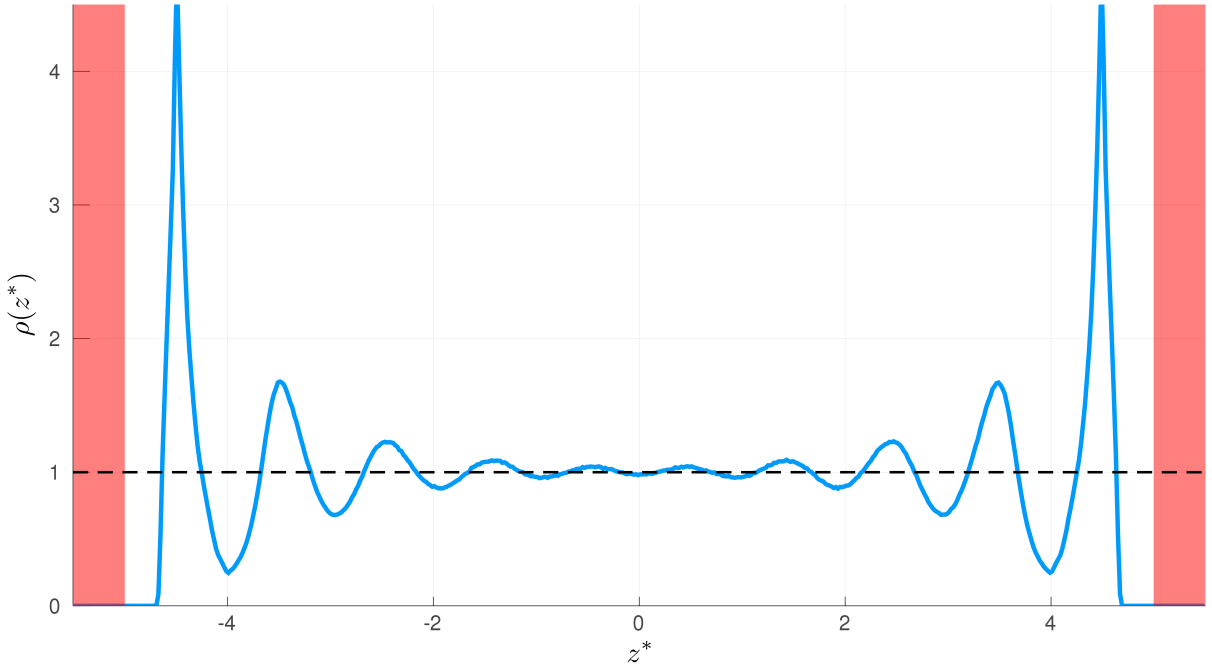

Figure 3.4: Distribution profile for a square-well fluid with parameters $L_z = 10\sigma, T = 1.5, \rho_{Bulk} = 0.6$ confined within square-well slit-like walls. Red shaded area illustrates wall's location.

Although no direct relation of the density distribution with thermodynamic variables of the system can be easily achieved, it's not of great concern as this is justified by the implementation of Monte Carlo algorithms given the fact that the averages are not directly affected by the geometry of the system.

Chapter 4

Discussion

The principal objective of this investigation is to study the adsorption properties of Square-Well (SW) interacting fluid molecules under slit-like confinement of hexagonally arranged atomistic walls. The simple, but effective, SW interacting potential has been selected due to its substantial theoretical importance and interest in the study of systems with varying potential range, as it is the simplest model which includes the presence of attractive and repulsive forces that can represent three limiting cases: The hard-sphere, short-range sticky-sphere and long-range van der Waals interactions, all with a single potential function.

To achieve this, a piece-wise potential energy function $U^*(r^*)$ for molecules separated a distance $\vec{r}^*$ is defined as

$$U^*(r^*) = \begin{cases} +\infty & \text{if } r^* < 1, \\ -1 & \text{if } 1 \leq r^* < \lambda^*, \\ 0 & \text{if } r^* \geq \lambda^*; \end{cases} \tag{4.1}$$

where the mandatory dependence on the parameters $\sigma, \lambda, \epsilon$ is no longer explicit due to the hereinafter exploiting of reduced units (refer to Appendix B where the purpose and practicality of these units is discussed). These latent parameters are the hard-sphere diameter of the fluid's molecules σ, the range of interaction of the potential-well λ and the depth of the potential-well ϵ; these are appreciable in figure 4.1.

These play an important role as their limiting cases lead to multiple interactions:

- $\lambda \to 1$ and/or $\epsilon \to 0$: (i. e., $T^* \to \infty$) the SW fluid converges to the hard-sphere (HS) fluid.

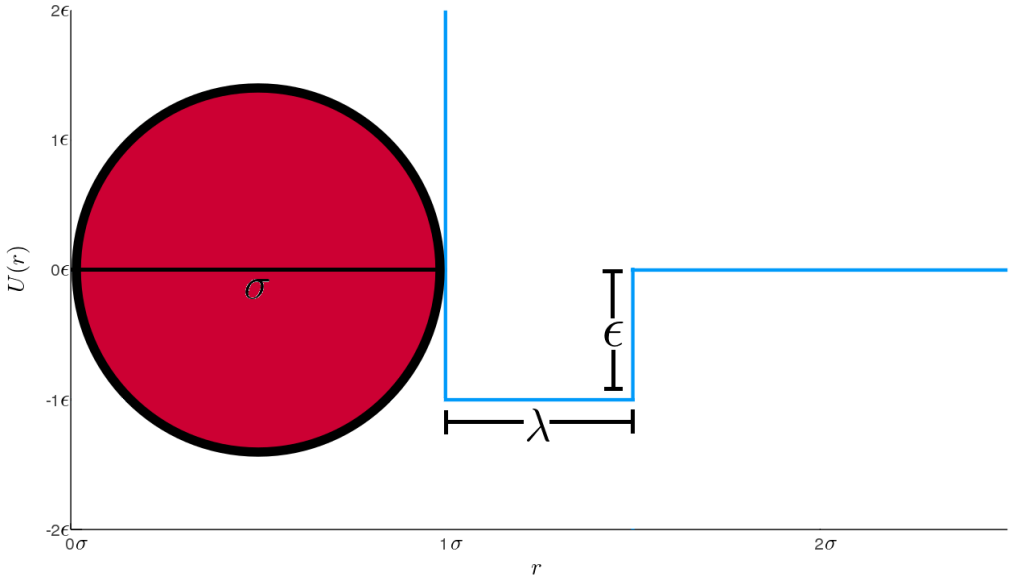

Figure 4.1: Visual representation of the piece-wise Square Well potential function with its corresponding parameters σ, λ and ϵ.

- $\lambda \to 1$ and $\epsilon \to \infty$: (i. e., $T^* \to 0$) the SW fluid converges to the sticky-hard-sphere (SHS) fluid.
- $\epsilon \to \infty$: the SW fluid converges to the sticky-sphere (SS) fluid.

Given the piece-wise nature of the SW potential, calculation of the system's pressure via Virial expansion is not conveniently feasible for non-continuous functions in their domain. Although this intensive property might be of interest for the study, it will be omitted for now.

Despite the mathematical simplicity of the SW potential, no analytical solution of the conventional integral equations for fluids is known. Therefore, structural quantities such as the radial distribution function and the structure factor are commonly obtained via Monte Carlo simulations, numerical solutions of integral equations or perturbation theory. [39].

For the study of adsorption problems, chemical potential is mandatory as it dictates the energy that can be absorbed or released as the number of molecules of the given species changes. Its calculation is usually straightforward via test-particle insertions in Monte Carlo simulations on the canonical ensemble for systems found above the liquid-vapor coexistence binodal, a curve that denotes the condtion at which two distinct phases may coexist. This phase equilibria for pure fluids of SW interacting molecules has been broadly calculated for multiple ranges of interaction λ [40]. The most common employed range of interaction corresponds to $\lambda = 1.5$ and its vapor-liquid coexistence curve is displayed in figure 4.2, where the examination of the pressure-temperature curve's endpoints designate the necessary conditions under which a

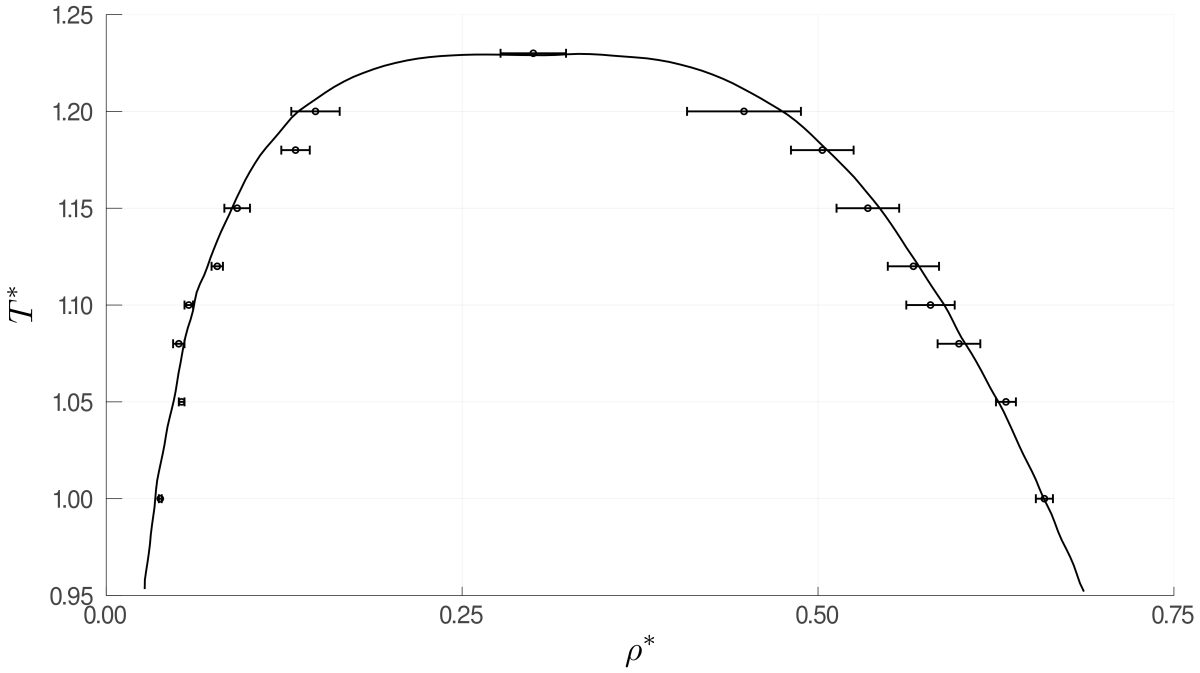

Figure 4.2: $T^* - \rho^*$ vapor-liquid coexistence curve for the square-well fluid with a range of interaction $\lambda = 1.5\sigma$. Dataset extracted from *Phase equilibria and critical behavior of square-well fluids of variable width by Gibbs ensemble Monte Carlo simulation* by L. Vega *et. al.* [40].

liquid and its vapor can coexist and provides an estimation to its critical point, corresponding for the $\lambda = 1.5\sigma$ case to the critical temperature $T_C^* = 1.219 \pm 0.008$ and critical density $\rho_C^* = 0.3 \pm 0.0023$. These values are of remarkable importance given the impossibility to examine the phase equilibria in the region very near the critical point with any conventional technique[1] due to large density fluctuations, consequently, the true limiting behavior can't be directly studied.

There's no general vapor-liquid coexistence curve for fluids under confinement constrictions, therefore, the best guess is to elect temperatures and densities further away from the critical point and above the binodal, as fluids confined by adsorbing walls will, in general, condense before the critical point is reached in a phenomenon called capillary condensation [41]. Therefore, an election of temperatures $T^* \in [1.5, 2.0, 2.5, 3.0] > T_C^*$ in multiple density scopes $\rho^* \in [0.1, 0.3, 0.6]$ represents a good enough exploration approach for the chemical potential of the systems.

Extrapolation of these dozen of systems to the canonical ensemble is carried out by the designed *Canonical.jl* code which is obtainable from my GitHub repository (more details in Appendix C.2). An extensive set of exhaustive runs allowed to identify the optimal parameters

[1] *Vega et. al.* implemented the Gibbs ensemble technique where the coexisting vapor-liquid and liquid phases are monitored simultaneously as separate subsystems without the presence of an interface [40].

to achieve conclusive converging results compared to those published by Smith *et. al.* [42], Adams *et. al* [29, 31] and Frenkel *Et. al.* [43]. These parameters are recapped in table 4.1 and a proof of their convergence is appreciable in figure 4.3 where the calculated chemical potential μ^* and average chemical potential $\langle \mu^* \rangle$ of an arbitrary system display narrow fluctuations as amount of steps increases.

Table 4.1: Optimal parameters for the simulations implemented in the code *Canonical.jl*.

Fluid Status	:	Bulk
Particle-Particle Interaction	:	Square-Well ($\lambda^* = 1.5$)
Simulation Box	:	$20\sigma \times 20\sigma \times 20\sigma$
Initial Configuration	:	Random
# Relaxation Steps	:	$2 \times N \times 10^4$
# Equilibrium Steps	:	$2.5 \times N \times 10^5$
# Averages	:	25,000
$\langle U^*/N \rangle$	:	✓
$\langle p^* \rangle$	:	×
$\langle g(r^*) \rangle$	:	✓
$\langle \mu^*_{ex} \rangle$	:	✓
# Test Particle Insertions	:	5,000

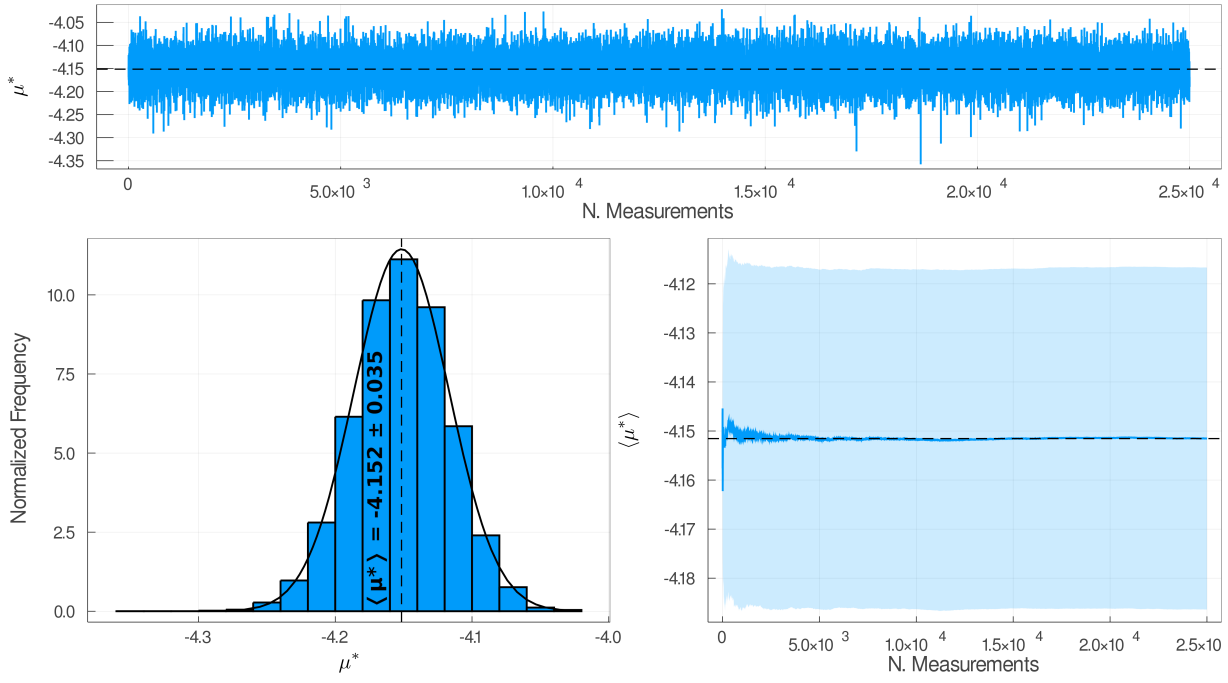

Figure 4.3: μ^* and $\langle \mu^* \rangle$ presented for an arbitrary system with $T^* = 1.5$ and $\rho^* = 0.1$, displaying the 2.5×10^4 measurements during the equilibrium steps. **(A)** Every μ^* calculated in each measurement with a prevailing behavior around $\langle \mu^* \rangle$. **(B)** Histogram of μ^* frequencies and its corresponding normal distribution as dictated by the Central Limit Theorem (2.2). **(C)**. Convergence of $\langle \mu^* \rangle$ with narrow oscillations around the final value.

With the code set and running, simulations of the twelve elected systems were executed with times ranging from 6 hours up to 20 hours, depending on the density of the system. The results are summarized in table 4.4 where T^* and ρ^* define the system and the rest of the columns are calculated. Note: Chemical potential is splitted into its ideal and excess contributions as mentioned in chapter 2.4.2.

Table 4.2: Runs in the *NVT* ensemble executed with *Canonical.jl*. Columns on the left define the system, while columns on the right are calculated along the simulation through ensemble averaging.

***NVT* Ensemble**					
$\boldsymbol{\rho^*}$	$\boldsymbol{T^*}$	$\boldsymbol{\mu^*_{id}}$	$\langle \boldsymbol{\mu^*_{Ex}} \rangle$	$\langle \boldsymbol{\mu^*} \rangle$	$\langle \boldsymbol{U^*/N} \rangle$
0.1	1.5	-3.454	-0.697 ± 0.038	-4.151 ± 0.038	-0.914 ± 0.098
	2.0	-4.605	-0.377 ± 0.034	-4.982 ± 0.034	-0.782 ± 0.082
	2.5	-5.756	-0.099 ± 0.036	-5.856 ± 0.036	-0.718 ± 0.077
	3.0	-6.908	0.162 ± 0.040	-6.746 ± 0.040	-0.681 ± 0.073
0.3	1.5	-1.806	-1.569 ± 0.109	-3.375 ± 0.109	-2.438 ± 0.073
	2.0	-2.408	-0.623 ± 0.097	-3.031 ± 0.097	-2.222 ± 0.061
	2.5	-3.01	0.291 ± 0.102	-2.719 ± 0.102	-2.121 ± 0.056
	3.0	-3.612	1.912 ± 0.114	-2.421 ± 0.114	-2.060 ± 0.053
0.6	1.5	-0.766	-0.886 ± 0.456	-1.652 ± 0.456	-4.533 ± 0.033
	2.0	-1.021	1.825 ± 0.533	0.803 ± 0.533	-4.424 ± 0.033
	2.5	-1.277	4.531 ± 0.640	3.254 ± 0.640	-4.359 ± 0.033
	3.0	-1.532	7.231 ± 0.755	5.699 ± 0.755	-4.316 ± 0.033

The ideal chemical potential contribution follows a direct dependence of T^* and $\ln(\rho^*)$ (from equation 2.28a), this is quickly appreciated on the third column of the previous table. Regarding the excess chemical contribution that is calculated by ensamble averages (from equation 2.28b), for a fixed density the calculated values follow a linear behavior. This same linear behavior is present after the combined chemcial potential contributions, therefore, a linear regression may allow to predict values not yet calculated:

Table 4.3: Linear regression for the calculated chemical potentials at a fixed density. The second column show the linear equation and the last one the ratio of variation.

Linear Regression For μ^*		
$\boldsymbol{\rho^*}$	$\mu^*_{Approx.}$	R^2
0.1	$-1.732T^* - 1.537$	0.9998
0.3	$0.635T^* - 4.315$	0.9989
0.6	$4.901T^* - 9.001$	1

Although only using four data points may make the model uncertain, all three scopes

display values of $R^2 \approx 1$, stating a low-to-non variance between the variables. It's worth to mention that only the low-density system has a negative slope, while the medium- and high-density systems have a positive one with increasing value.

Regarding the average energy per particle, fixing the density shows concave downwards curves as a function of T^*, with now a quadratic regression returning favorable values

Table 4.4: Quadratic regression for the calculated energy per particle at a fixed density. The second column show the quadratic equation and the last one the ratio of variation.

Quadratic Regression For U / N		
$\boldsymbol{\rho^*}$	$\mu^*_{Approx.}$	R^2
0.1	$-0.095T^{*2} + 0.580T^* - 1.568$	0.9973
0.3	$-0.151T^{*2} + 0.923T^* - 3.476$	0.9969
0.6	$-0.066T^{*2} + 0.440T^* - 5.044$	0.9991

At first glance, the calculated information is enough to proceed to the adsorption systems in confined pores, but a set of complementary simulations in the grand canonical ensemble were designed to find the optimal parameters of this ensemble. The decision criteria this time was a strict agreement with the previous results in the canonical ensemble.

The twelve new runs now in the the μVT ensemble were carried out in the designed *GrandCanonical.jl* code which is also obtainable from my GitHub repository (more details in Appendix C.4). Compared to its predecessor ensemble, this systems are said to be open in the sense that an exchange of particles with a reservoir is continuously present, leading to two important modifications to keep in mind along the simulation:

- Starting with an empty simulation box and allowing it to be filled, according to the *Cavity-Biased* algorithm denoted in 2.9, results in the most rational initial configuration.
- The amount of relaxation and equilibrium states were previously defined in the canonical ensemble based on the fixed number of particles. This is no longer possible, thus the amount steps are set to scale according to an *idealized* number of particles corresponding to a system of $\rho^*_{ideal} = 0.5$.

$$N_{ideal} = \lceil \rho_{ideal} \times V \rceil = \lceil 0.5 \times V \rceil \tag{4.2}$$

with the ceiling function guaranteeing that N_{ideal} results in an integer number.

Besides these important changes, the rest of them remain the same and are summarized

in table 4.5, followed up by a set of plots in figure 4.4 for the density convergence as a function of the simulation steps for an arbitrary system.

Table 4.5: Optimal parameters for the simulations implemented in the code *GrandCanonical.jl*.

Fluid Status	:	Bulk
Particle-Particle Interaction	:	Square-Well ($\lambda^* = 1.5$)
Simulation Box	:	$20\sigma \times 20\sigma \times 20\sigma$
Initial Configuration	:	Empty
# Relaxation Steps	:	$2 \times \lceil 0.5V \rceil \times 10^4$
# Equilibrium Steps	:	$2.5 \times \lceil 0.5V \rceil \times 10^5$
# Averages	:	25,000
$\langle U^*/N \rangle$	:	✓
$\langle p^* \rangle$	:	×
$\langle \rho^* \rangle$	:	✓
$\langle g(r^*) \rangle$	:	✓

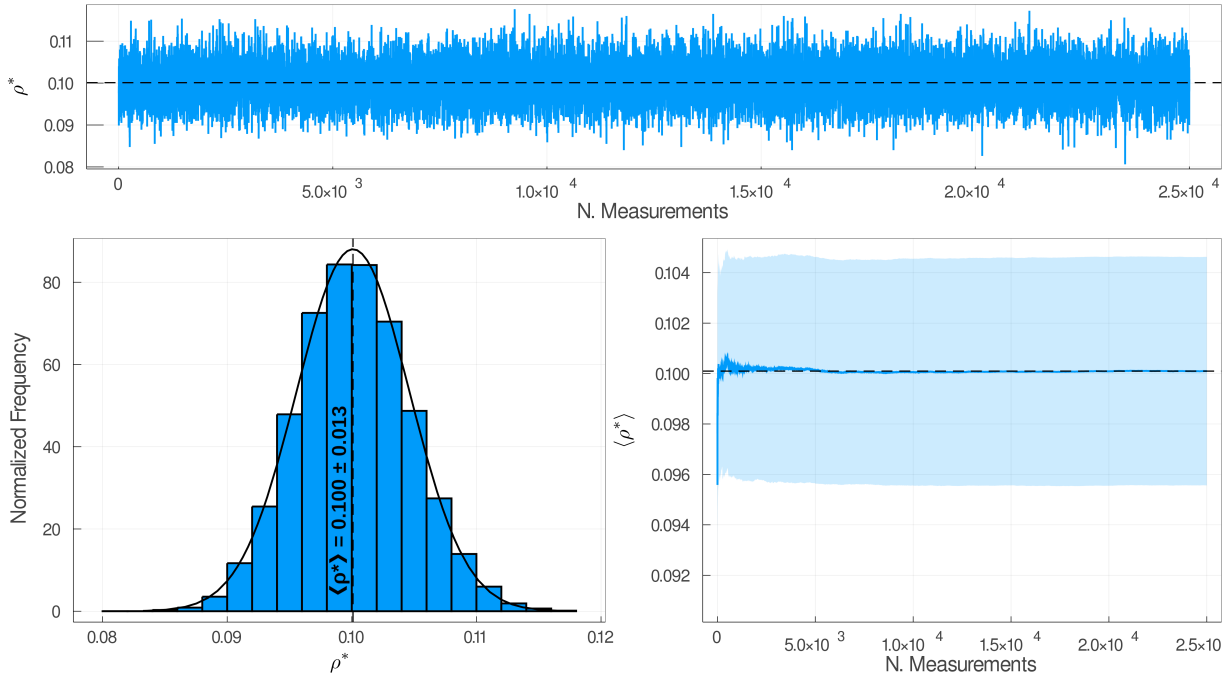

Figure 4.4: ρ^* and $\langle \rho^* \rangle$ presented for an arbitrary system with $T^* = 1.5$ and $\mu^* = -4.151$, displaying the 2.5×10^4 measurements during the equilibrium steps. **(A)** Every ρ^* calculated in each measurement with a prevailing behavior around $\langle \rho^* \rangle$. **(B)** Histogram of ρ^* frequencies and its corresponding normal distribution as dictated by the Central Limit Theorem (2.2). **(C)**. Convergence of $\langle \rho^* \rangle$ with narrow oscillations around the final value.

Feeding the previous chemical potentials calculated to the μVT ensemble, calculates densities (displayed in table 4.6) that discern on the order of 10^{-2}. For an easier visualization, the calculated values with their corresponding error bars are plotted in figure 4.5 with vertical bars provided by the NVT ensemble and horizontal ones provided by the μVT ensemble.

Table 4.6: Runs in the μVT ensemble executed with *GrandCanonical.jl*. Columns on the left define the system, while columns on the right are calculated along the simulation through ensemble averaging.

μVT Ensemble			
T^*	μ^*	$\langle \rho^* \rangle$	$\langle U^*/N \rangle$
1.5	-4.151	0.100 ± 0.013	-0.914 ± 0.148
	-3.375	0.300 ± 0.023	-2.439 ± 0.163
	-1.652	0.608 ± 0.008	-4.596 ± 0.064
2.0	-4.982	0.100 ± 0.023	-0.780 ± 0.115
	-3.031	0.300 ± 0.015	-2.222 ± 0.116
	0.803	0.606 ± 0.008	-4.473 ± 0.062
2.5	-5.856	0.100 ± 0.010	-0.718 ± 0.104
	-2.719	0.300 ± 0.013	-2.125 ± 0.104
	3.254	0.605 ± 0.007	-4.401 ± 0.061
3.0	-6.746	0.100 ± 0.009	-0.680 ± 0.099
	-2.421	0.300 ± 0.013	-2.062 ± 0.098
	5.699	0.604 ± 0.007	-4.347 ± 0.060

The calculated values from both ensambles seem to perfectly concide, at least for the low- and medium-density systems. Meanwhile, the high-density one displays calculated densities a little higher than they should be, a common discrepancy for highly populated systems, but the overlapping of the error bars ensures the agreement of the results.

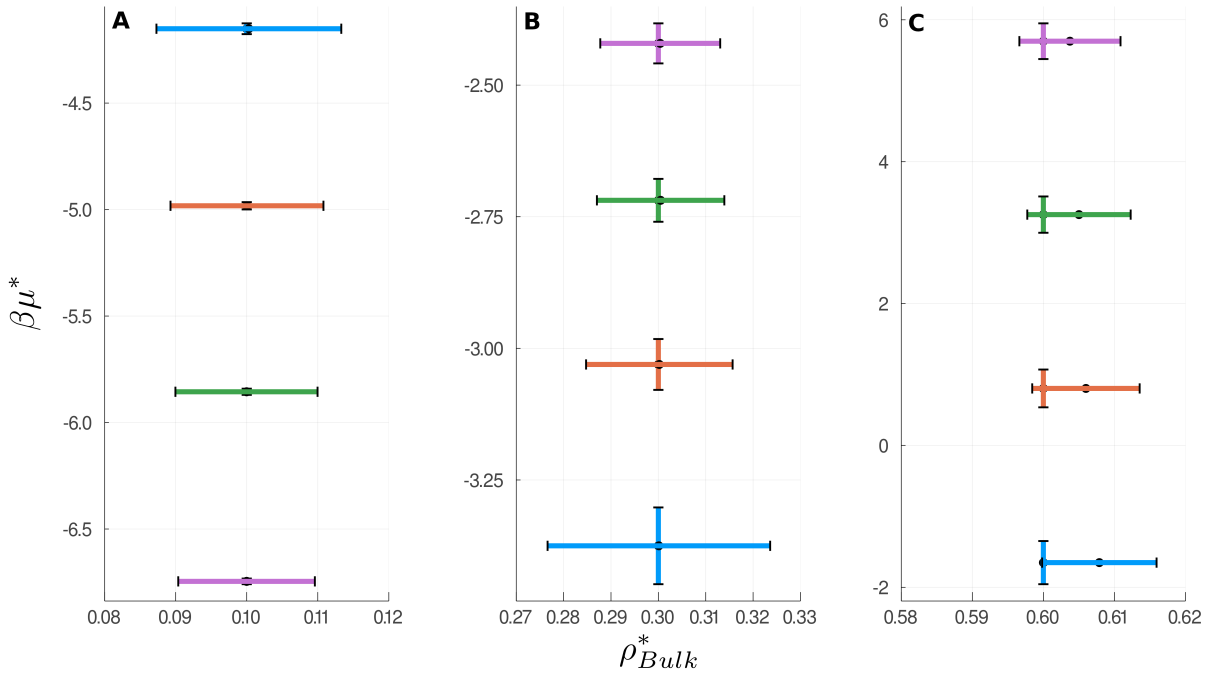

Figure 4.5: Vertical error bars from the canonical ensemble's table 4.4 and horizont bars from the grand canonical ensemble's table 4.6 for the: **(A)** Low-, **(B)** Medium- and **(C)** High-density systems.
Color scheme represents $T^* = 1.5$, $T^* = 2.0$, $T^* = 2.5$ and $T^* = 3.0$.

Radial distribution functions calculated in both ensembles are compared side to side in figure 4.6, where the ones from the canonical ensemble are represented by solid lines and the ones from the grand canonical ensemble by overlapping dashed lines. Each of the panels display different densities: **(A)** Low-, **(B)** Medium- and **(C)** High-density systems with four different temperatures dictated by the color scheme $T^* = 1.5$, $T^* = 2.0$, $T^* = 2.5$ and $T^* = 3.0$.

The main highlights of each panel are as follow:

- **Low-density**: Density distribution denotes two flat zones (One from σ to 1.5σ with higher density values and another one from 1.5σ to 3σ with normalized values near to unity), denoting an equal likelihood of molecules being separated between σ and 1.5σ units apart. Lower temperatures increase the distribution profile around the first flat zone, denoting a higher tendency for molecules to cluster.
- **Medium-density**: Structure is barely perceptible with a barely larger value at $r^* = \sigma$ that slowly descends until 1.5σ units of separation. Distances further away exhibit small-scale oscillations .
- **High-density**: Molecular structure is well-defined, with a leading peak found at $r^* = \sigma$, followed by a drastically smaller one near $r^* \approx 1.5\sigma$ and prominent oscillations around unity for further separation values. Unlike lower-density systems where temperature scales the size of the whole distribution function, for high-density systems higher temperatures attempt to flatten the curve comprehending the two main peaks, lowering the height of the first one while increasing the second one.

Each panel show similar molecular structures with temperature playing a negligible role, inducing minimal variations on the height of the first two peaks or the flat section, just as mentioned previously. The similar structure results in uninteresting systems for the confinement phase, culminating once again in similar adsorptions.

Therefore, it's been opted to drop out half the systems to maintain only the limiting cases ($T^* = 1.5$ and 3) which provided different structural properties to a greater extend. This decision should allow a deeper exploration of a reduced number of systems, but with the consideration of larger separation span of the pore's walls with a diverse set of patterns.

To this end, wholly SW ($\lambda = 1.5$) and HS ($\lambda = 1, \epsilon = 0$) walls were designed as control variables (since their adsorptions indicate the limiting adsorption cases), followed by five different pattern arrangements (also known as lithographic decorations) conformed by the two natures of interaction previously mentioned. Given that the object of study is the adsorption

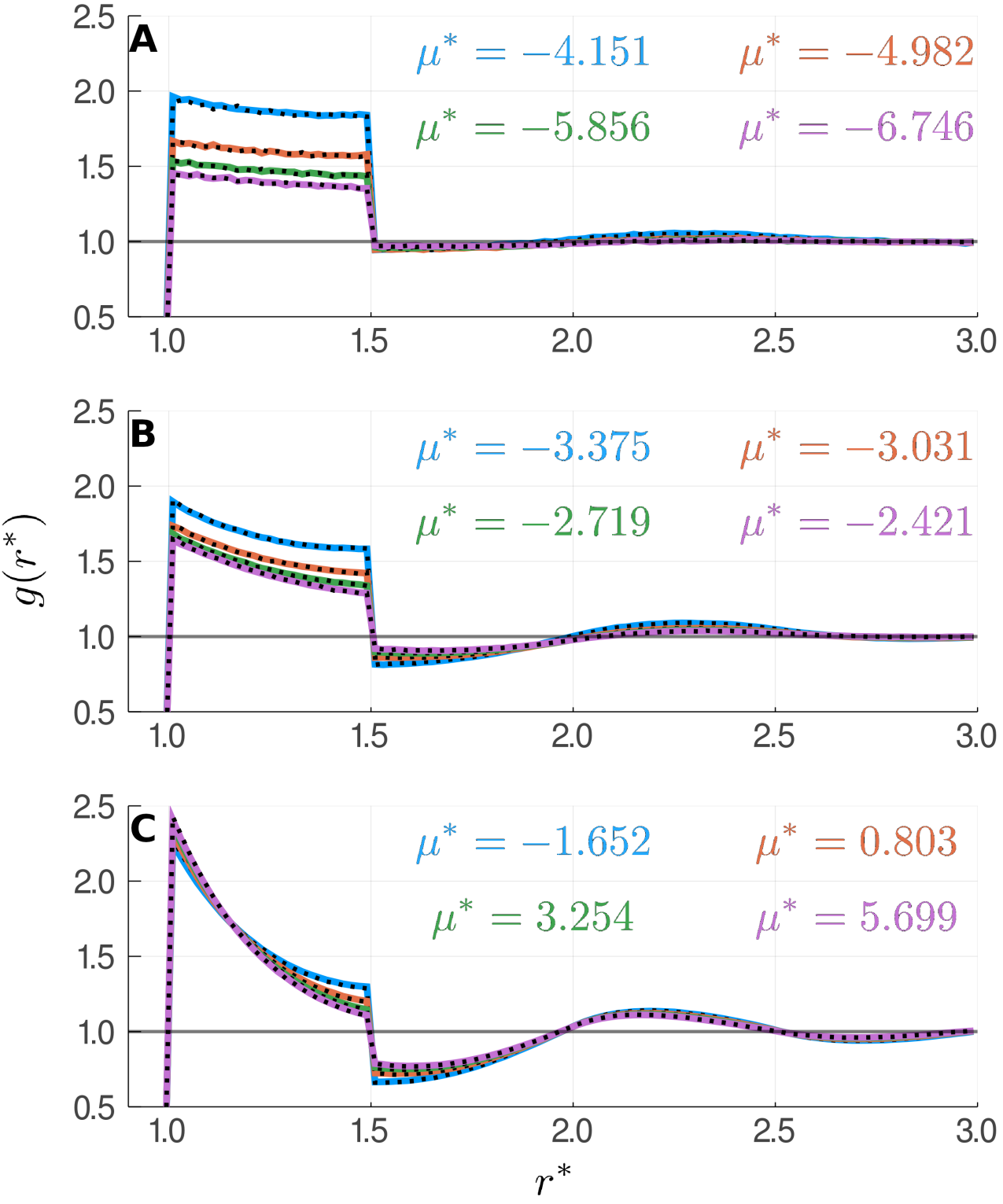

Figure 4.6: Radial distribution functions calculated in both the canonical (solid) and grand canonical (dashed) ensembles for the: **(A)** Low-, **(B)** Medium- and **(C)** High-density systems.
Color scheme represents $T^* = 1.5$, $T^* = 2.0$, $T^* = 2.5$ and $T^* = 3.0$.

of the pores due to the adsorbing pattern in the wall, the ratio between interacting sections is fixed to fifty percent of the area each. This patterns, illustrated in figure 4.7, sum up to a total of seven different wall designs with separations ranging values of $L_z \in [3, 4, 5, 6, 7, 8, 9, 10, 11]$ for the remaining six sytems ($T^* \in [1.5, 3]$ and $\rho_{Bulk} \in [0.1, 0.3, 0.6]$) adds to a total of three hundred seventy-eight different systems to be simulated with the third and final desgined *ConfinedGrandCanonical.jl* code (more details may be found in appendix C.6). This code imports previously defined parameters from table 4.5, put to test with results reported by D. R. Bérard [44] and reinforcing them into those presented in table 4.7.

Main changes to its same ensemble predecessor code are:

- Molecular interfaces placed to confine the system. This adds a fluid-wall interaction which is unique for each of the designed patterns.
- No longer cubic simulation box, with the variable separation of the walls defined by L_z.
- Maximum displacement of molecules now controlled by two variables δ_{xy} and δ_z for their corresponding axis.
- Calculation of the distribution profiles, instead of its radial analogue.
- Generation and execution of PovRay codes for visualization purposes from different points of view.

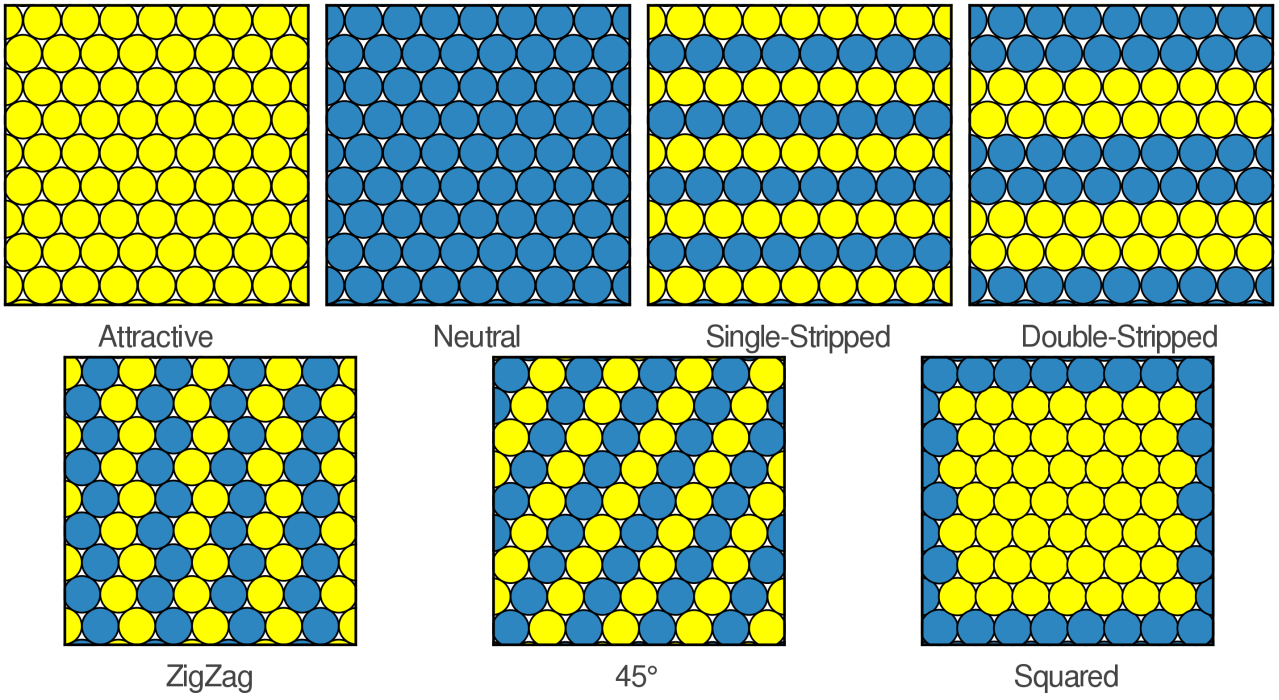

Figure 4.7: Lithographic pattern designs for the confining walls consisting of hexagonally arranged molecules with SW (Attractive, yellow) and HS (Neutral, blue) interactions. Nametags arbitrarily defined.

Table 4.7: Optimal parameters for the simulations implemented in the code *ConfinedGrandCanonical.jl*.

Fluid Status	:	Confined
Particle-Particle Interaction	:	Square-Well ($\lambda^* = 1.5$)
Wall-Particle Interaction	:	Square-Well ($\lambda^* = 1.5$)
Wall-Wall Interaction	:	Fixed Hard-Spheres
Simulation Box	:	$20\sigma \times 20\sigma \times L_z$
Starting Configuration	:	Empty
# Relaxation Steps	:	$2 \times \lceil 5V \rceil \times 10^3$
# Equilibrium Steps	:	$25 \times \lceil 5V \rceil \times 10^3$
# Averages	:	25,000
$\langle U^*/N \rangle$	:	✓
$\langle p_N^* \rangle$	:	×
$\langle p_T^* \rangle$	:	×
$\langle \rho_{Pore}^* \rangle$	:	✓
$\langle g(z^*) \rangle$	:	✓

Chapter 5

Results

The vast set of stipulated systems required high-end computational resources, attained from the *Laboratorio de Supercómputo y Visualización en Paralelo's (LSVP)* cluster *YOLTLA* by the *UAM-Iztapalapa*. This high level performance supercomputer comprised of 6392 Intel Xeon logical processing cores enabled approximately 20370 CPU-hours @ 2.6GHz for this investigation.

The highlights of the generated results are segmented in six sections (for each $T^* - \rho_{Bulk}$ combination), each consisting of four main segments:

1. A sixty-three entries table for a certain value of T^* and ρ_{Bulk}. Segmentation corresponds to the nine different pore separations ($L_z \in [3..11]$) with each pattern design having its average total energy per particle (both wall and fluid interactions) and the adsorption density.

2. A two panel plot displaying the results from the previous table (upper for average adsorbed density and lower for average total energy per particle) as a visual assistance tool for tendency tracking. Values are normalized with respect to its bulk system for comparison purposes.

3. First layer of adsorption (1.5σ units away from the wall) illustrating preferential adsorption spots for each pattern. Each illustration represent an arbitrary frame out of the 25,000 saved configurations.

4. Distribution profiles as described in section 3.3 for each separation, but only for the most contrasting pattern designs.

Note: Hereinafter, a density differentiation is implemented as the adsorbed density in the pore (ρ_{Pore}) is inherited from the its bulk system (ρ_{Bulk}).

$$T^* = 1.5 \quad \rho^*_{Bulk} = 0.1 \quad \mu^* = -4.151$$

Low-density and low-temperature system with adsorption values ranging from 0.026 to 0.332. The 45°, Single-Stripped and ZigZag design share similar adsorption densities $\langle \rho_{Pore} \rangle \approx 1$ (as its bulk) regardless the separation of the walls. Meanwhile, the Double-Stripped and Squared designs are slightly more adsorbant, in that consecutive order.

A wider-spread set of average energy values is visible, with the 45° and Single-Stripped desings once again sharing similar values and the ZigZag, Double-Stripped and Squared laying into more negative values, in that descending order.

Table 5.1: Sixty-three entries corresponding to the $T^* = 1.5, \rho^*_{Bulk} = 0.1$ and $\mu^* = -4.151$ system, segmented according the walls' separation and pattern design.

μVT ensemble for a confined system with multiple pattern designs.

L^*_z	Decoration	$\langle \rho^*_{Pore} \rangle$	$\langle U^*/N \rangle$	L^*_z	Decoration	$\langle \rho^*_{Pore} \rangle$	$\langle U^*/N \rangle$
	Attractive	0.332 ± 0.080	-7.129 ± 0.084		Attractive	0.179 ± 0.008	-3.724 ± 0.103
	Neutral	0.026 ± 0.005	-0.279 ± 0.104		Neutral	0.071 ± 0.006	-0.781 ± 0.087
	Squared	0.128 ± 0.007	-5.693 ± 0.260		Squared	0.107 ± 0.007	-2.316 ± 0.126
3.0	45°	0.095 ± 0.010	-2.843 ± 0.144	8.0	45°	0.099 ± 0.007	-1.563 ± 0.088
	Single-Stripped	0.094 ± 0.010	-2.842 ± 0.145		Single-Stripped	0.099 ± 0.007	-1.562 ± 0.088
	Double-Stripped	0.115 ± 0.010	-3.755 ± 0.157		Double-Stripped	0.106 ± 0.007	-1.902 ± 0.094
	ZigZag	0.096 ± 0.010	-2.904 ± 0.145		ZigZag	0.100 ± 0.007	-1.596 ± 0.089
	Attractive	0.275 ± 0.011	-5.363 ± 0.089		Attractive	0.170 ± 0.007	-3.539 ± 0.101
	Neutral	0.026 ± 0.005	-0.507 ± 0.109		Neutral	0.074 ± 0.006	-0.802 ± 0.083
	Squared	0.119 ± 0.008	-3.881 ± 0.217		Squared	0.106 ± 0.006	-2.168 ± 0.116
4.0	45°	0.098 ± 0.009	-2.249 ± 0.122	9.0	45°	0.099 ± 0.006	-1.492 ± 0.083
	Single-Stripped	0.098 ± 0.009	-2.249 ± 0.122		Single-Stripped	0.099 ± 0.006	-1.491 ± 0.083
	Double-Stripped	0.111 ± 0.009	-2.838 ± 0.127		Double-Stripped	0.105 ± 0.007	-1.799 ± 0.087
	ZigZag	0.099 ± 0.009	-2.307 ± 0.122		ZigZag	0.100 ± 0.006	-1.521 ± 0.084
	Attractive	0.233 ± 0.011	-4.594 ± 0.092		Attractive	0.163 ± 0.007	-3.379 ± 0.100
	Neutral	0.053 ± 0.006	-0.632 ± 0.105		Neutral	0.076 ± 0.005	-0.819 ± 0.078
	Squared	0.113 ± 0.008	-3.141 ± 0.176		Squared	0.106 ± 0.006	-2.050 ± 0.108
5.0	45°	0.099 ± 0.008	-1.963 ± 0.110	10.0	45°	0.099 ± 0.006	-1.436 ± 0.078
	Single-Stripped	0.099 ± 0.008	-1.963 ± 0.110		Single-Stripped	0.099 ± 0.006	-1.434 ± 0.078
	Double-Stripped	0.110 ± 0.009	-2.454 ± 0.115		Double-Stripped	0.105 ± 0.006	-1.715 ± 0.083
	ZigZag	0.100 ± 0.008	-2.010 ± 0.110		ZigZag	0.100 ± 0.006	-1.463 ± 0.080
	Attractive	0.207 ± 0.009	-4.209 ± 0.098		Attractive	0.157 ± 0.006	-3.236 ± 0.098
	Neutral	0.061 ± 0.006	-0.706 ± 0.099		Neutral	0.079 ± 0.005	-0.832 ± 0.074
	Squared	0.110 ± 0.007	-2.753 ± 0.154		Squared	0.105 ± 0.006	-1.953 ± 0.101
6.0	45°	0.099 ± 0.008	-1.783 ± 0.101	11.0	45°	0.099 ± 0.006	-1.388 ± 0.074
	Single-Stripped	0.099 ± 0.008	-1.782 ± 0.101		Single-Stripped	0.099 ± 0.006	-1.388 ± 0.075
	Double-Stripped	0.108 ± 0.008	-2.208 ± 0.106		Double-Stripped	0.104 ± 0.006	-1.646 ± 0.079
	ZigZag	0.100 ± 0.008	-1.822 ± 0.101		ZigZag	0.100 ± 0.006	-1.413 ± 0.075
	Attractive	0.191 ± 0.008	-3.938 ± 0.102				
	Neutral	0.066 ± 0.006	-0.752 ± 0.094				
	Squared	0.108 ± 0.007	-2.501 ± 0.139				
7.0	45°	0.099 ± 0.007	-1.657 ± 0.093				
	Single-Stripped	0.099 ± 0.007	-1.655 ± 0.094				
	Double-Stripped	0.107 ± 0.007	-2.034 ± 0.099				
	ZigZag	0.100 ± 0.007	-1.692 ± 0.094				

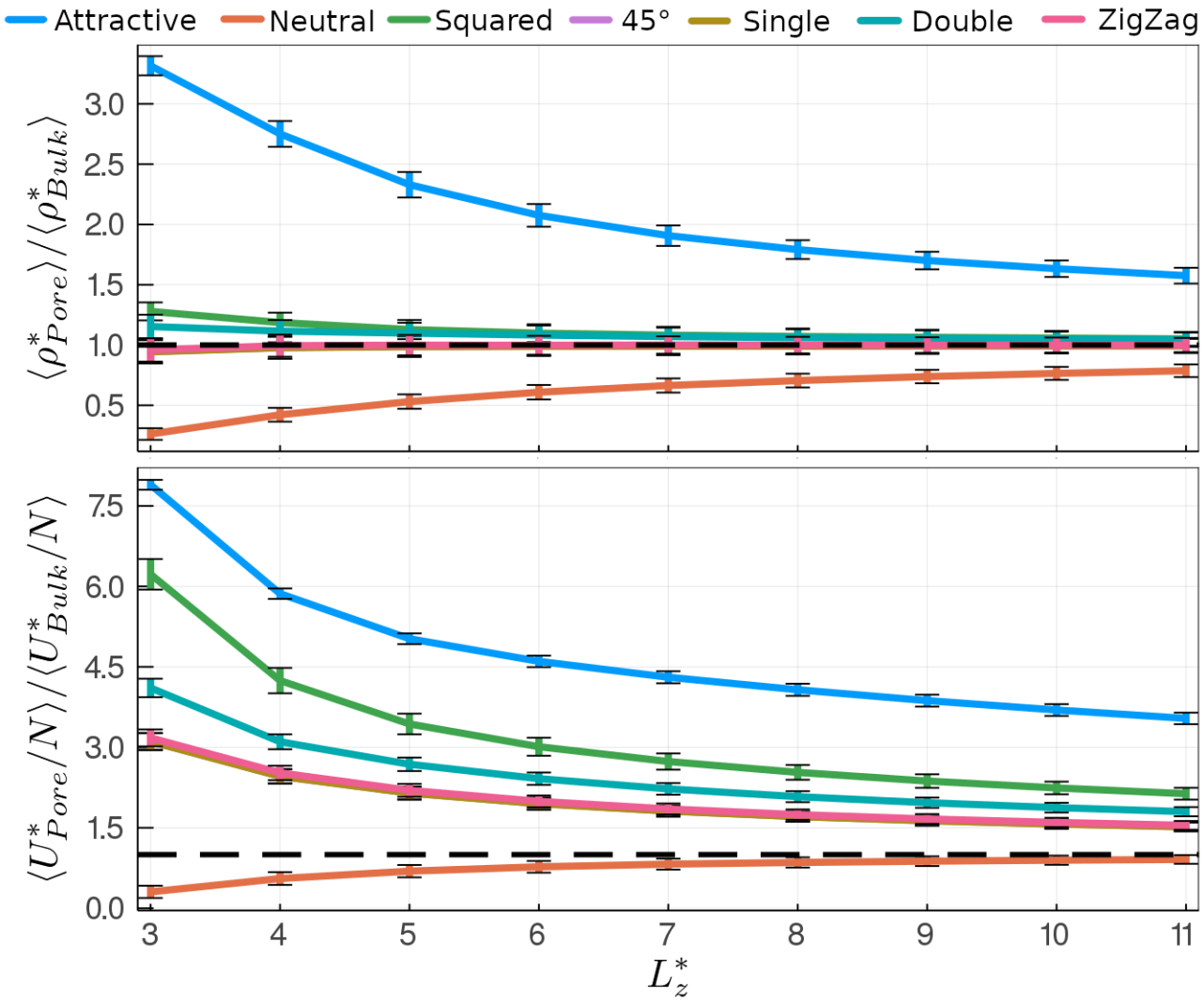

Figure 5.1: Visual summary of table 5.1 for the $T^* = 1.5, \rho^*_{Bulk} = 0.1, \mu^* = -4.151$ system. Upper panel displays average adsorption density normalized with its bulk density while lower panel displays average total energy per particle normalized with its bulk analogue.

$\langle \boldsymbol{\rho^*_{Pore}} \rangle / \langle \boldsymbol{\rho^*_{Bulk}} \rangle$: Minor distinctions are noticeable with the Squared and Double-Stripped patterns slightly surpassing the bulk density for small separations, while the rest stick really close to unity among all separations. The convergence to the bulk density is ubiquitous for all decorations as the separation increases, with their error bars overlapping each curve.

$\langle \boldsymbol{U^*_{Pore}/N} \rangle / \langle \boldsymbol{U^*_{Bulk}/N} \rangle$: Patterns obey the same order as for the adsorption density, all of them with higher energy values than the bulk. No difference is appreciable from the 45°, Single-Stripped and ZigZag patterns for any specific separation. Convergence of the energy as the separation increases to a single value is not as evident as for the adsorption, with values laying as twice as much as the bulk.

Fluid's molecules are primarily adsorbed near the SW (attractive) sections of the confining wall (displayed in yellow on image 5.5), a prominent behavior for contiguous pattern designs, like the Squared and Double-Stripped ones.

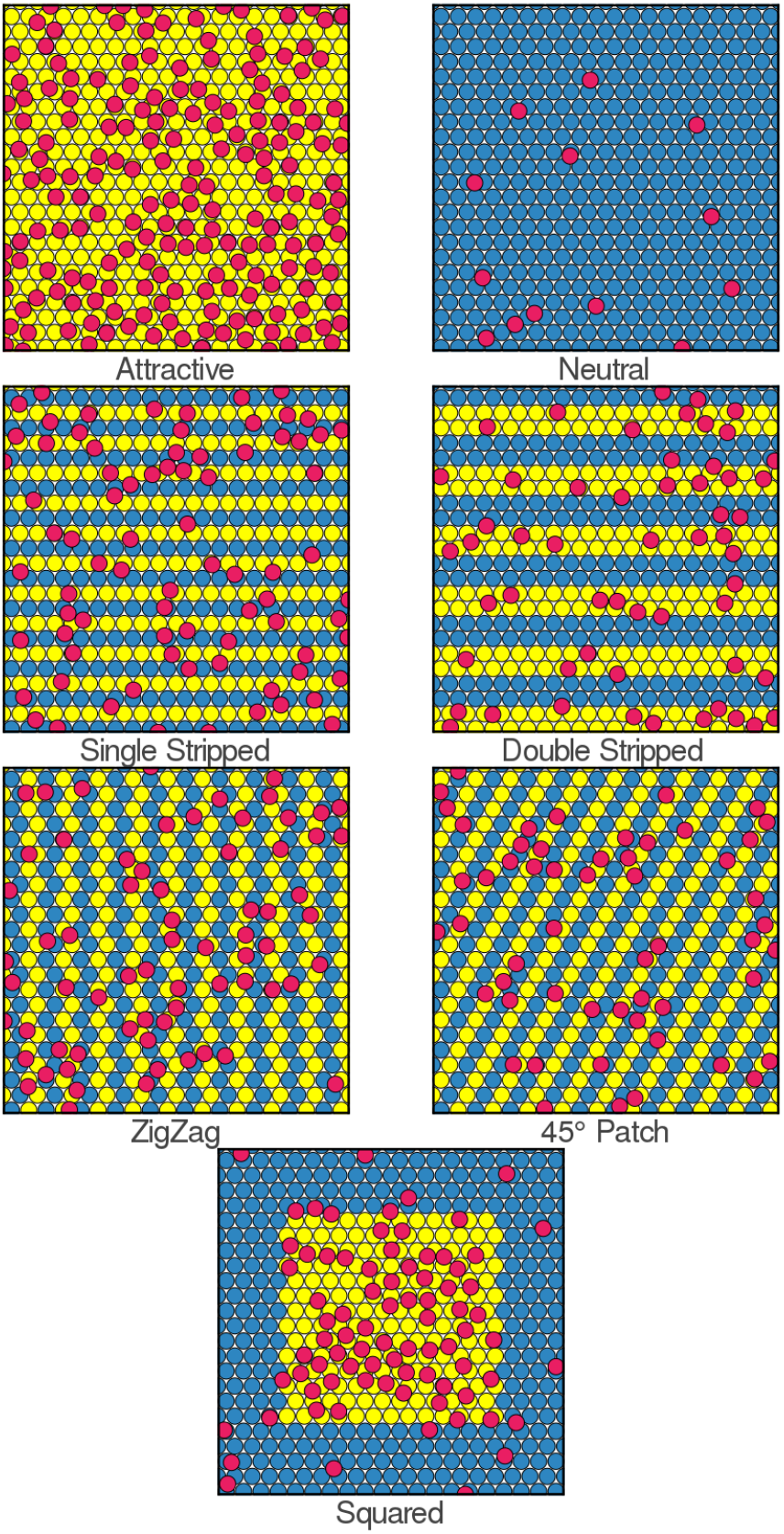

Figure 5.2: First adsorption layer (molecules 1.5σ units apart from the wall) of the designed lithographic patterns for the $T^* = 1.5, \rho^*_{Bulk} = 0.1, \mu^* = -4.151$ system. Color scheme: **Yellow** for SW (attractive), **Blue** for HS (neutral) and **Red** for fluid's molecules.

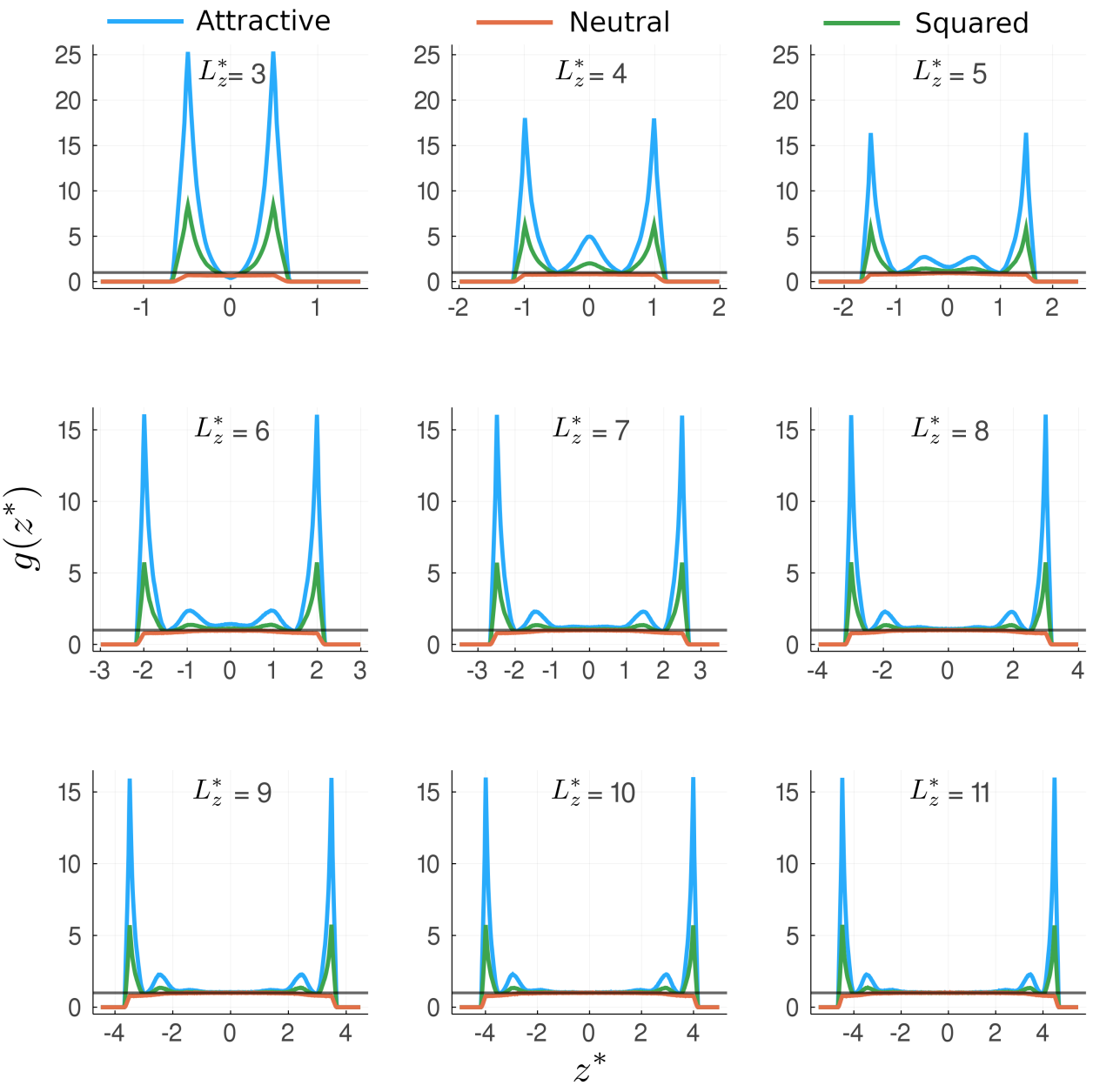

Figure 5.3: Distribution profiles normalized with the bulk density for the $T^* = 1.5, \rho^*_{Bulk} = 0.1, \mu^* = -4.151$ system. Pore separations range from $L_z = 3\sigma$ to $L_z = 11\sigma$, $L_z \in \mathbb{Z}$. Color scheme represents: **Blue** for attractive (SW), **Orange** for neutral (HS) and **Green** for squared slit-like walls' designs.

The overall averaged distribution of molecules in the pore along the z-axis has a drastically larger distribution near the walls for those patterns with attractive interactions, while the wholly HS one has no preferential spots.

Neutral walls display patterns near unity (representing bulk-like density), therefore its behavior is just like the bulk. This same behavior is onlly visible for the central sections for the rest of pattern designs with separations beyond 7σ; indicating that molecules 2.5σ no longer feel the pressence of the wall.

$$T^* = 1.5 \quad \rho^*_{Bulk} = 0.3 \quad \mu^* = -3.375$$

Medium-density and low-temperature system with adsorption values ranging from 0.046 to 0.384. Once again the 45°, Single-Stripped and ZigZag pattern designs have similar adsorption values across the calculated separations. None of the calculated system reaches values near the bulk density, regardless the distance between walls.

The spread of calculated energies is narrower, with 45°, Single-Stripped and ZigZag patterns still displaying similar values.

Table 5.2: Sixty-three entries corresponding to the $T^* = 1.5, \rho^*_{Bulk} = 0.3$ and $\mu^* = -3.375$ system, segmented according the walls' separation and pattern design.

μVT ensemble for a confined system with multiple pattern designs.							
L^*_z	Decoration	$\langle \rho^*_{Pore} \rangle$	$\langle U^*/N \rangle$	L^*_z	Decoration	$\langle \rho^*_{Pore} \rangle$	$\langle U^*/N \rangle$
	Attractive	0.384 ± 0.006	-7.702 ± 0.077		Attractive	0.346 ± 0.009	-4.308 ± 0.052
	Neutral	0.046 ± 0.007	-0.489 ± 0.108		Neutral	0.180 ± 0.010	-1.879 ± 0.103
	Squared	0.168 ± 0.007	-5.807 ± 0.228		Squared	0.242 ± 0.010	-3.041 ± 0.075
3.0	45°	0.176 ± 0.011	-3.617 ± 0.120	8.0	45°	0.254 ± 0.011	-2.748 ± 0.083
	Single-Stripped	0.176 ± 0.011	-3.614 ± 0.121		Single-Stripped	0.254 ± 0.011	-2.747 ± 0.082
	Double-Stripped	0.192 ± 0.010	-4.339 ± 0.119		Double-Stripped	0.260 ± 0.011	-2.925 ± 0.077
	ZigZag	0.177 ± 0.011	-3.662 ± 0.119		ZigZag	0.256 ± 0.011	-2.775 ± 0.081
	Attractive	0.377 ± 0.007	-6.106 ± 0.064		Attractive	0.343 ± 0.009	-4.129 ± 0.051
	Neutral	0.084 ± 0.008	-0.972 ± 0.120		Neutral	0.193 ± 0.010	-1.968 ± 0.098
	Squared	0.191 ± 0.009	-4.260 ± 0.167		Squared	0.248 ± 0.010	-2.958 ± 0.071
4.0	45°	0.205 ± 0.012	-3.152 ± 0.105	9.0	45°	0.259 ± 0.010	-2.711 ± 0.078
	Single-Stripped	0.205 ± 0.012	-3.151 ± 0.105		Single-Stripped	0.259 ± 0.011	-2.708 ± 0.080
	Double-Stripped	0.215 ± 0.011	-3.556 ± 0.099		Double-Stripped	0.264 ± 0.010	-2.865 ± 0.075
	ZigZag	0.207 ± 0.012	-3.203 ± 0.106		ZigZag	0.260 ± 0.010	-2.730 ± 0.078
	Attractive	0.366 ± 0.008	-5.308 ± 0.060		Attractive	0.338 ± 0.009	-3.976 ± 0.050
	Neutral	0.116 ± 0.009	-1.326 ± 0.121		Neutral	0.204 ± 0.010	-2.039 ± 0.092
	Squared	0.209 ± 0.009	-3.629 ± 0.119		Squared	0.253 ± 0.009	-2.894 ± 0.068
5.0	45°	0.225 ± 0.012	-2.970 ± 0.098	10.0	45°	0.264 ± 0.010	-2.682 ± 0.075
	Single-Stripped	0.225 ± 0.012	-2.970 ± 0.098		Single-Stripped	0.263 ± 0.010	-2.677 ± 0.074
	Double-Stripped	0.233 ± 0.011	-3.270 ± 0.091		Double-Stripped	0.268 ± 0.010	-2.819 ± 0.070
	ZigZag	0.227 ± 0.012	-3.014 ± 0.097		ZigZag	0.264 ± 0.010	-2.697 ± 0.074
	Attractive	0.359 ± 0.009	-4.854 ± 0.057		Attractive	0.335 ± 0.009	-3.853 ± 0.048
	Neutral	0.142 ± 0.010	-1.577 ± 0.117		Neutral	0.212 ± 0.009	-2.091 ± 0.085
	Squared	0.223 ± 0.010	-3.329 ± 0.095		Squared	0.258 ± 0.009	-2.849 ± 0.065
6.0	45°	0.238 ± 0.011	-2.870 ± 0.091	11.0	45°	0.267 ± 0.010	-2.658 ± 0.072
	Single-Stripped	0.238 ± 0.011	-2.868 ± 0.092		Single-Stripped	0.266 ± 0.010	-2.653 ± 0.072
	Double-Stripped	0.246 ± 0.011	-3.114 ± 0.084		Double-Stripped	0.271 ± 0.010	-2.780 ± 0.069
	ZigZag	0.240 ± 0.012	-2.902 ± 0.091		ZigZag	0.267 ± 0.010	-2.671 ± 0.071
	Attractive	0.353 ± 0.009	-4.546 ± 0.055				
	Neutral	0.163 ± 0.010	-1.753 ± 0.111				
	Squared	0.233 ± 0.010	-3.151 ± 0.082				
7.0	45°	0.248 ± 0.011	-2.801 ± 0.088				
	Single-Stripped	0.247 ± 0.011	-2.798 ± 0.085				
	Double-Stripped	0.253 ± 0.011	-3.003 ± 0.082				
	ZigZag	0.249 ± 0.011	-2.827 ± 0.084				

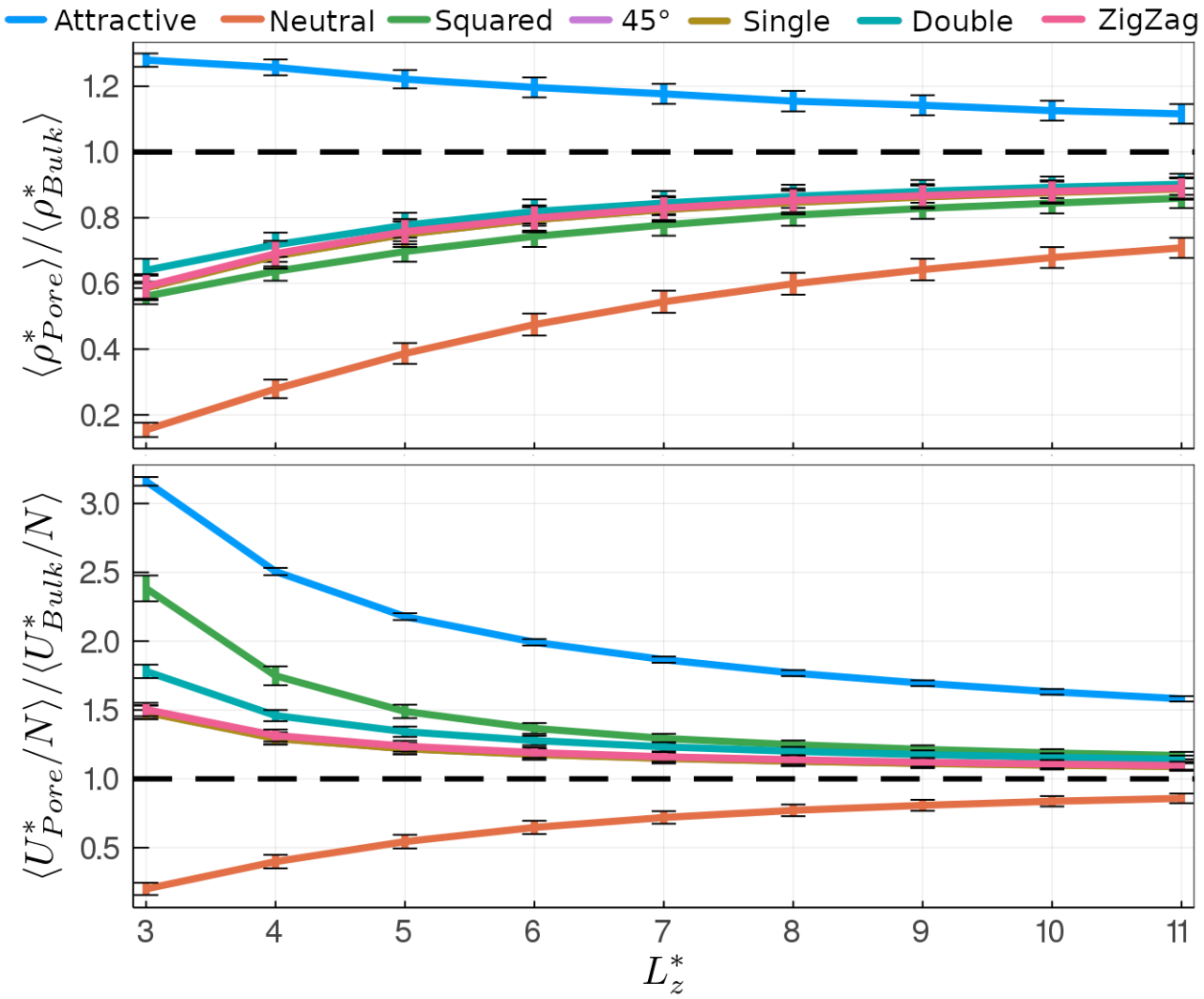

Figure 5.4: Visual summary of table 5.2 for the $T^* = 1.5, \rho^*_{Bulk} = 0.3, \mu^* = -3.375$ system. Upper panel displays average adsorption density normalized with its bulk density while lower panel displays average total energy per particle normalized with its bulk analogue.

$\langle \boldsymbol{\rho^*_{Pore}} \rangle / \langle \boldsymbol{\rho^*_{Bulk}} \rangle$: With less prolific adsorption values (as they go under the bulk density), the Double-Stripped takes the lead, followed by the 45°, Single-Stripped and ZigZag patterns that have been sharing values so far and lastly, the squared one (that used to be the most adsorbant in the previous system). The range of values is narrower, with all of them converging to similar adsorption densities.

$\langle \boldsymbol{U^*_{Pore}/N} \rangle / \langle \boldsymbol{U^*_{Bulk}/N} \rangle$: Although a similar order of appearence is observed, the squared pattern results in the most energetic one, with a wide spread set of values for $L^*_z \leq 6$, but rapidly converging into a unique line.

Although the adsorption of molecules is mainly on attractive areas, a remarkable rate of them are also found in neutral sections; driving into a more homogeneous adsorption despite the pattern design.

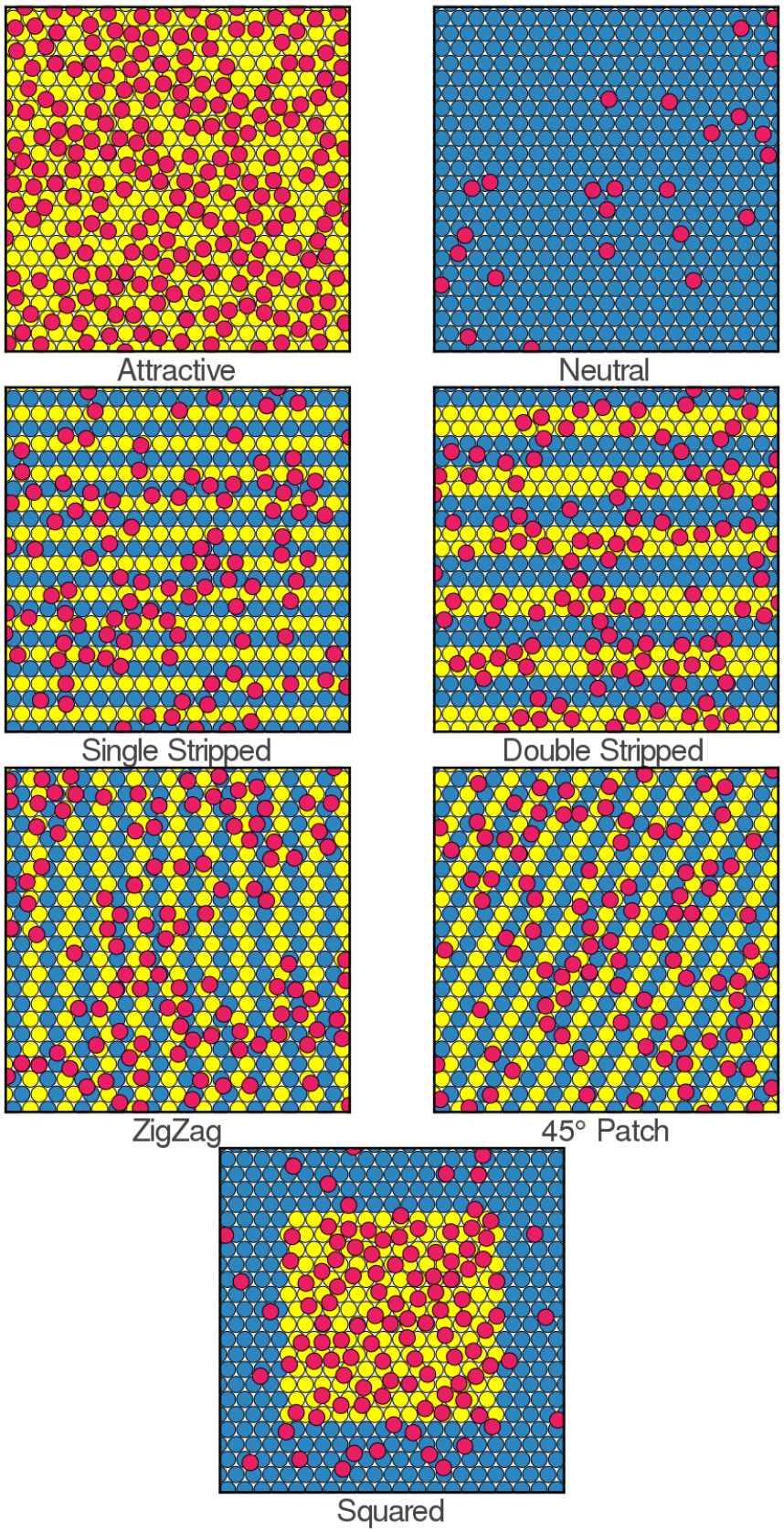

Figure 5.5: First adsorption layer (molecules 1.5σ units apart from the wall) of the designed lithographic patterns for the $T^* = 1.5, \rho^*_{Bulk} = 0.3, \mu^* = -3.375$ system. Color scheme: **Yellow** for SW (attractive), **Blue** for HS (neutral) and **Red** for fluid's molecules.

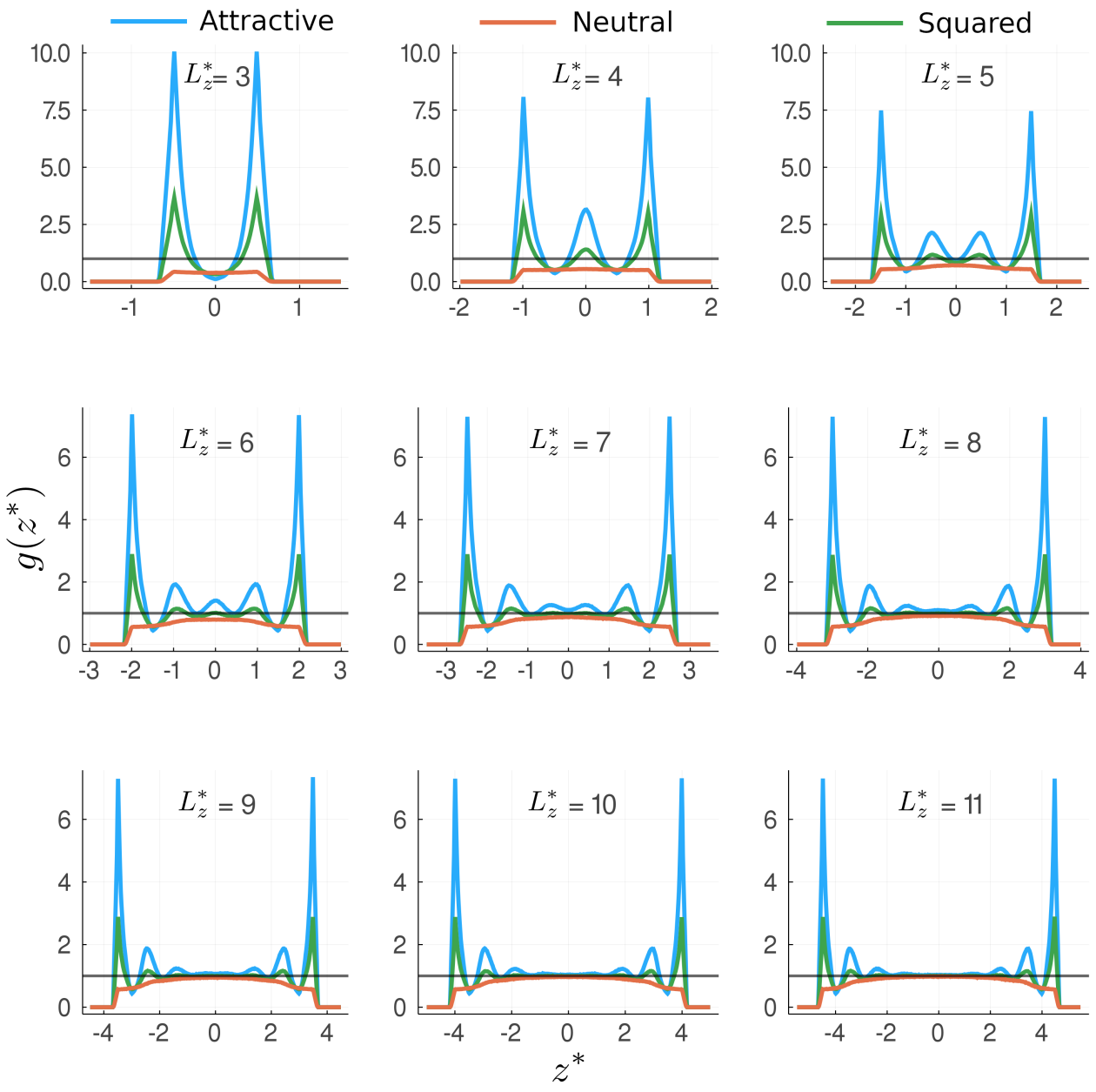

Figure 5.6: Distribution profiles normalized with the bulk density for the $T^* = 1.5, \rho^*_{Bulk} = 0.3, \mu^* = -3.375$ system. Pore separations range from $L_z = 3\sigma$ to $L_z = 11\sigma$, $L_z \in \mathbb{Z}$. Color scheme represents: **Blue** for attractive (SW), **Orange** for neutral (HS) and **Green** for squared slit-like walls' designs.

The adsorbance of wholly neutral walls is way lower than the bulk fluid for separations smaller than 5σ, with a slow fitting into unity as separation increases. For the attractive and squared patterns, the number of adsorption oscillations near the center of the pore increased, with only molecules 3.5σ units away from the wall diminishing their interaction.

$$T^* = 1.5 \quad \rho^*_{Bulk} = 0.6 \quad \mu^* = -1.652$$

High-density and low-temperature system with adsorption values ranging from 0.160 to 0.447. Adsorption densities are identical for four out of the five patterns, with the squared one being only one laying on lower values. Achievement of adsorption values similar to the bulk fluid was not posible, not even for the wholly attractive control wall.

Similar energetic valeus are displayed across the each separation segment of the table, quickly converging after a separation of 7σ.

Table 5.3: Sixty-three entries corresponding to the $T^* = 1.5, \rho^*_{Bulk} = 0.6$ and $\mu^* = -1.652$ system, segmented according the walls' separation and pattern design.

μVT ensemble for a confined system with multiple pattern designs.							
L^*_z	Decoration	$\langle \rho^*_{Pore} \rangle$	$\langle U^*/N \rangle$	L^*_z	Decoration	$\langle \rho^*_{Pore} \rangle$	$\langle U^*/N \rangle$
	Attractive	0.447 ± 0.006	-8.295 ± 0.071		Attractive	0.533 ± 0.004	-5.525 ± 0.035
	Neutral	0.160 ± 0.010	-1.533 ± 0.100		Neutral	0.451 ± 0.005	-4.002 ± 0.040
	Squared	0.278 ± 0.008	-5.477 ± 0.136		Squared	0.484 ± 0.004	-4.611 ± 0.036
3.0	45°	0.350 ± 0.006	-5.185 ± 0.070	8.0	45°	0.500 ± 0.004	-4.644 ± 0.037
	Single-Stripped	0.350 ± 0.007	-5.186 ± 0.070		Single-Stripped	0.500 ± 0.004	-4.646 ± 0.037
	Double-Stripped	0.343 ± 0.007	-5.429 ± 0.068		Double-Stripped	0.498 ± 0.004	-4.701 ± 0.037
	ZigZag	0.349 ± 0.007	-5.198 ± 0.070		ZigZag	0.500 ± 0.004	-4.654 ± 0.037
	Attractive	0.479 ± 0.005	-6.986 ± 0.060		Attractive	0.541 ± 0.004	-5.405 ± 0.033
	Neutral	0.289 ± 0.008	-2.842 ± 0.078		Neutral	0.468 ± 0.004	-4.085 ± 0.036
	Squared	0.365 ± 0.007	-4.822 ± 0.063		Squared	0.497 ± 0.004	-4.603 ± 0.033
4.0	45°	0.403 ± 0.006	-4.852 ± 0.058	9.0	45°	0.511 ± 0.004	-4.635 ± 0.034
	Single-Stripped	0.403 ± 0.006	-4.854 ± 0.058		Single-Stripped	0.511 ± 0.004	-4.634 ± 0.034
	Double-Stripped	0.401 ± 0.006	-5.007 ± 0.057		Double-Stripped	0.510 ± 0.004	-4.681 ± 0.034
	ZigZag	0.404 ± 0.006	-4.889 ± 0.059		ZigZag	0.511 ± 0.004	-4.645 ± 0.035
	Attractive	0.498 ± 0.005	-6.311 ± 0.050		Attractive	0.547 ± 0.003	-5.311 ± 0.031
	Neutral	0.357 ± 0.007	-3.420 ± 0.062		Neutral	0.481 ± 0.004	-4.144 ± 0.033
	Squared	0.412 ± 0.006	-4.680 ± 0.051		Squared	0.508 ± 0.004	-4.599 ± 0.031
5.0	45°	0.439 ± 0.005	-4.732 ± 0.049	10.0	45°	0.521 ± 0.004	-4.627 ± 0.032
	Single-Stripped	0.440 ± 0.005	-4.733 ± 0.049		Single-Stripped	0.521 ± 0.004	-4.628 ± 0.032
	Double-Stripped	0.437 ± 0.005	-4.834 ± 0.049		Double-Stripped	0.520 ± 0.004	-4.671 ± 0.032
	ZigZag	0.440 ± 0.005	-4.755 ± 0.050		ZigZag	0.520 ± 0.004	-4.634 ± 0.033
	Attractive	0.512 ± 0.004	-5.930 ± 0.043		Attractive	0.552 ± 0.003	-5.236 ± 0.030
	Neutral	0.399 ± 0.006	-3.711 ± 0.051		Neutral	0.492 ± 0.004	-4.191 ± 0.031
	Squared	0.444 ± 0.005	-4.637 ± 0.044		Squared	0.516 ± 0.004	-4.595 ± 0.030
6.0	45°	0.465 ± 0.005	-4.681 ± 0.044	11.0	45°	0.528 ± 0.003	-4.623 ± 0.030
	Single-Stripped	0.465 ± 0.005	-4.681 ± 0.044		Single-Stripped	0.529 ± 0.003	-4.624 ± 0.030
	Double-Stripped	0.464 ± 0.005	-4.765 ± 0.044		Double-Stripped	0.527 ± 0.003	-4.659 ± 0.031
	ZigZag	0.466 ± 0.005	-4.702 ± 0.044		ZigZag	0.528 ± 0.003	-4.627 ± 0.031
	Attractive	0.524 ± 0.004	-5.689 ± 0.038				
	Neutral	0.429 ± 0.005	-3.887 ± 0.044				
	Squared	0.466 ± 0.005	-4.619 ± 0.039				
7.0	45°	0.485 ± 0.004	-4.659 ± 0.040				
	Single-Stripped	0.485 ± 0.004	-4.662 ± 0.039				
	Double-Stripped	0.483 ± 0.004	-4.725 ± 0.040				
	ZigZag	0.485 ± 0.004	-4.674 ± 0.040				

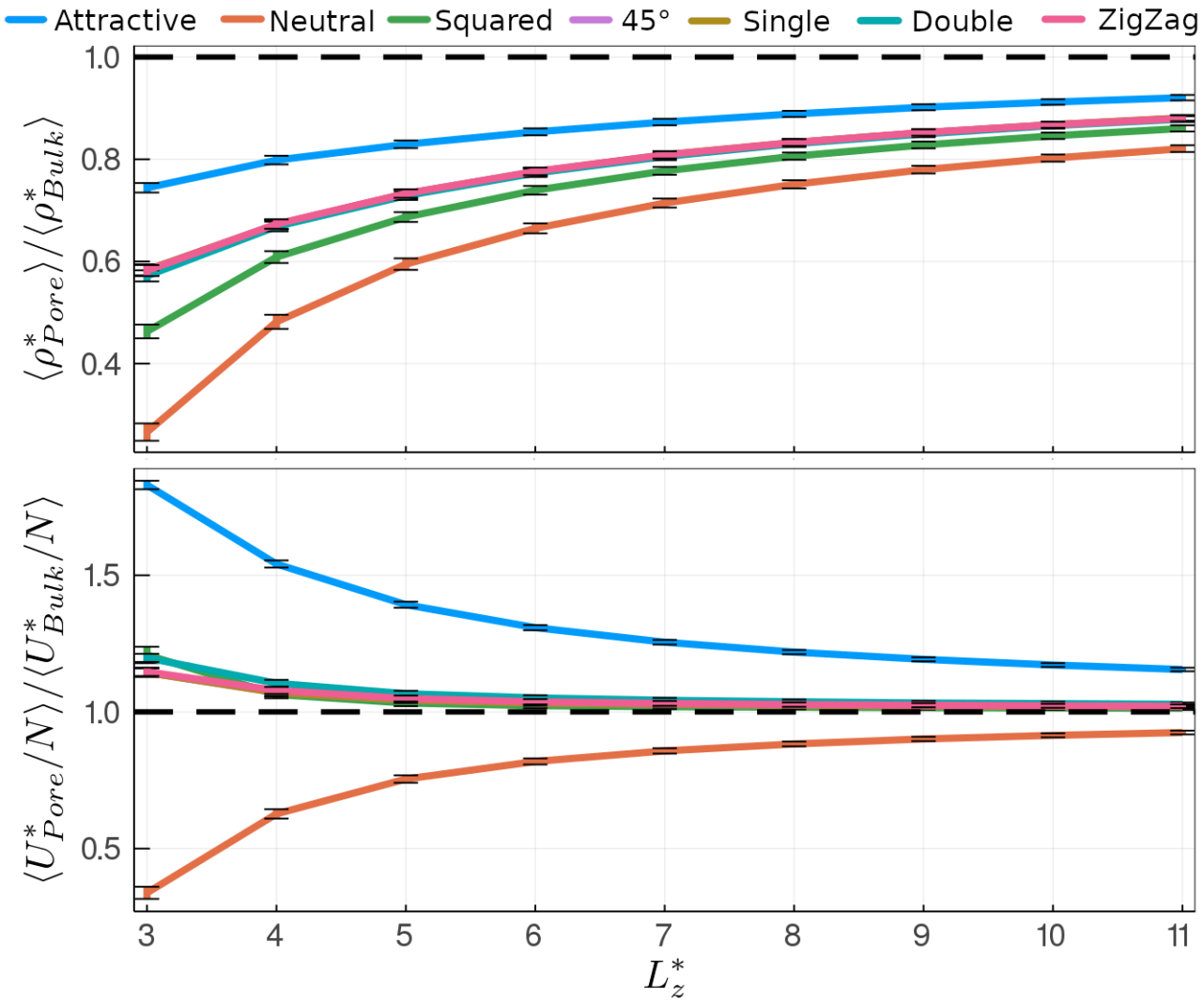

Figure 5.7: Visual summary of table 5.3 for the $T^* = 1.5, \rho^*_{Bulk} = 0.6, \mu^* = -1.652$ system. Upper panel displays average adsorption density normalized with its bulk density while lower panel displays average total energy per particle normalized with its bulk analogue.

$\langle \boldsymbol{\rho^*_{Pore}} \rangle / \langle \boldsymbol{\rho^*_{Bulk}} \rangle$: As the chemical potential increases, the confinement no longer has the same imposing presence on the fluid. This is validated with the similar four adsorption curves, with only the the squared one being the one out, pressumably due to the contiguous HS-SW areas.

$\langle \boldsymbol{U^*_{Pore}/N} \rangle / \langle \boldsymbol{U^*_{Bulk}/N} \rangle$: Energy curves overlapping reinforces the previous mentioned hypothesis, at least for pore separations ranging values $L^*_z \geq 4$.

The increments in the chemical potential disable the recognition of an evident adsorption pattern for most of the lithographic patterns, as fluid molecules are equally located across the whole area. The squared one is the only exception, as a higher rate of molecules are found in the attractive section of the wall, but not by a large margin.

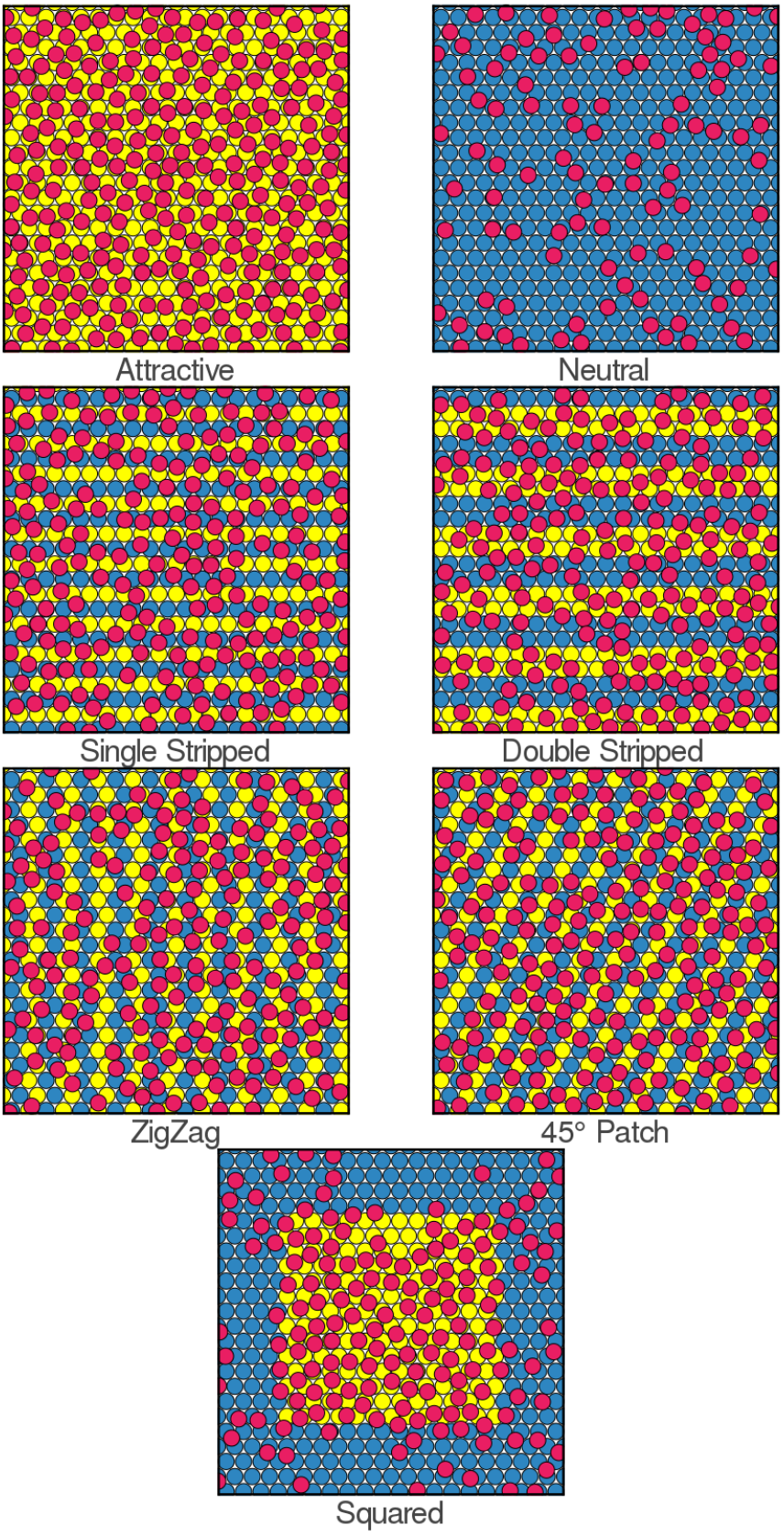

Figure 5.8: First adsorption layer (molecules 1.5σ units apart from the wall) of the designed lithographic patterns for the $T^* = 1.5, \rho^*_{Bulk} = 0.6, \mu^* = -1.652$ system. Color scheme: **Yellow** for SW (attractive), **Blue** for HS (neutral) and **Red** for fluid's molecules.

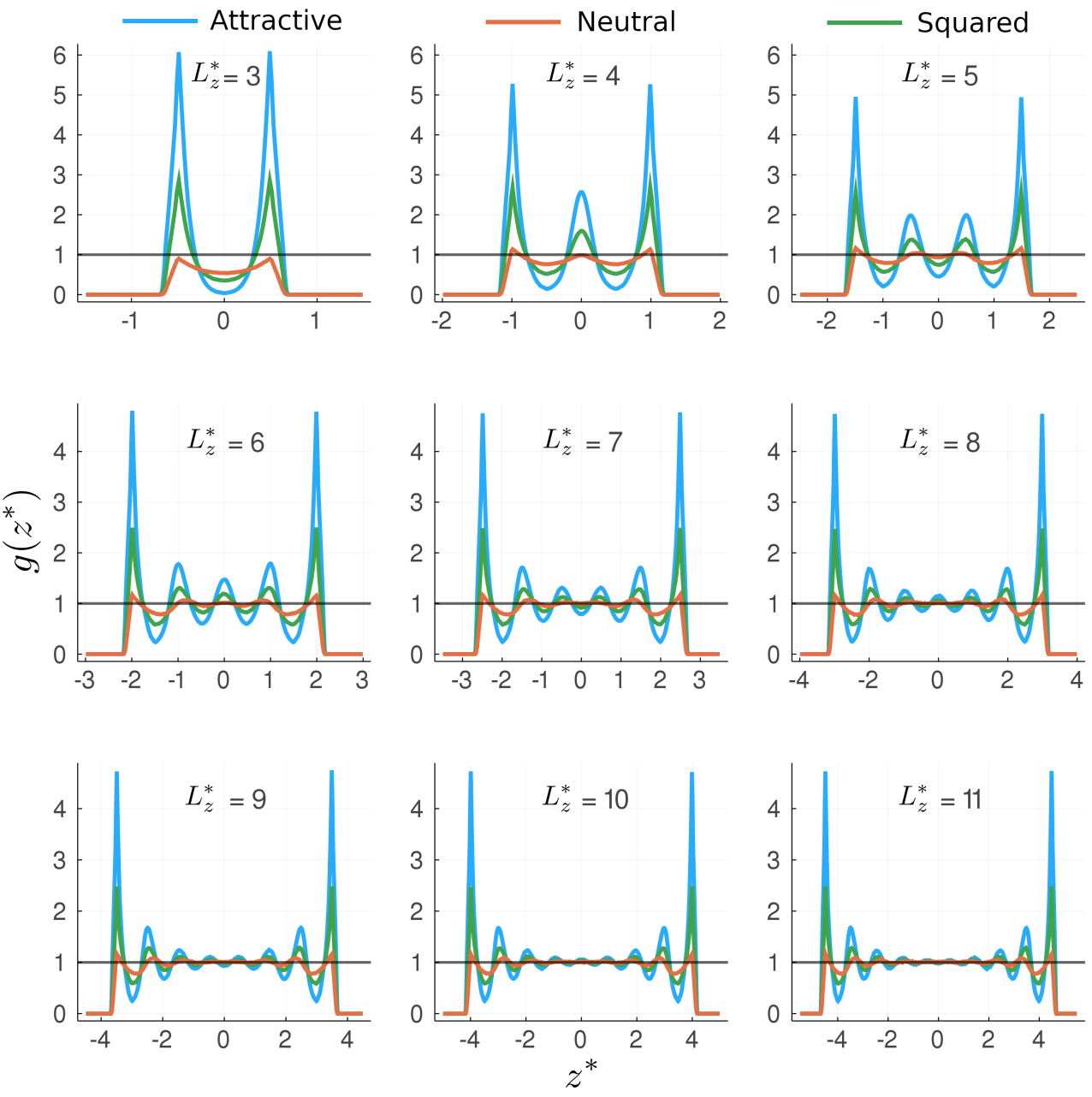

Figure 5.9: Distribution profiles normalized with the bulk density for the $T^* = 1.5, \rho^*_{Bulk} = 0.6, \mu^* = -1.652$ system. Pore separations range from $L_z = 3\sigma$ to $L_z = 11\sigma$, $L_z \in \mathbb{Z}$. Color scheme represents: **Blue** for attractive (SW), **Orange** for neutral (HS) and **Green** for squared slit-like walls' designs.

The density distribution profiles display a large amount of oscillations around the center of each pore, with most of the molecules found near the wall. This is true even for the neutral case, where the presence of the wall plays a higher role than previous cases while not allowing the confined fluid have bulk-like regions.

$$T^* = 3.0 \quad \rho^*_{Bulk} = 0.1 \quad \mu^* = -6.746$$

Low-density and high-temperature system with adsorption values ranging from 0.036 to 0.097. Calculated values are very similar across all the lithographic patterns, but none of these get close to the bulk density infering a reduced adsorption as temperature raises.

Energies may be englobed in two groups, the more energetic one consisting of the Double-Stripped and Squared designs and the less energetic made up of the 45°, Single-Stripped and ZigZag patterns.

Table 5.4: Sixty-three entries corresponding to the $T^* = 3.0, \rho^*_{Bulk} = 0.1$ and $\mu^* = -6.746$ system, segmented according the walls' separation and pattern design.

μVT ensemble for a confined system with multiple pattern designs.							
L^*_z	Decoration	$\langle \rho^*_{Pore} \rangle$	$\langle U^*/N \rangle$	L^*_z	Decoration	$\langle \rho^*_{Pore} \rangle$	$\langle U^*/N \rangle$
	Attractive	0.089 ± 0.007	-4.243 ± 0.161		Attractive	0.096 ± 0.005	-1.905 ± 0.104
	Neutral	0.036 ± 0.005	-0.291 ± 0.085		Neutral	0.076 ± 0.005	-0.608 ± 0.059
	Squared	0.055 ± 0.006	-2.498 ± 0.277		Squared	0.083 ± 0.005	-1.133 ± 0.087
3.0	45°	0.056 ± 0.006	-2.079 ± 0.136	8.0	45°	0.084 ± 0.005	-1.052 ± 0.067
	Single-Stripped	0.056 ± 0.006	-2.075 ± 0.136		Single-Stripped	0.084 ± 0.005	-1.050 ± 0.067
	Double-Stripped	0.059 ± 0.006	-2.441 ± 0.186		Double-Stripped	0.085 ± 0.005	-1.159 ± 0.077
	ZigZag	0.056 ± 0.006	-2.110 ± 0.139		ZigZag	0.084 ± 0.005	-1.062 ± 0.068
	Attractive	0.093 ± 0.007	-3.220 ± 0.150		Attractive	0.097 ± 0.005	-1.766 ± 0.095
	Neutral	0.052 ± 0.005	-0.459 ± 0.084		Neutral	0.079 ± 0.004	-0.618 ± 0.055
	Squared	0.067 ± 0.006	-1.801 ± 0.178		Squared	0.085 ± 0.005	-1.075 ± 0.080
4.0	45°	0.068 ± 0.006	-1.586 ± 0.111	9.0	45°	0.086 ± 0.005	-1.004 ± 0.062
	Single-Stripped	0.068 ± 0.006	-1.585 ± 0.111		Single-Stripped	0.086 ± 0.005	-1.004 ± 0.062
	Double-Stripped	0.070 ± 0.006	-1.829 ± 0.140		Double-Stripped	0.087 ± 0.005	-1.097 ± 0.071
	ZigZag	0.068 ± 0.006	-1.609 ± 0.114		ZigZag	0.086 ± 0.005	-1.012 ± 0.063
	Attractive	0.094 ± 0.006	-2.680 ± 0.138		Attractive	0.097 ± 0.005	-1.655 ± 0.089
	Neutral	0.062 ± 0.005	-0.531 ± 0.076		Neutral	0.081 ± 0.004	-0.627 ± 0.053
	Squared	0.073 ± 0.006	-1.496 ± 0.139		Squared	0.087 ± 0.004	-1.030 ± 0.072
5.0	45°	0.074 ± 0.006	-1.345 ± 0.094	10.0	45°	0.087 ± 0.004	-0.969 ± 0.057
	Single-Stripped	0.074 ± 0.006	-1.344 ± 0.094		Single-Stripped	0.087 ± 0.004	-0.967 ± 0.058
	Double-Stripped	0.076 ± 0.006	-1.531 ± 0.115		Double-Stripped	0.088 ± 0.004	-1.051 ± 0.065
	ZigZag	0.075 ± 0.006	-1.363 ± 0.097		ZigZag	0.087 ± 0.004	-0.975 ± 0.058
	Attractive	0.095 ± 0.006	-2.332 ± 0.126		Attractive	0.097 ± 0.004	-1.564 ± 0.081
	Neutral	0.068 ± 0.005	-0.570 ± 0.069		Neutral	0.083 ± 0.004	-0.634 ± 0.049
	Squared	0.078 ± 0.005	-1.323 ± 0.115		Squared	0.088 ± 0.004	-0.995 ± 0.066
6.0	45°	0.079 ± 0.005	-1.206 ± 0.082	11.0	45°	0.088 ± 0.004	-0.939 ± 0.055
	Single-Stripped	0.079 ± 0.005	-1.205 ± 0.083		Single-Stripped	0.088 ± 0.004	-0.938 ± 0.055
	Double-Stripped	0.080 ± 0.005	-1.355 ± 0.099		Double-Stripped	0.089 ± 0.004	-1.013 ± 0.061
	ZigZag	0.079 ± 0.005	-1.220 ± 0.084		ZigZag	0.088 ± 0.004	-0.945 ± 0.055
	Attractive	0.096 ± 0.005	-2.087 ± 0.114				
	Neutral	0.073 ± 0.005	-0.592 ± 0.064				
	Squared	0.081 ± 0.005	-1.212 ± 0.100				
7.0	45°	0.082 ± 0.005	-1.115 ± 0.074				
	Single-Stripped	0.082 ± 0.005	-1.115 ± 0.073				
	Double-Stripped	0.083 ± 0.005	-1.238 ± 0.086				
	ZigZag	0.082 ± 0.005	-1.126 ± 0.075				

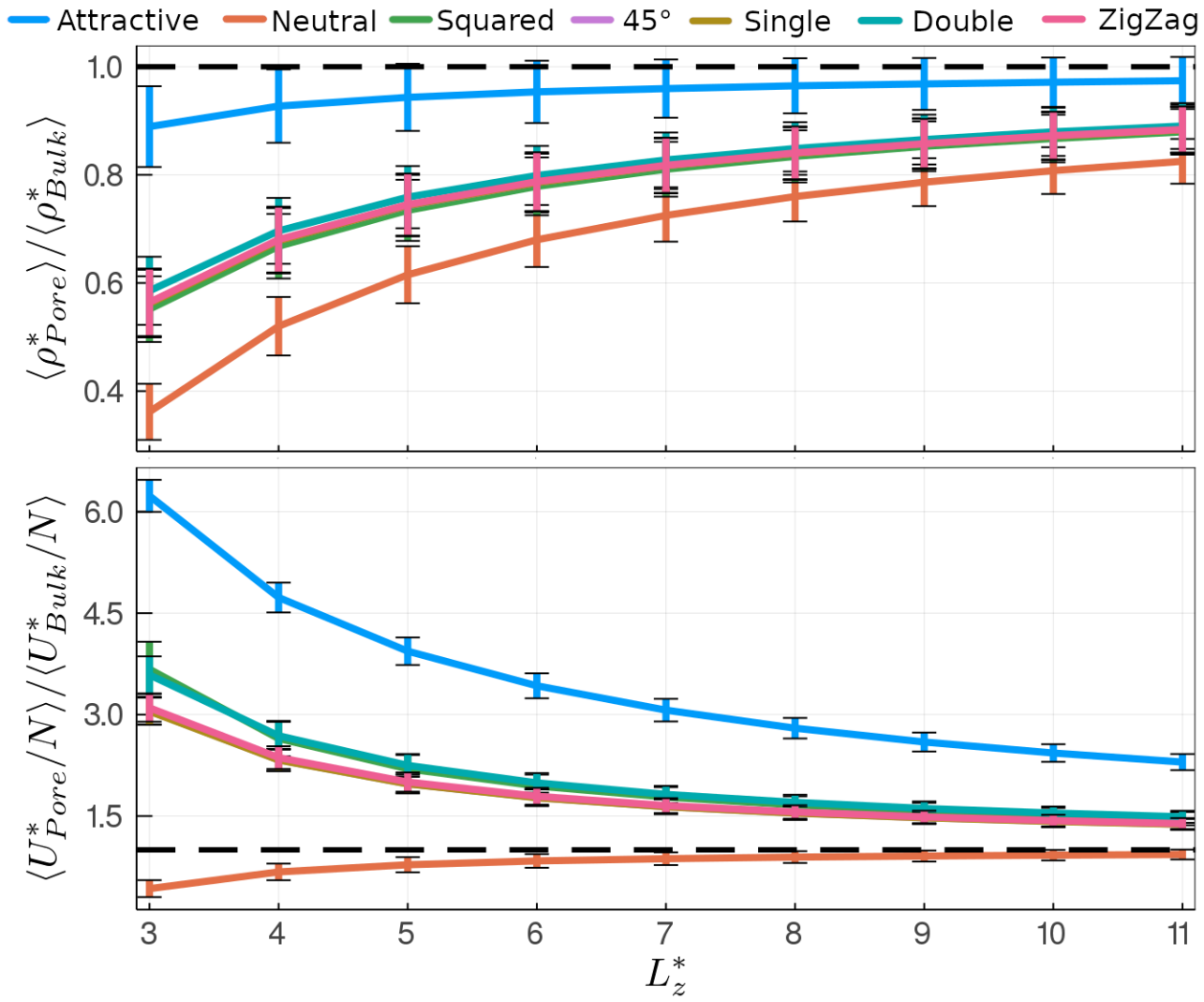

Figure 5.10: Visual summary of table 5.4 for the $T^* = 3.0, \rho^*_{Bulk} = 0.1, \mu^* = -6.746$ system. Upper panel displays average adsorption density normalized with its bulk density while lower panel displays average total energy per particle normalized with its bulk analogue.

$\langle \boldsymbol{\rho^*_{Pore}} \rangle / \langle \boldsymbol{\rho^*_{Bulk}} \rangle$: The increment in the temperature reduced the individual contributions of the designed patterns, with all five of them displaying very similar values for each of the separations.

$\langle \boldsymbol{U^*_{Pore}/N} \rangle / \langle \boldsymbol{U^*_{Bulk}/N} \rangle$: The identification of the two groups of curves is largely notable, with the Squared and Two-Stripped designs having slightly higher energetic values than the lower group constituted by the 45°, Single-Stripped and ZigZag patterns.

The adsorption of the pores drastically decreased as temperature raised, with the adsorbed molecules no longer being located primarily on the attractive sections. For example, the elected frame for the squared pattern has 53% of the fluid molecules interacting with SW wall's molecules and 47% with only HS wall's molecules.

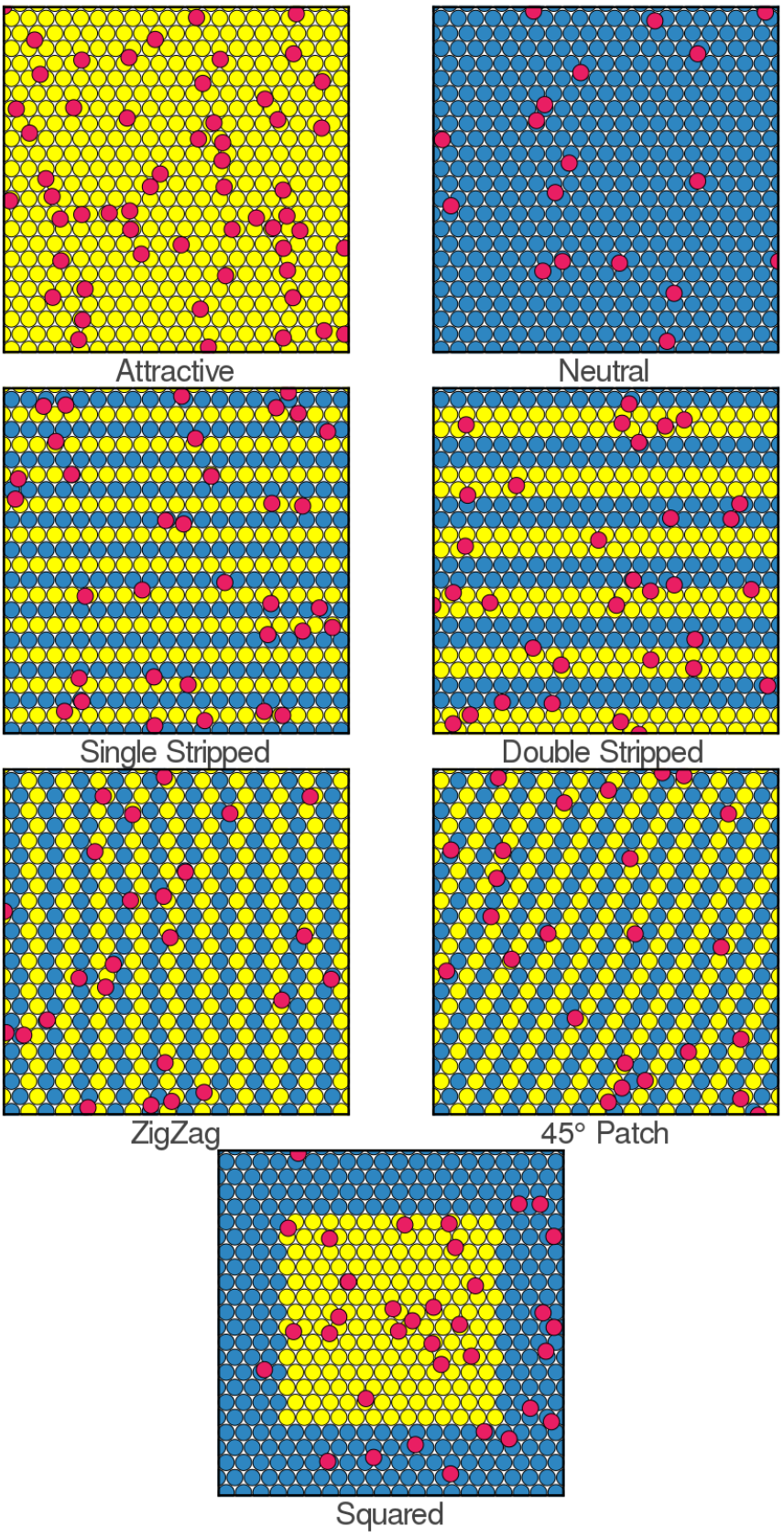

Figure 5.11: First adsorption layer (molecules 1.5σ units apart from the wall) of the designed lithographic patterns for the $T^* = 3.0, \rho^*_{Bulk} = 0.1, \mu^* = -6.746$ system. Color scheme: **Yellow** for SW (attractive), **Blue** for HS (neutral) and **Red** for fluid's molecules.

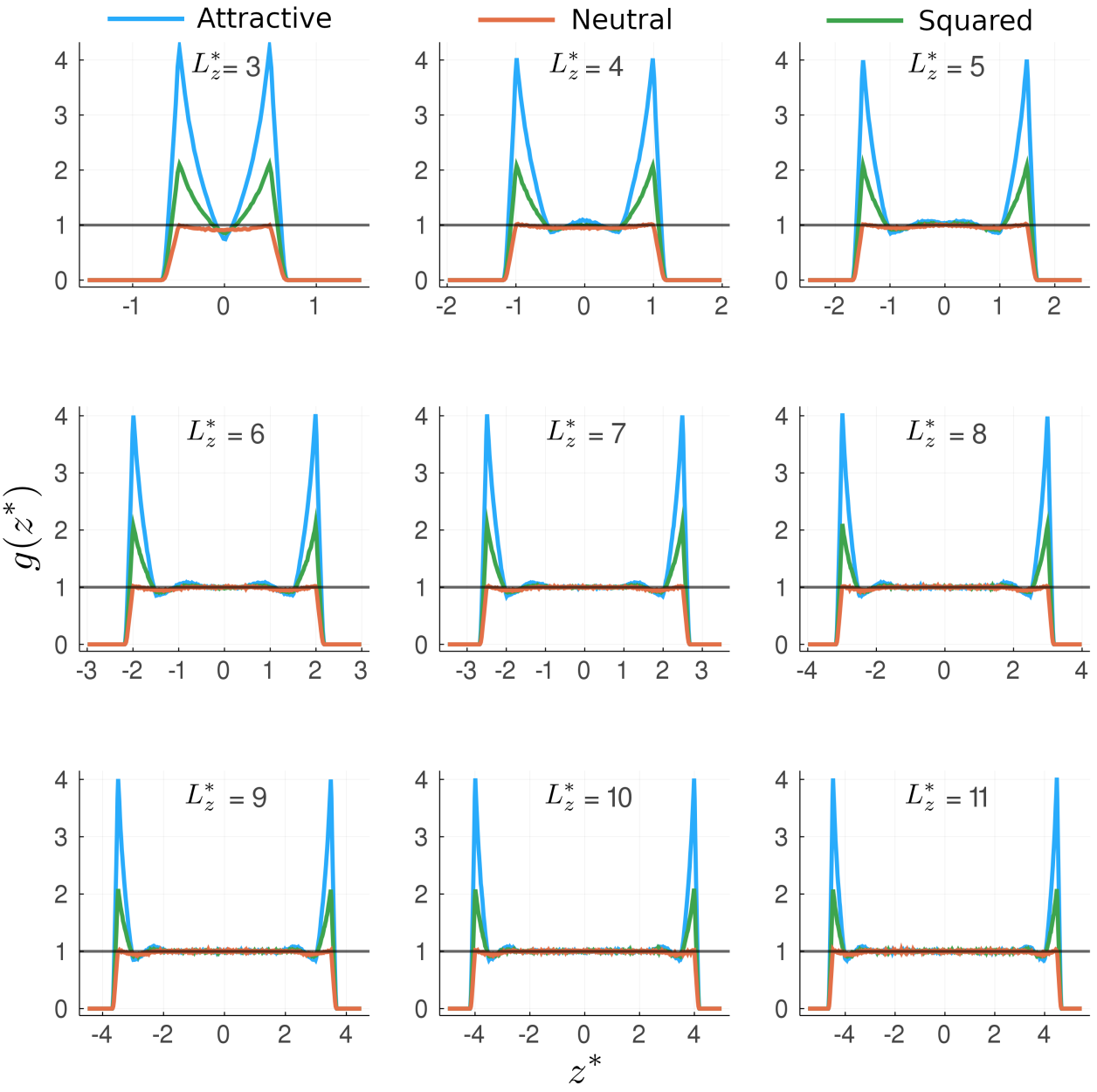

Figure 5.12: Distribution profiles normalized with the bulk density for the $T^* = 3.0, \rho^*_{Bulk} = 0.1, \mu^* = -6.746$ system. Pore separations range from $L_z = 3\sigma$ to $L_z = 11\sigma$, $L_z \in \mathbb{Z}$. Color scheme represents: **Blue** for attractive (SW), **Orange** for neutral (HS) and **Green** for squared slit-like walls' designs.

Unlike previous density distribution profiles, the ones listed for this system result in sharper curves with few-to-non oscillations for the averaged allocation of molecules. The abrupt flattening of the profiles as the separation of the wall's increases ($L_z^* = 4$ for the neutral wall and $L_z^* = 6$ for the attractive and squared designs) indicates the diminishing role the the confining interface plays on the fluid, with molecules no longer sharing the chained interaction.

$$T^* = 3.0 \quad \rho^*_{Bulk} = 0.3 \quad \mu^* = -2.421$$

Medium-density and and high-temperature system with adsorption values ranging from 0.111 to 0.276. Once again each calculated value regarding either the adsorption density or total energy per particle result in very similar numbers for each of the segmented sections, indicating the separation of the walls.

Table 5.5: Sixty-three entries corresponding to the $T^* = 3.0, \rho^*_{Bulk} = 0.3$ and $\mu^* = -2.421$ system, segmented according the walls' separation and pattern design.

μVT ensemble for a confined system with multiple pattern designs.							
L^*_z	Decoration	$\langle \rho^*_{Pore} \rangle$	$\langle U^*/N \rangle$	L^*_z	Decoration	$\langle \rho^*_{Pore} \rangle$	$\langle U^*/N \rangle$
	Attractive	0.213 ± 0.008	-5.478 ± 0.109		Attractive	0.267 ± 0.006	-3.051 ± 0.059
	Neutral	0.111 ± 0.008	-0.915 ± 0.085		Neutral	0.230 ± 0.006	-1.829 ± 0.060
	Squared	0.149 ± 0.008	-3.221 ± 0.169		Squared	0.244 ± 0.006	-2.310 ± 0.060
3.0	45°	0.156 ± 0.008	-2.993 ± 0.102	8.0	45°	0.247 ± 0.006	-2.298 ± 0.057
	Single-Stripped	0.156 ± 0.008	-2.992 ± 0.103		Single-Stripped	0.247 ± 0.006	-2.298 ± 0.056
	Double-Stripped	0.158 ± 0.008	-3.289 ± 0.122		Double-Stripped	0.248 ± 0.006	-2.370 ± 0.058
	ZigZag	0.156 ± 0.008	-3.017 ± 0.103		ZigZag	0.247 ± 0.006	-2.307 ± 0.057
	Attractive	0.233 ± 0.008	-4.299 ± 0.090		Attractive	0.271 ± 0.006	-2.929 ± 0.055
	Neutral	0.159 ± 0.008	-1.391 ± 0.085		Neutral	0.237 ± 0.006	-1.862 ± 0.056
	Squared	0.186 ± 0.008	-2.691 ± 0.104		Squared	0.250 ± 0.006	-2.277 ± 0.056
4.0	45°	0.193 ± 0.008	-2.646 ± 0.083	9.0	45°	0.253 ± 0.006	-2.268 ± 0.053
	Single-Stripped	0.193 ± 0.008	-2.644 ± 0.083		Single-Stripped	0.253 ± 0.006	-2.267 ± 0.054
	Double-Stripped	0.194 ± 0.008	-2.820 ± 0.089		Double-Stripped	0.253 ± 0.006	-2.330 ± 0.054
	ZigZag	0.193 ± 0.008	-2.665 ± 0.085		ZigZag	0.253 ± 0.006	-2.275 ± 0.053
	Attractive	0.247 ± 0.007	-3.765 ± 0.078		Attractive	0.274 ± 0.006	-2.836 ± 0.052
	Neutral	0.187 ± 0.007	-1.603 ± 0.079		Neutral	0.244 ± 0.006	-1.887 ± 0.053
	Squared	0.210 ± 0.007	-2.516 ± 0.083		Squared	0.255 ± 0.006	-2.251 ± 0.053
5.0	45°	0.215 ± 0.007	-2.493 ± 0.073	10.0	45°	0.257 ± 0.006	-2.244 ± 0.050
	Single-Stripped	0.215 ± 0.007	-2.490 ± 0.073		Single-Stripped	0.258 ± 0.006	-2.244 ± 0.050
	Double-Stripped	0.216 ± 0.007	-2.622 ± 0.076		Double-Stripped	0.258 ± 0.006	-2.299 ± 0.051
	ZigZag	0.215 ± 0.007	-2.506 ± 0.074		ZigZag	0.258 ± 0.006	-2.250 ± 0.050
	Attractive	0.256 ± 0.007	-3.437 ± 0.070		Attractive	0.276 ± 0.005	-2.759 ± 0.049
	Neutral	0.206 ± 0.007	-1.714 ± 0.071		Neutral	0.249 ± 0.005	-1.906 ± 0.050
	Squared	0.225 ± 0.007	-2.417 ± 0.073		Squared	0.259 ± 0.005	-2.232 ± 0.050
6.0	45°	0.229 ± 0.007	-2.400 ± 0.066	11.0	45°	0.261 ± 0.006	-2.225 ± 0.048
	Single-Stripped	0.229 ± 0.007	-2.400 ± 0.067		Single-Stripped	0.261 ± 0.006	-2.225 ± 0.048
	Double-Stripped	0.230 ± 0.007	-2.503 ± 0.068		Double-Stripped	0.262 ± 0.005	-2.275 ± 0.048
	ZigZag	0.229 ± 0.007	-2.411 ± 0.067		ZigZag	0.262 ± 0.005	-2.231 ± 0.047
	Attractive	0.263 ± 0.006	-3.214 ± 0.064				
	Neutral	0.219 ± 0.007	-1.783 ± 0.065				
	Squared	0.236 ± 0.006	-2.354 ± 0.065				
7.0	45°	0.239 ± 0.007	-2.340 ± 0.061				
	Single-Stripped	0.239 ± 0.007	-2.340 ± 0.061				
	Double-Stripped	0.240 ± 0.007	-2.425 ± 0.063				
	ZigZag	0.239 ± 0.007	-2.350 ± 0.061				

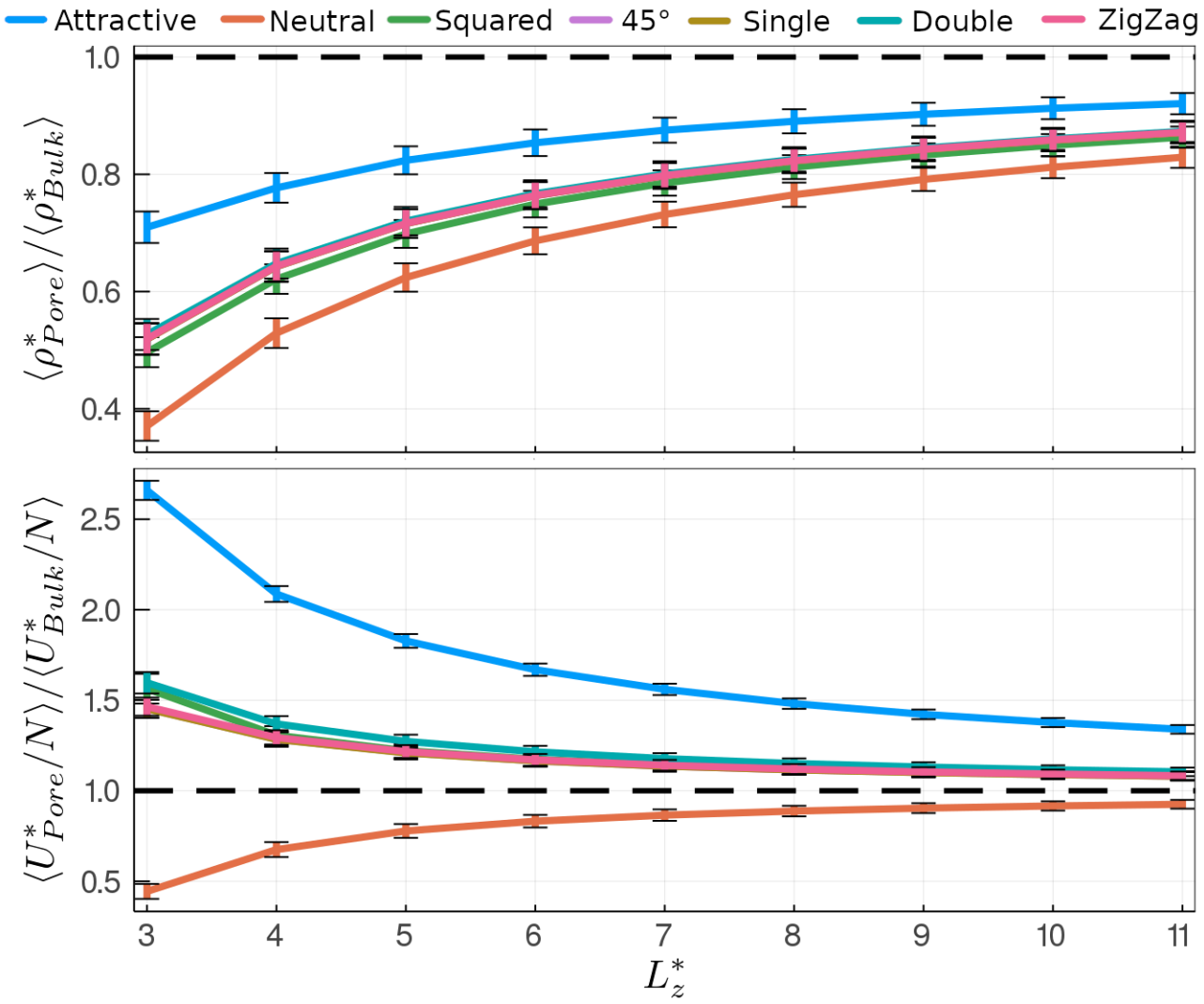

Figure 5.13: Visual summary of table 5.6 for the $T^* = 3.0, \rho^*_{Bulk} = 0.3, \mu^* = -2.421$ system. Upper panel displays average adsorption density normalized with its bulk density while lower panel displays average total energy per particle normalized with its bulk analogue.

$\langle \boldsymbol{\rho^*_{Pore}} \rangle / \langle \boldsymbol{\rho^*_{Bulk}} \rangle$: The evolution of the adsorption of the system follows a similar set of values for each of the pattern designs, with the Squared lithographic pattern laying on slightly smaller values.

$\langle \boldsymbol{U^*_{Pore}/N} \rangle / \langle \boldsymbol{U^*_{Bulk}/N} \rangle$: Although a set of two groups could be define (like the previous case), their rather rapid converging tendencies for $L^*_z \geq 4\sigma$ makes them have identical values that fit within the error bars of each other.

The induced increment on the chemical potential and temperature indicates that the fluid no longer is greatly influenced by the lithographic design of the walls, as the adsorbed molecules homogeneously distribute on the proximities of the walls.

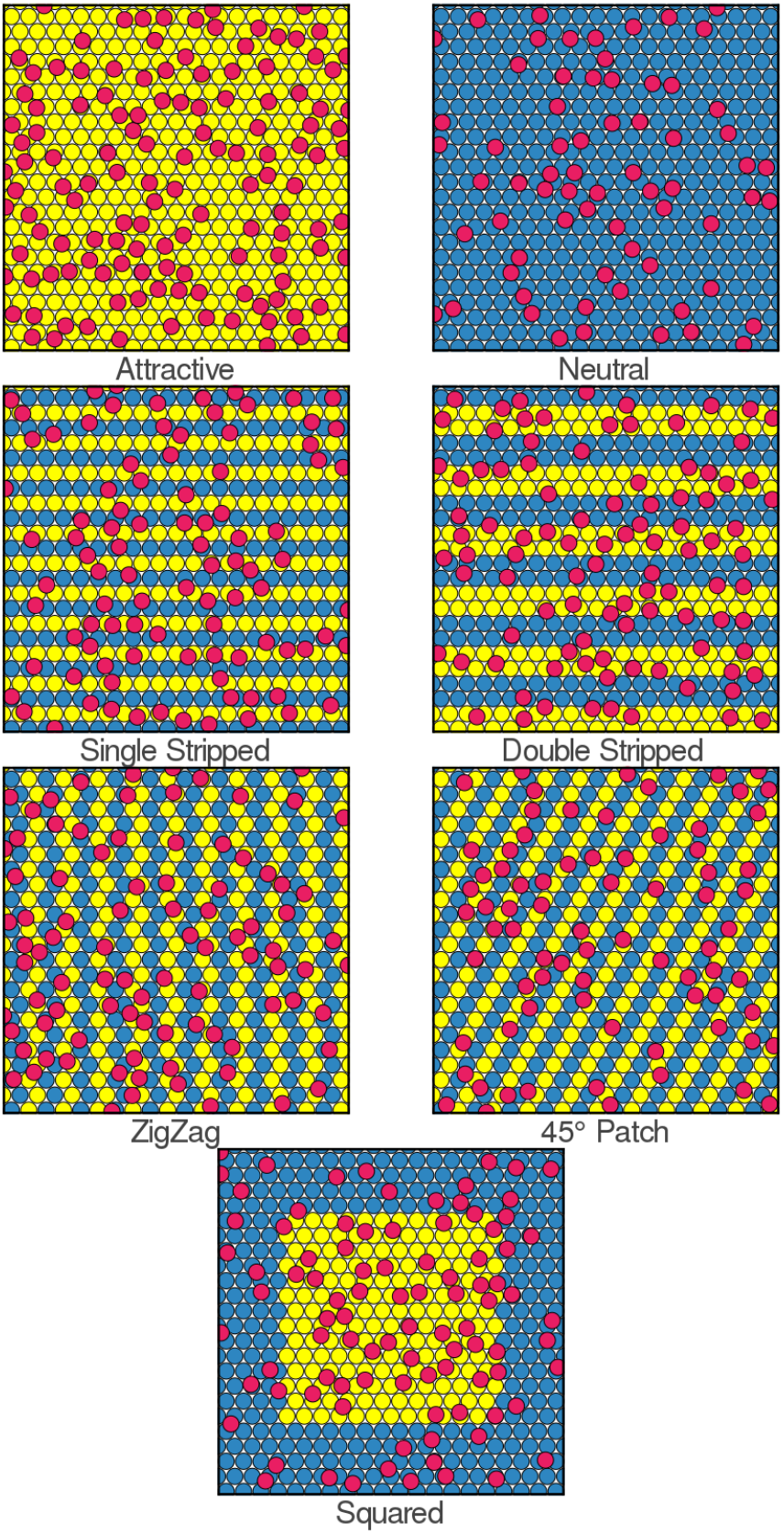

Figure 5.14: First adsorption layer (molecules 1.5σ units apart from the wall) of the designed lithographic patterns for the $T^* = 3.0, \rho^*_{Bulk} = 0.3, \mu^* = -2.421$ system. Color scheme: **Yellow** for SW (attractive), **Blue** for HS (neutral) and **Red** for fluid's molecules.

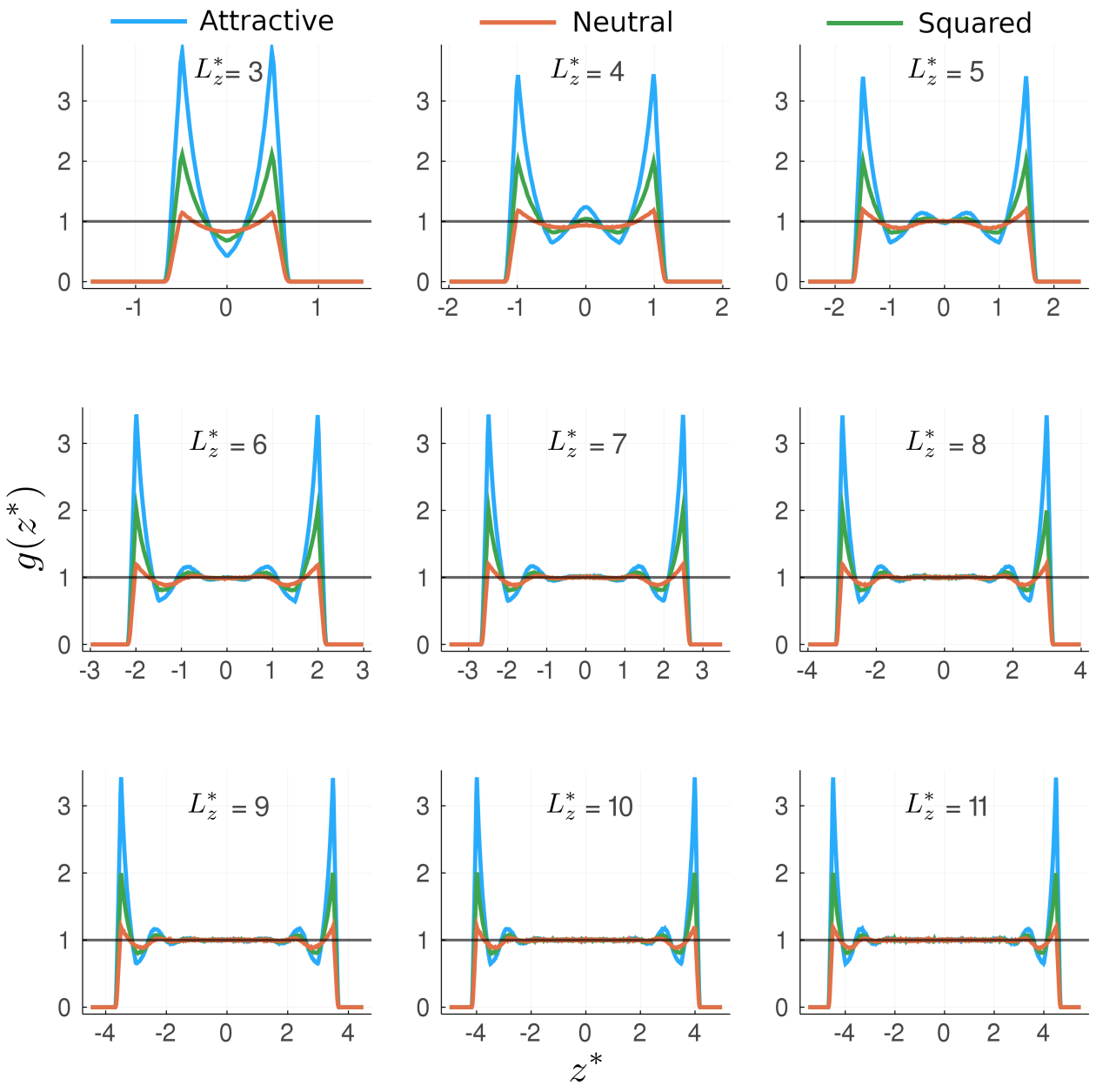

Figure 5.15: Distribution profiles normalized with the bulk density for the $T^* = 3.0, \rho^*_{Bulk} = 0.3, \mu^* = -2.421$ system. Pore separations range from $L_z = 3\sigma$ to $L_z = 11\sigma$, $L_z \in \mathbb{Z}$. Color scheme represents: **Blue** for attractive (SW), **Orange** for neutral (HS) and **Green** for squared slit-like walls' designs.

A drastic decrement for $g(z^*)$ near the walls reinforces the hypothesis that indicates that the confined fluid slowly tends to ignore the presence of the wall, followed by quickly-flattening oscillations into completely plain bulk-like fluid sections for those molecules found 2.5σ units away from the wall.

$$T^* = 3.0 \quad \rho^*_{Bulk} = 0.6 \quad \mu^* = 5.699$$

High-density and high-temperature system with adsorption values ranging from 0.313 to 0.541. Although the adsorption values fall well bellow the bulk density, a minor distinction of the squared pattern may be recognized from the rest of the patterns that lay in slightly higher values. Despite this slight difference, as the separation increases they all still converge to the same values. The same behavior is true for the energy.

Table 5.6: Sixty-three entries corresponding to the $T^* = 3.0, \rho^*_{Bulk} = 0.6$ and $\mu^* = 5.699$ system, segmented according the walls' separation and pattern design.

μVT ensemble for a confined system with multiple pattern designs.							
L^*_z	Decoration	$\langle \rho^*_{Pore} \rangle$	$\langle U^*/N \rangle$	L^*_z	Decoration	$\langle \rho^*_{Pore} \rangle$	$\langle U^*/N \rangle$
	Attractive	0.402 ± 0.006	-7.460 ± 0.076		Attractive	0.518 ± 0.003	-5.098 ± 0.037
	Neutral	0.313 ± 0.006	-2.675 ± 0.062		Neutral	0.491 ± 0.004	-3.931 ± 0.037
	Squared	0.348 ± 0.006	-4.733 ± 0.077		Squared	0.502 ± 0.004	-4.378 ± 0.036
3.0	45°	0.361 ± 0.006	-5.025 ± 0.068	8.0	45°	0.506 ± 0.004	-4.459 ± 0.035
	Single-Stripped	0.361 ± 0.006	-5.025 ± 0.068		Single-Stripped	0.505 ± 0.004	-4.458 ± 0.036
	Double-Stripped	0.361 ± 0.006	-5.160 ± 0.071		Double-Stripped	0.505 ± 0.004	-4.491 ± 0.036
	ZigZag	0.361 ± 0.006	-5.038 ± 0.068		ZigZag	0.505 ± 0.004	-4.464 ± 0.036
	Attractive	0.442 ± 0.005	-6.262 ± 0.061		Attractive	0.528 ± 0.003	-5.000 ± 0.034
	Neutral	0.381 ± 0.005	-3.296 ± 0.056		Neutral	0.503 ± 0.003	-3.985 ± 0.034
	Squared	0.405 ± 0.005	-4.499 ± 0.059		Squared	0.513 ± 0.003	-4.372 ± 0.034
4.0	45°	0.413 ± 0.005	-4.693 ± 0.056	9.0	45°	0.516 ± 0.003	-4.442 ± 0.033
	Single-Stripped	0.414 ± 0.005	-4.694 ± 0.056		Single-Stripped	0.516 ± 0.003	-4.442 ± 0.033
	Double-Stripped	0.413 ± 0.005	-4.777 ± 0.057		Double-Stripped	0.516 ± 0.003	-4.471 ± 0.033
	ZigZag	0.414 ± 0.005	-4.708 ± 0.056		ZigZag	0.516 ± 0.003	-4.448 ± 0.033
	Attractive	0.470 ± 0.004	-5.714 ± 0.051		Attractive	0.535 ± 0.003	-4.925 ± 0.032
	Neutral	0.425 ± 0.005	-3.586 ± 0.049		Neutral	0.513 ± 0.003	-4.026 ± 0.032
	Squared	0.442 ± 0.004	-4.425 ± 0.050		Squared	0.522 ± 0.003	-4.368 ± 0.032
5.0	45°	0.448 ± 0.004	-4.568 ± 0.048	10.0	45°	0.525 ± 0.003	-4.430 ± 0.032
	Single-Stripped	0.449 ± 0.004	-4.569 ± 0.048		Single-Stripped	0.525 ± 0.003	-4.429 ± 0.031
	Double-Stripped	0.448 ± 0.004	-4.629 ± 0.048		Double-Stripped	0.525 ± 0.003	-4.455 ± 0.032
	ZigZag	0.449 ± 0.004	-4.580 ± 0.048		ZigZag	0.525 ± 0.003	-4.435 ± 0.032
	Attractive	0.491 ± 0.004	-5.416 ± 0.044		Attractive	0.541 ± 0.003	-4.866 ± 0.030
	Neutral	0.454 ± 0.004	-3.752 ± 0.044		Neutral	0.521 ± 0.003	-4.058 ± 0.030
	Squared	0.468 ± 0.004	-4.399 ± 0.044		Squared	0.529 ± 0.003	-4.364 ± 0.030
6.0	45°	0.473 ± 0.004	-4.512 ± 0.042	11.0	45°	0.532 ± 0.003	-4.420 ± 0.030
	Single-Stripped	0.474 ± 0.004	-4.512 ± 0.042		Single-Stripped	0.532 ± 0.003	-4.420 ± 0.030
	Double-Stripped	0.473 ± 0.004	-4.559 ± 0.043		Double-Stripped	0.532 ± 0.003	-4.443 ± 0.030
	ZigZag	0.474 ± 0.004	-4.521 ± 0.042		ZigZag	0.532 ± 0.003	-4.425 ± 0.030
	Attractive	0.506 ± 0.004	-5.228 ± 0.040				
	Neutral	0.475 ± 0.004	-3.857 ± 0.039				
	Squared	0.487 ± 0.004	-4.385 ± 0.040				
7.0	45°	0.492 ± 0.004	-4.480 ± 0.039				
	Single-Stripped	0.492 ± 0.004	-4.480 ± 0.038				
	Double-Stripped	0.491 ± 0.004	-4.518 ± 0.039				
	ZigZag	0.492 ± 0.004	-4.488 ± 0.039				

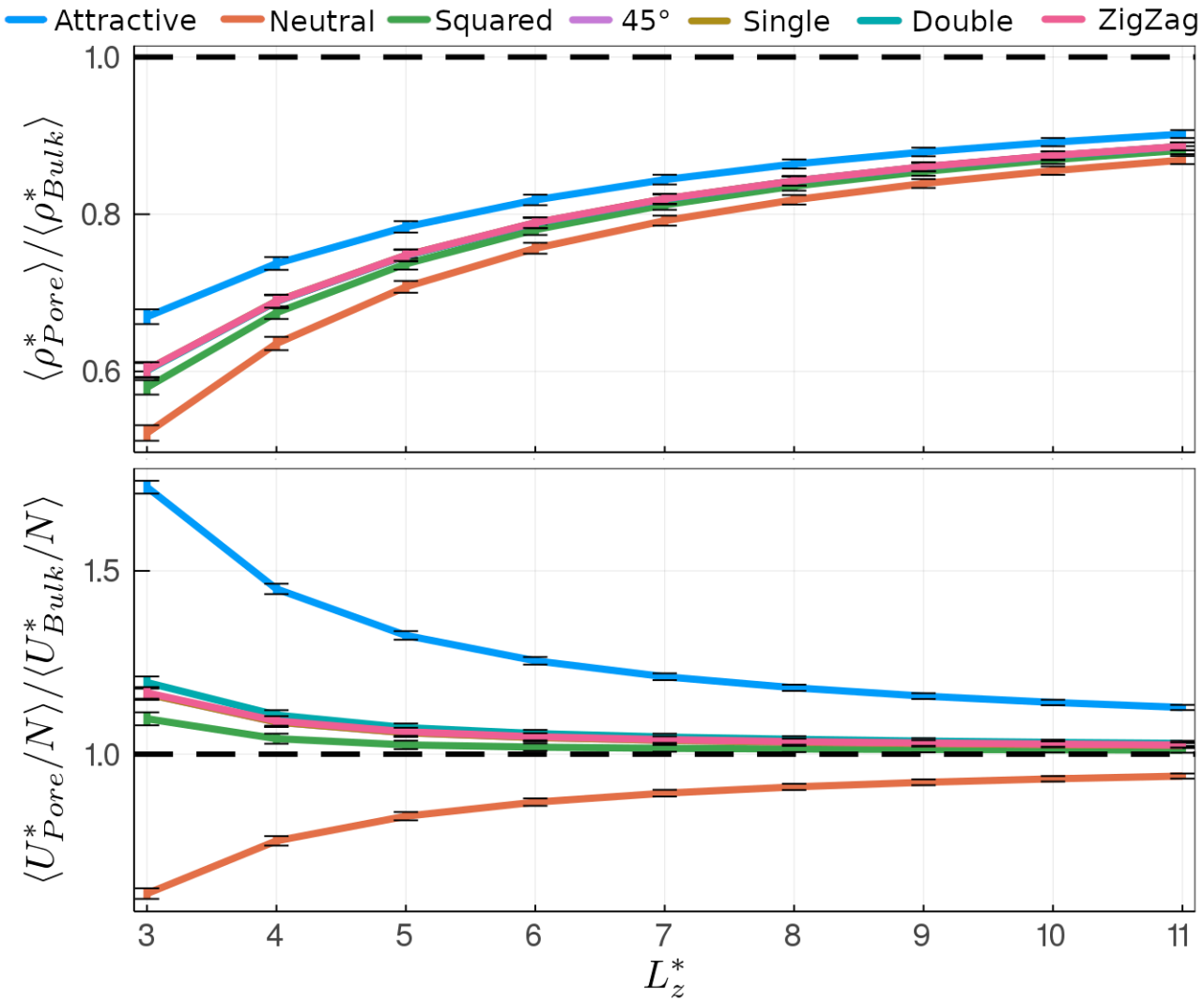

Figure 5.16: Visual summary of table 5.6 for the $T^* = 3.0, \rho^*_{Bulk} = 0.6, \mu^* = 5.699$ system. Upper panel displays average adsorption density normalized with its bulk density while lower panel displays average total energy per particle normalized with its bulk analogue.

$\langle \boldsymbol{\rho^*_{Pore}} \rangle / \langle \boldsymbol{\rho^*_{Bulk}} \rangle$: The gap of values for the control walls (attractive and neutral) drastically narrows, with most of the enclosed lithographic patterns displaying similar values, besides the squared design that stands out with lower values for short pore heights.

$\langle \boldsymbol{U^*_{Pore}/N} \rangle / \langle \boldsymbol{U^*_{Bulk}/N} \rangle$: Energetic values for the five different decorations coarsely fit to the bulk fluid, with more energetic values for highly confined fluids ($L^*_z = 3, 4, 5$).

The fluid's molecule no longer have a distinguishable preference for adsorption spots around SW interacting particles; the rather large chemical potential and temperature induces a higher omission of the design of the walls as their coverage by the fluid is homogeneously carried out.

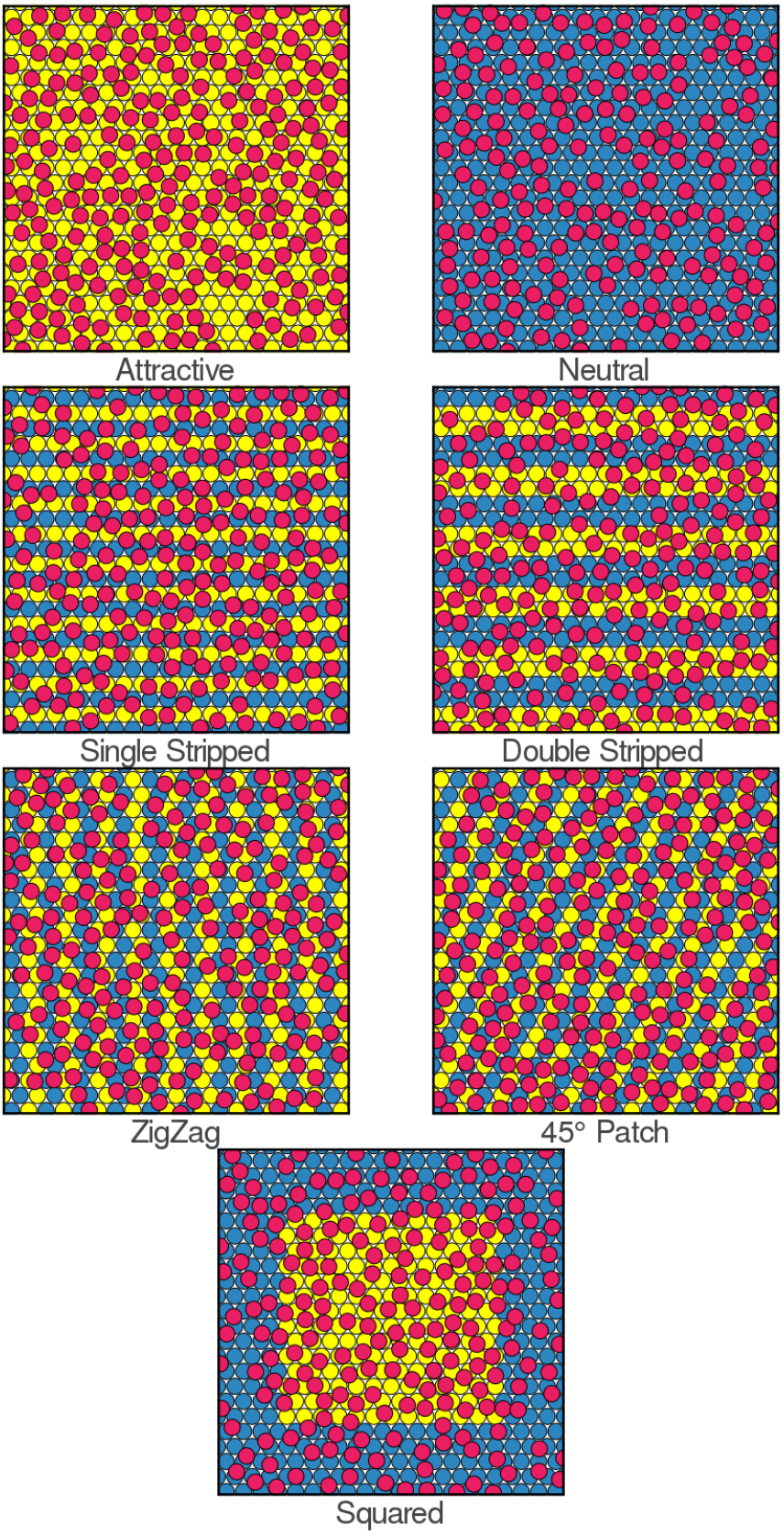

Figure 5.17: First adsorption layer (molecules 1.5σ units apart from the wall) of the designed lithographic patterns for the $T^* = 3.0, \rho^*_{Bulk} = 0.6, \mu^* = 5.699$ system. Color scheme: **Yellow** for SW (attractive), **Blue** for HS (neutral) and **Red** for fluid's molecules.

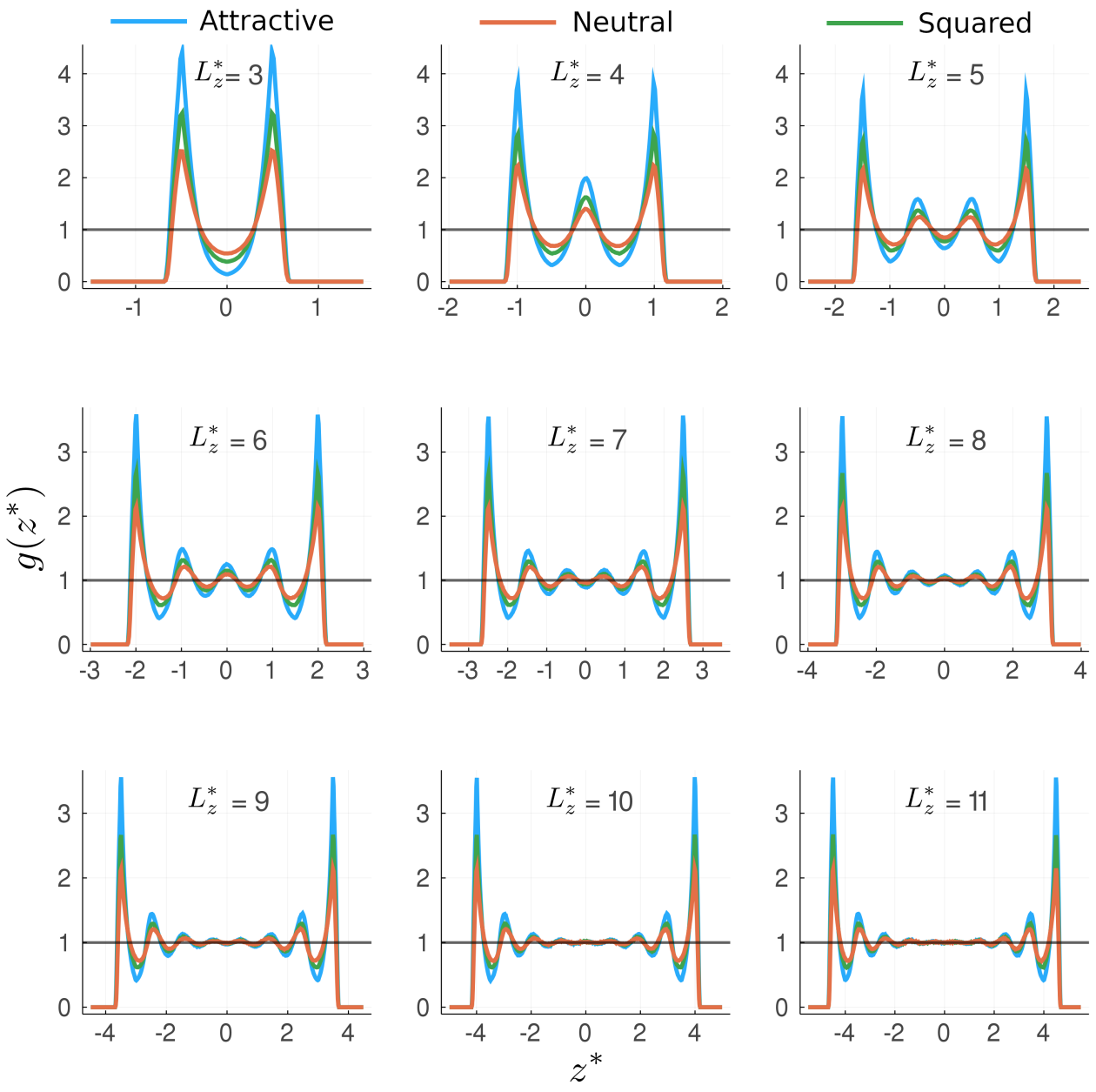

Figure 5.18: Distribution profiles normalized with the bulk density for the $T^* = 3.0, \rho^*_{Bulk} = 0.6, \mu^* = 5.699$ system. Pore separations range from $L_z = 3\sigma$ to $L_z = 11\sigma$, $L_z \in \mathbb{Z}$. Color scheme represents: **Blue** for attractive (SW), **Orange** for neutral (HS) and **Green** for squared slit-like walls' designs.

Out of all the six combinations of T^* and μ^* simulated under confinement, the high-temperature and high-density system is the only one that displays the three distribution profiles in figure 5.18 with similar curves. Across all the separation values calculated, the amount of oscillations and their location coincide (besides the height of those, as the walls still play a not-so-fundamental but still an active role) with a varely appreciable bulk-like behavior for molecules 5σ units away from the walls.

Conclusions

Confined systems, as important as they are, may have diverse adsorption densities depending on multiple parameters, such as chemical potential and temperature. This work contemplates the contribution of walls conformed by a combination of Square-Well (attractive) and Hard-Sphere (neutral) interacting molecules, resembling multiple lithographic pattern arrangements.

To this end, a set of temperatures and densities for Square-Well interacting fluids were elected (keeping in mind the vapor-liquid coexistence binodal) for a total of twelve privileged systems to be simulated in the canonical ensemble (NVT constant) via Monte Carlo techniques with the Metropolis' acceptance/rejection criteria to average the chemical potential over the ensembles, a fundamental thermodynamic property in adsorption problems. Afterwards, a set of simulations in the grand canonical ensemble (μVT constant) were carried out for optimal parameter fitting and consistency validation.

Previous calculations serve valuable information related to the structural composition of the fluid, with only six out of the twelve systems revealing remarkable characteristics that would result in attractive objects of study under confinement. The spatial restriction was achieved with two slit-like walls composed of an arrangement of attractive and neutral interacting molecules in an hexagonal-closed packing fashion, with variable separation ranging from 3σ to 11σ along the z-axis. The design of the walls was meticulous, with two of them being wholly attractive and neutral (to play a control variable role) and five different lithographic designs consisting of an equal ratio of covered area for both interactions previously mentioned.

A total of three hundred seventy-eight confined simulations were allocated in vast computational resources, with their results discussed in chapter 5. The analysis indicates that:

1. Out of the five established decorations, three of these have really similar behaviors throughout the systems; these correspond to the 45°, single-stripped and zigzag decorations. The first two mentioned decorations are identical with only a 45° rotation in the xy-plane, resulting in equal $\langle \rho^*_{Bulk} \rangle$ and $\langle U^*/N \rangle$. The last decoration, zigzag, share alike $\langle \rho^*_{Bulk} \rangle$, but with $\langle U^*/N \rangle$ values hovering slightly more negative values.

2. Wall's presence play a fundamental role for small pore separation systems, which is perceptible in the peaks' size over the distribution profiles $g(z^*)$. This is slowly overlooked as the slit-like wall separation increases and the flattening of the distribution profiles around the normalization value, indicating a bulk-like behavior of the confined fluid around the center of the pore. This appearance is dependent of the temperature and bulk fluid, as well as the wall's constitution with the neutral one requiring less distance from the walls.

3. Although almost all the simulated systems (besides the one with a completely neutral wall) have fluid molecules with higher relative energy per molecule (as normalized with the bulk), the same doesn't happen for the adsorption as only a few confined systems have a higher adsorption density than it's bulk homonymous. This is true only for the attractive, squared and two-stripped decorated walls for the low-temperature and low-bulk-density system and only for the wholly attractive wall in the low-temperature and medium-bulk-density system; with only four out of fourty-two, no other system has a higher adsorption than its analogue in bulk phase.

4. Temperature's increment introduce a loose negligibility for the wall's decorations. For low-temperature systems preferential adsorption spots may be identified near the fixed positions of attractive molecules, something no longer true for the high-temperature system which homogeneously adsorbs fluid molecules regardless of the attractive/neutral designed pattern in the wall.

Appendix A

Random Numbers

Monte Carlo methods are heavily dependent on the fast, efficient and reliable production of streams of random numbers. Actual random physical processes, such as white noise generation from electrical circuits, generally, produce new numbers way too slowly to be effective with today's digital computers. Therefore, appealing for computer-implemented software is required to keep up with the demand, even though, it's a conceptual impossibility to use a precise and deterministic machine conceived by the human mind to produce "random" numbers.

After all, any program produces an entirely predictable output, hence not truly random. Knuth [45] discusses this dilemma and comments that the sequences aren't random, but they appear to be. Sequences generated in a deterministic way are often called pseudorandom or quasirandom and have worked quite well in nearly every application, provided that a suitable method has been carefully selected.

A consequence of randomness in the context of computer-generated sequences is that the deterministic program that produces a random sequence should be different and statistically uncorrelated with the computer program that uses its output.

Explosive growth in the use of Monte Carlo simulations has prompted an extensive investigation of new methods and the reliability of both old and new techniques. In a 1968 paper by Marsaglia [46], a discussion regarding the employment of poor quality random number generators (**RNGs**) lead to systematic errors; being more disturbing the possibility that for 20 years before the study's publication, bad but unrecognized results in Monte Carlo simulation studies had been produced.

A sequence of *independent random numbers* with a specified *distribution* means loosely that each number is merely obtained by chance, having nothing to do with other previous or upcoming numbers, and that each one has a specified probability of falling in any given range of values. A *uniform* distribution on a finite set of numbers is one in which each possible value is equally probable.

In general for a Monte Carlo simulation, the random number sequences required must be uniform, uncorrelated, and of extremely long period (meaning they do not repeat over a certain interval).

A.1 Tests For Quality

Marsaglia carefully examined in a later paper [47] the properties of random number generators using a battery of mathematical tests:

- **Uniformity test**: Break up the interval between zero and one into a large number of small bins and after generating a large number of random numbers check for uniformity in the number of entries in each bin.
- **Overlapping M-tuple test**: Check the statistical properties of the number of times M-tuples of digits appear in the sequence of random numbers.
- **Parking lot test**: Plot points in an m-dimensional space where the m-coordinates of each point are determined by m-successive calls to the random number generator. Then look for regular structures.

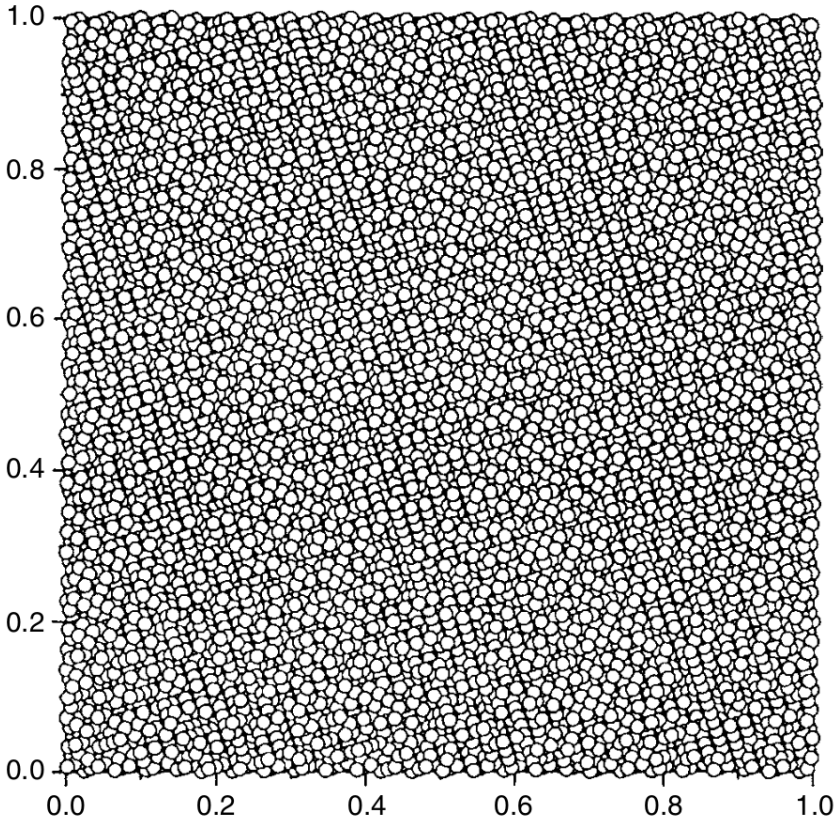

Figure A.1: 10,000 points plotted in a 2-dimensional space using consecutive pairs of random numbers as x- and y- coordinates. A display of a "bad" generator can be recognized by the exhibition of stripped patterns. Image taken from *A guide to Monte-Carlo Simulations in Statistical Physics* by David P. Landau and Kurt Binder [24].

A.2 Mersenne Twister: MT19937

All Monte Carlo simulations were carried out implementing the default RNG in the Julia language which uses the Mersenne Twister algorithm [48] which is a fast and high quality uniform double precision floating point pseudorandom number generator. The used version of Mersenne Twister is **MT19937**, which has a very long period of $2^{19937} - 1$ and passes several stringent statistical tests including Diehard (Battery of statistical tests for measuring the quality of RNG, developed by G. Marsaglia and first published in 1995 on a CD-ROM) [49].

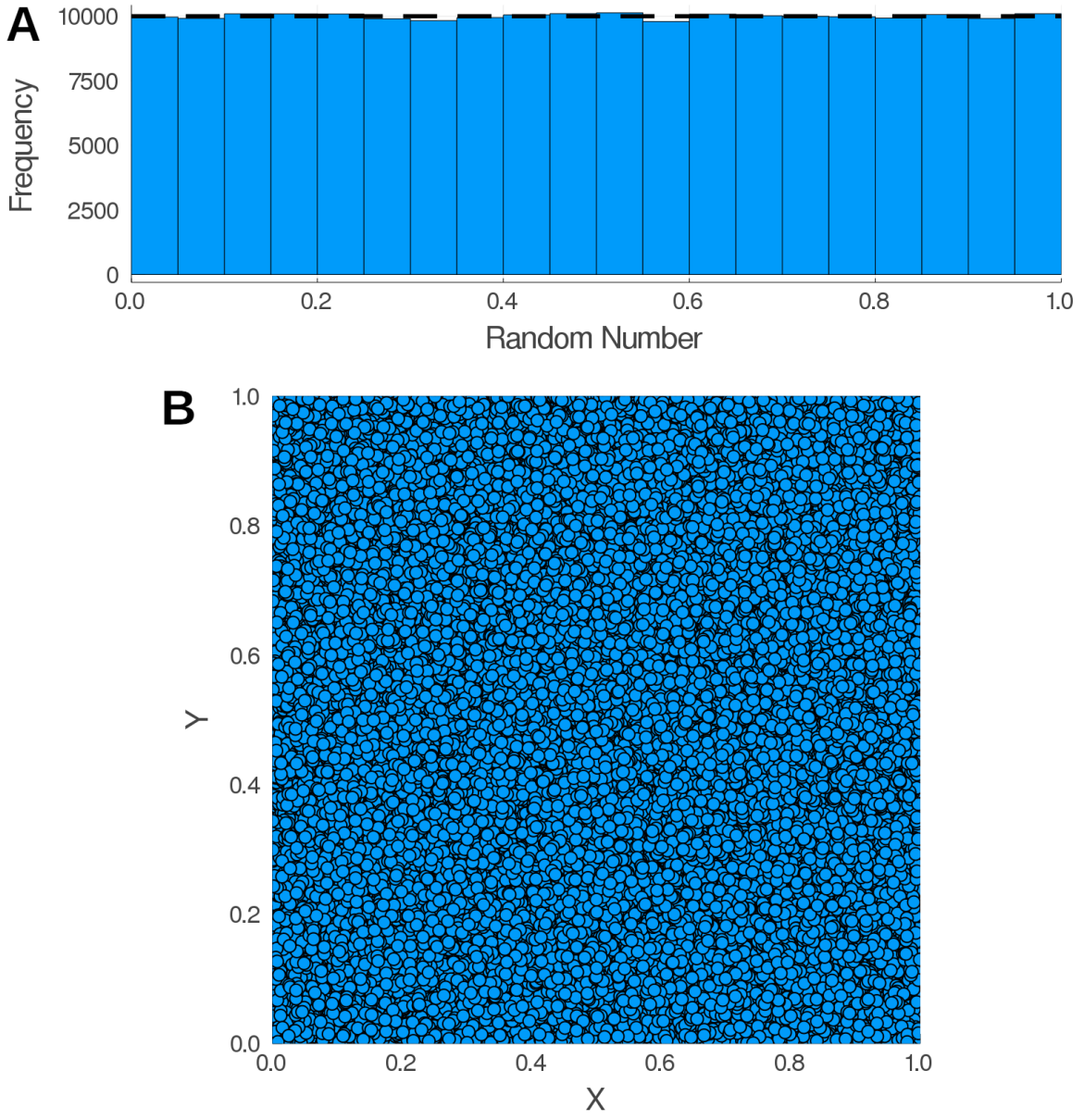

Figure A.2: Tests for the MT19937 method using 200,000 random numbers. **(A)** Uniformity test: Numbers look uniform, with each bin having approximately the same height (Total Random Numbers / Bins = 200,000 / 20 = 10,000). **(B)** Parking lot test: No visible pattern can be recognized.

Appendix B

Reduced Units

For a computational simulation, there are several reasons to use reduced units instead of regular *SI* units with the most prominent one, being the enabling of the principle of corresponding states. According to van der Waals, the theorem indicates that all fluids, when compared at the same reduced temperature and reduced pressure, have approximately the same compressibility factor and all deviate from ideal gas behavior to about the same degree. For instance, the same set of reduced units in a simulation can be used to describe the behavior of argon at a temperature of 60 K and a density of 840 kg/m^3, and, xenon at a temperature of 112 K and a density of 1617 kg/m^3. In reduced units, both simulations correspond to the state point $\rho^* = 0.5$ and $T^* = 0.5$. [43]

Usage of these units reduces all numeric values within the simulation to an order of magnitude of one, making it easier to spot errors in the simulation since extreme values are very unlikely to occur. Moreover, using numbers in this order of magnitude ensures that no floating-point errors occur due to the limited precision of the processor.

The system of reduced units consists of four fundamental parameters: reduced length σ^*, reduced mass m^*, reduced energy E^* and reduced charge q^*. From the previous parameters, compound units follow and are summarized in the following table.

Quantity	Symbol	Relation to *SI*
Length	r^*	r/σ
Mass	m^*	m/m_p
Time	t^*	$t/\sigma\sqrt{\epsilon/m_p}$
Temperature	T^*	$k_B T/\epsilon$
Energy	E^*	E/ϵ
Force	F^*	$F\sigma/\epsilon$
Pressure	P^*	$P\sigma^3/\epsilon$
Velocity	v^*	$v\sqrt{m_p/\epsilon}$
Density	ρ^*	$N\sigma^3/V$

Figure B.1: Reduced square-well units.

Appendix C

Codes

Codes referred throughout this work were developed in the Julia language [50], a flexible dynamic language, appropriate for highest numerical computing and scientific performance performance comparable to traditional statically-typed languages, achieved using type inference and just-in-time (JIT) compilation, implemented using LLVM.
With a semi-interactive design, codes were designed in such a way that no prior knowledge to julia is required to execute it. It's also a great opportunity for newcomers to the language as a pick up code. Outputs consist of two kinds:

- Multi-column out stream files with values in every simulation step and their corresponding average and standard deviation evolution. Also, a file summarizing the input and output of the run.
- Plots of the thermodynamical variables' evolution and histograms for a correspondence to the central limit theorem (theorem 2.2).

For first-timers, few additional packages are required from the builtin package manager Pkg, that may be run within julia REPL as follows:

```
] #Enters the Pkg REPL. Backspace or ^C to exit.
add Statistics, Plots, Test, LaTeXStrings, StatsPlots, Distributions,
 ArgParse
```

Code C.1: Package installation via Pkg.

C.1 Canonical Ensemble

Semi-interactive code for simulations in the NVT ensemble according to the Metropolis' acceptance/rejection criteria derived from the detailed balance condition of the ergodic markov chain proposed in chapter in 2.4. A sample of the code may be cloned from the GitHub repository from the following direction:

```
git clone https://github.com/omaraalvarez/Canonical.git
```

Code C.2: Cloning the canonical ensemble code.

Execution is straightforward by argument parsing:

```
julia Canonical.jl -h
usage: Canonical.jl [-h] ρ T

positional arguments:
  ρ      Density (type: Float64)
  T      Temperature (type: Float64)

optional arguments:
  -h, --help  show this help message and exit
```

Code C.3: Help message to execute the *Canonical.jl* code.

C.2 Grand Canonical

Semi-interactive code for fluid simulations in the μVT ensemble according to Mezei's Cavity-Biased algorithm from chapter 2.5.1, which improves insertions in high-density systems. A sample of the code may be cloned from the GitHub repository from the following direction:

```
git clone https://github.com/omaraalvarez/GrandCanonical.git
```

Code C.4: Cloning the grand canonical ensemble code.

Execution is straightforward by argument parsing:

```
julia GrandCanonical.jl -h
usage: GrandCanonical.jl [-h] μ T

positional arguments:
  μ            Chemical Potental (type: Float64)
  T            Temperature (type: Float64)

optional arguments:
  -h, --help  show this help message and exit
```

Code C.5: Help message to execute the *GrandCanonical.jl* code.

C.3 Confined - Grand Canonical

Semi-interactive code for the simulation of confined fluids, under hexagonally arranged slit-like walls, in the μVT ensemble according to Mezei's Cavity-Biased algorithm for the efficient insertion of high-density systems. A sample of the code may be cloned from the GitHub repository from the following direction:

```
git clone https://github.com/omaraalvarez/ConfinedGrandCanonical.git
```

Code C.6: Cloning the grand canonical ensemble code for confined systems.

Compared to its predecessor, execution of this code requires three parameters μ^*, T^* and L_z^*, accompanied by three optional parameters:

- $\boldsymbol{\rho^*_{Bulk}}$: Used for the normalization of the distribution profiles, in case a bulk simulation was previously carried out.
- **RayTracing**: Boolean "switch" for x- and z-axis image generation of the adsorption in the system via RayTracing techniques (PovRay must be installed, execution is automatic).
- **Configurations**: Boolean "switch" that saves the sampled configurations (default: 25,000) in *.xyz for a deeper analysis. BEWARE: High-density systems require large amounts of storage.

Execution is straightforward by parsing arguments:

```
julia Confined.jl -h
usage: Confined_GrandCanonical.jl [-D ρ_Bulk] [-C CONFIGURATIONS] [-P POVRAY]
  [-h] μ T h

positional arguments:
  μ                 Chemical Potental (type: Float64)
  T                     Temperature (type: Float64)
  h                     Slit's Separation (type: Float64)

optional arguments:
  -D, --ρ_Bulk      Bulk fluid's density (type: Float64, default: 1.0)
  -C, --Configurations  Enable/Disable Saving Configuraitons (type: Bool,
 default: false)
  -P, --PovRay          Enable/Disable PovRay Animations (type: Bool,
 default: false)
  -h, --help            show this help message and exit
```

Code C.7: Code execution for an arbitrary confiend system in the grand canonical ensemble.

References

[1] J. Israelachvili and D. Gourdon, "Putting liquids under molecular-scale confinement", Science **292**, 867–868 (2001).

[2] A. Wongkoblap, S. Junpirom, and D. Do, "Adsorption of lennard-jones fluids in carbon slit pores of a finite length. a computer simulation study", Adsorption Science and Technology **23**, 10.1260/0263617053737163 (2005).

[3] A. Jayaraman, C. K. Hall, and J. Genzer, "Designing pattern-recognition surfaces for selective adsorption of copolymer sequences using lattice monte carlo simulation", Physical review letters **94**, 078103 (2005).

[4] W. Song, J. Yao, J. Ma, A. Li, Y. Li, H. Sun, and L. Zhang, "Grand canonical monte carlo simulations of pore structure influence on methane adsorption in micro-porous carbons with applications to coal and shale systems", Fuel **215**, 196 –203 (2018).

[5] J. B. Curtis, "Fractured shale-gas systems", AAPG bulletin **86**, 1921–1938 (2002).

[6] J. Zhou, Z. Jin, and K. H. Luo, "Insights into recovery of multi-component shale gas by co2 injection: a molecular perspective", Fuel **267**, 117247 (2020).

[7] C. Bousige, C. M. Ghimbeu, C. Vix-Guterl, A. E. Pomerantz, A. Suleimenova, G. Vaughan, G. Garbarino, M. Feygenson, C. Wildgruber, F.-J. Ulm, et al., "Realistic molecular model of kerogen's nanostructure", Nature materials **15**, 576–582 (2016).

[8] R. J. Ambrose, R. C. Hartman, M. Diaz-Campos, I. Y. Akkutlu, C. H. Sondergeld, et al., "Shale gas-in-place calculations part i: new pore-scale considerations", Spe Journal **17**, 219–229 (2012).

[9] C. H. Sondergeld, M. E. Curtis, and C. S. Rai, "Application of fib/sem and argon ion milling to the study of foliated fine grained organic rich rocks", Microscopy and Microanalysis **18**, 622–623 (2012).

[10] R. F. Cracknell, P. Gordon, and K. E. Gubbins, "Influence of pore geometry on the design of microporous materials for methane storage", The Journal of Physical Chemistry **97**, 494–499 (1993).

[11] M. Beckner and A. Dailly, "Adsorbed methane storage for vehicular applications", Applied energy **149**, 69–74 (2015).

[12]T. A. University, "Making an alternate fuel usable in cars: researcher tackles natural gas storage", Phys Org (2013).

[13]R. I. Yousef, B. El-Eswed, and H Ala'a, "Adsorption characteristics of natural zeolites as solid adsorbents for phenol removal from aqueous solutions: kinetics, mechanism, and thermodynamics studies", Chemical engineering journal **171**, 1143–1149 (2011).

[14]T Motsi, N. Rowson, and M. Simmons, "Adsorption of heavy metals from acid mine drainage by natural zeolite", International Journal of Mineral Processing **92**, 42–48 (2009).

[15]C. M. S. Torres, *Alternative lithography* (Springer, 2003), pp. 1–14.

[16]S. M. Ulam and J. von Neumann, "Random ergodic theorems", Bull. Amer. Math Soc. **51** (1945).

[17]N. Metropolis, A. W. Rosenbluth, M. N. Rosenbluth, A. H. Teller, and E. Teller, "Equation of state calculations by fast computing machines", The journal of chemical physics **21**, 1087–1092 (1953).

[18]N. Metropolis, "The beginning of the monte carlo method", Los Alamos Science **15**, 125–30 (1987).

[19]A Herbert, "Metropolis, monte carlo, and the ma niac", Los Alamos Science, Fall (1986).

[20]A. Vesa, *Monte carlo methods*, 2nd Ed. (Johannes Kepler Universität, Linz, Austria, 2005).

[21]A. T. Bharucha-Reid, *Elements of the theory of markov processes and their applications* (McGraw-Hill Book Company, 1960).

[22]W. Feller, *An introduction to probability theory and its applications*, English, 2nd ed. (John Wiley, 1957).

[23]W. K. Hastings, "Monte carlo sampling methods using markov chains and their applications", (1970).

[24]D. P. Landau and K. Binder, *A guide to monte carlo simulations in statistical physics* (Cambridge university press, 2014).

[25]M. Newman and G. Barkema, *Monte carlo methods in statistical physics* (Oxford University Press: New York, USA, 1999).

[26]V. I. Manousiouthakis and M. W. Deem, "Strict detailed balance is unnecessary in monte carlo simulation", The Journal of chemical physics **110**, 2753–2756 (1999).

[27]W. Wood and F. Parker, "Monte carlo equation of state of molecules interacting with the lennard-jones potential. i. a supercritical isotherm at about twice the critical temperature", The Journal of Chemical Physics **27**, 720–733 (1957).

[28]B. Widom, "Some topics in the theory of fluids", The Journal of Chemical Physics **39**, 2808–2812 (1963).

[29]D. Adams, "Grand canonical ensemble monte carlo for a lennard-jones fluid", Molecular Physics **29**, 307–311 (1975).

[30]G. Norman and V. Filinov, "Investigations of phase transitions by a monte-carlo method", High Temperature **7**, 216 (1969).

[31]D. Adams, "Chemical potential of hard-sphere fluids by monte carlo methods", Molecular Physics **28**, 1241–1252 (1974).

[32]L. Rowley, D Nicholson, and N. Parsonage, "Monte carlo grand canonical ensemble calculation in a gas-liquid transition region for 12-6 argon", Journal of Computational Physics **17**, 401–414 (1975).

[33]G. L. Deitrick, L. E. Scriven, and H. T. Davis, "Efficient molecular simulation of chemical potentials", The Journal of Chemical Physics **90**, 2370–2385 (1989).

[34]M. Mezei, "A cavity-biased (T, V, μ) Monte Carlo method for the computer simulation of fluids", Molecular Physics **40**, 901–906 (1980).

[35]M. R. Stapleton and A. Z. Panagiotopoulos, "Application of excluded volume map sampling to phase equilibrium calculations in the gibbs ensemble", The Journal of Chemical Physics **92**, 1285–1293 (1990).

[36]D. A. McQuarrie, *Statistical mechanics*, First edition (Harbe and Row, 1976).

[37]A. P. Reinhold Haberlandt Dieter Michel and R. Stannarius, *Molecules in interaction with surfaces and interfaces*, 1st (Springer-Verlag Berlin Heidelberg, 2004).

[38]E. A. Ustinov and D. D. Do, "Simulation of gas adsorption on a surface and in slit pores with grand canonical and canonical kinetic monte carlo methods", Physical Chemistry Chemical Physics **14**, 11112–11118 (2012).

[39]S. B. Yuste and A. Santos, "A model for the structure of square-well fluids", Journal of Chemical Physics **101**, 2355–2364 (1994).

[40]L. Vega, E. de Miguel, L. F. Rull, G. Jackson, and I. A. McLure, "Phase equilibria and critical behavior of square-well fluids of variable width by gibbs ensemble monte carlo simulation", The Journal of Chemical Physics **96**, 2296–2305 (1992).

[41]J. P. R. B. Walton and N. Quirke, "Capillary condensation: a molecular simulation study", Molecular Simulation **2**, 361–391 (1989).

[42]W. R. Smith and H. L. Vörtler, "Monte carlo simulation of fluid phase equilibria in pore systems: square-well fluid distributed over a bulk and a slit-pore", Chemical Physics Letters **249**, 470 –475 (1996).

[43]D. Frenkel and B. Smit, *Understanding molecular simulation*, 2nd (Academic Press, Inc., Orlando, FL, USA, 2001).

[44]D. R. Bérard, P. Attard, and G. N. Patey, "Cavitation of a lennard-jones fluid between hard walls, and the possible relevance to the attraction measured between hydrophobic surfaces", The Journal of Chemical Physics **98**, 7236–7244 (1993).

[45]D. E. Knuth, *The art of computer programming, volume 2 (3rd ed.): seminumerical algorithms* (Addison-Wesley Longman Publishing Co., Inc., Boston, MA, USA, 1997).

[46]G. Marsaglia, "Random numbers fall mainly in the planes", Proceedings of the National Academy of Sciences **61**, 25–28 (1968).

[47]G. Marsaglia, "A current view of random numbers", in Computer science and statistics the interface (Elsevier Science Publishers BV, 1985), pp. 3–10.

[48]M. Matsumoto and T. Nishimura, "Mersenne twister: a 623-dimensionally equidistributed uniform pseudo-random number generator", ACM Trans. Model. Comput. Simul. **8**, 3–30 (1998).

[49]G. Marsaglia, *The marsaglia random number cdrom including the diehard battery of tests of randomness*, (1995) `https://web.archive.org/web/20160125103112/http://stat.fsu.edu/pub/diehard/`.

[50]J. Bezanson, A. Edelman, S. Karpinski, and V. B. Shah, "Julia: a fresh approach to numerical computing", SIAM review **59**, 65–98 (2017).